2019

COMPUTATIONAL AND EXPERIMENTAL INVESTIGATION ON THE WETTING BEHAVIOR OF DROPLET-FIBER SYSTEMS

Hossain Aziz
Virginia Commonwealth University

Computational and Experimental Investigation on the Wetting Behavior of Droplet-Fiber Systems

A dissertation submitted in partial fulfillment of the requirements for the degree of Doctor of Philosophy at Virginia Commonwealth University

by

Hossain Aziz

M.S. Applied Mechanics, Indian Institute of Technology Madras, Chennai, India

Director: Hooman V. Tafreshi

Professor, Department of Mechanical and Nuclear Engineering

Virginia Commonwealth University

Richmond, Virginia

May, 2019

Dedication

I would like to dedicate this work to my family, especially to my parents, my elder brother and my wife Nilufa. I could not have come this far without their unconditional support.

Acknowledgment

I wish to express my sincere thanks to Prof. Hooman V. Tafreshi, my advisor, for his continuous support, valuable guidance and encouragement throughout the course of my research. I would not have been able to finish this work without his support and unfailing faith in me.

I would like to extend my feeling of gratitude to the other members of my Ph.D. committee, Prof. P. Worth Longest, Prof. Daren Chen, Prof. Christina Tang, Prof. Ram B. Gupta and the late Prof. Alenka Luzar for their insightful questions, valuable suggestions and comments which have helped strengthen my work.

I am thankful to my friends (Adya, Sweta, Aneel) and my labmates (Ali, Ganesh, Mohammad, Sina, Mana, Noor, Ahmed hemeda, Ahmed Saleh) for making my life in VCU and Richmond memorable.

I would like to express my gratitude to my family for their endless support. I am thankful to my parents for always supporting me and encouraging me to follow my dreams. I am thankful to my wife Nilufa for being with me and being my support system. I am also thankful to my elder brother, my vabi, my niece Hiya, my mother-in-law and Sunny for always supporting me.

I would also like to express my appreciation to Virginia Commonwealth University and National Science Foundation for supporting my graduate education.

Table of Contents

List of Figures

	different segments of the FLISTA coating.
Fig. 6.4	(a) Tracking of WLI and LAI in a FLISTA coating made of parallel fibers in random arrangement at $P_h = 10,\ 100, 200, 350$ Pa. (b) Tracking of WLI and LAI in a FLISTA coating made of parallel fibers in ordered arrangement at $P_h = 10,\ 250, 500, 800, 1100$ Pa. Here, $d_f = 20$ μm, $\theta_W = \theta_L = 100^o$ and $\text{SVF} = 0.05$. For the FLISTA coating with ordered arrangement of fibers $s = 160$ μm.
Fig. 6.5	Schematic representation of the computational domain for Couette flow over FLISTA coating made of parallel fibers in ordered/staggered arrangement. (a) Computational domain including the LAI. (b) Computational domain with symmetry boundary condition approximated the LAI. Here, PBC denotes periodic boundary condition.
Fig. 6.6	(a) Contours of the x-velocity in the oil domain and in the water domain adjacent to the WLI at different pressures for FLISTA coating with random arrangement of fibers. Blue to red represents the x-velocity from -0.05 mm/s to 1 mm/s. (b) Effects of hydrostatic pressure on slip length for FLISTA coating with random fibers. Here, $U_p = 10$ mm/s, $\theta_W = \theta_L = 100^o$, $\text{SVF} = 0.05$, $N = 3$ and $d_f = 20$ μm.
Fig. 6.7	(a) Effect of hydrostatic pressure P_h on slip length for different values of d_f for FLISTA having ordered arrangement of fibers. (b) Contours of the x-velocity in the oil domain and in the water domain adjacent to the WLI. Blue to red represents the x-velocity from -0.03 mm/s to 0.75 mm/s. (c) Effect of P_h on normalized average slip velocity. (d) Effect of P_h on normalized average shear rate. Here, $U_p = 10$ mm/s, $H = 200$ μm, $\theta_W = \theta_L = 100^o$, $h = 80$ μm, $N = 3$ and $\text{SVF} = 0.05$.
Fig. 6.8	(a) Effect of s on slip length for FLISTA having ordered arrangement of fibers. (b) Contours of the x-velocity in the oil domain and in the water domain adjacent to the WLI. Blue to red represents the x-velocity from -0.06 mm/s to 1 mm/s. Here, $U_p = 10$ mm/s, $H = 200$ μm, $\theta_W = \theta_L = 100^o$, $h = 80$ μm, $d_f = 20$ μm and $N = 3$.
Fig. 6.9	Effect of lubricant layer thickness l on slip length for FLISTA having ordered arrangement of fibers. Here, $U_p = 10$ mm/s, $H = 200$ μm, $\theta_W = \theta_L = 100^o$, $h = 80$ μm, $s = 160$ μm, $N = 3$ and $d_f = 20$ μm.

Fig. 6.10	Effects of θ_W and θ_L on slip length for FLISTA having ordered arrangement of fibers. (b) Contours of the x-velocity in the oil domain and in the water domain adjacent to the WLI at $P_h = 10$ Pa. Blue to red represents the x-velocity from -0.03 mm/s to 0.75 mm/s. Here, $U_p = 10$ m/s, $H = 200$ μm, $h = 80$ μm, $s = 160$ μm, $N = 3$ and $d_f = 20$ μm.
Fig. 6.11	Effects of gap height H on slip length for FLISTA coating having staggered arrangement of fibers. Here, $U_p = 10$ m/s, $\theta_W = \theta_L = 100^o$, $h = 80$ μm, $s = 160$ μm, $N = 3$ and $d_f = 20$ μm.
Fig. 6.12	(a) Effects of lubricant viscosity μ_L on slip length for FLISTA having staggered arrangement of fibers. (b) Contours of the x-velocity in the oil domain and in the water domain adjacent to the WLI at $P_h = 10$ Pa. Blue to red represents the x-velocity from -0.025 mm/s to 0.8 m/s. Here, $U_p = 10$ mm/s, $\theta_W = \theta_L = 100^o$, $h = 80$ μm, $s = 160$ μm and $d_f = 20$ μm.

Abstract

COMPUTATIONAL AND EXPERIMENTAL INVESTIGATION ON THE WETTING BEHAVIOR OF DROPLET-FIBER SYSTEMS

By Hossain Aziz, M.S.

A dissertation submitted in partial fulfillment of the requirements for the degree of Doctor of Philosophy at Virginia Commonwealth University.

Virginia Commonwealth University, 2019

Director: Hooman V. Tafreshi
Professor, Department of Mechanical and Nuclear Engineering

Interaction of a liquid droplet and a fiber or layer of fibers is ubiquitous in nature and in a variety of industrial applications. It plays a crucial role in fog harvesting, coalescence filtration, membrane desalination, self-cleaning and fiber based microfluidics, among many others. This work presents a quantitative investigation on the interactions of a droplet with a fiber or layers of fibers. More precisely, the present work is focused on 1) predicting the effects of fiber's size and material on its ability to withhold a droplet against external forces and on the liquid residue left on the fiber after the droplet detachment, 2) predicting the outcome of two fibers competing to attract the same droplet, and 3) predicting the wetting stability of a droplet deposited on a layer of electrospun fibers. This work is comprised of series of computational and experimental studies for mutual validation and/or calibration. The simulations were conducted using the Surface Evolver code and the experiments were devised using a ferrofluid and a magnet.

We also investigated the drag reduction performance of fibrous coatings because of its close connection with droplet-fiber interaction. We started by studying the drag reduction performance

of a superhydrophobic granular coating because of its geometrical simplicity. We modeled the flow of water over the granular coating and studied the effects of hydrostatic pressure and microstructural properties on the drag reduction performance of the coating. We then examined the drag reduction performance of a lubricant infused surface with trapped air made of layers of parallel fibers (FLISTA). A mathematical model was developed to predict the shape of the water-lubricant interface and lubricant-air interface under a given hydrostatic pressure. This information was used to solve the flow field over the coating in a Couette configuration to find the effects of hydrostatic pressure and microstructural properties of the coating on its drag reduction performance.

Chapter 1. Introduction

1.1 Background Information

Interaction of liquid droplet with solid surfaces is of great importance in fog harvesting (1,2), droplet-gas filtration (3, 4), membrane desalination (5-7), textiles and apparel (8,9), droplet-fluid separation (10,11) and microfluidics (12,13) among many others. It is also frequently observed in nature. This work is focused on the interaction of a liquid droplet with a fiber and layers of fibers because of its ubiquitous presence in nature and engineering applications. From a microscopic point of view, the shape of a liquid droplet deposited on a solid surface depends on the molecular interactions between the molecules of the liquid and air at the liquid-air interface (LAI) and between the molecules of the liquid and solid at the solid-liquid interface (SLI). The liquid droplet takes the shape corresponding to the minimum of the total energy of the LAI and SLI.

The two most important macroscopic parameters that decide the shape of the liquid droplet deposited on a solid surface are surface tension of the LAI and the Young-Laplace (or intrinsic) contact angle. The shape of the liquid droplet deposited on a flat surface has been widely studied by researchers (14-17). The interaction of a liquid droplet with a fiber/fibrous coatings is different from that of a liquid droplet with flat surface because of the curvature of the surface of the fiber. However, a little attention has been paid on the interaction of the liquid droplet with a fiber and fibrous coatings. The background information about surface tension, Young-Laplace contact angle, capillary force, droplet interaction with a fiber/fibrous coatings and interaction of liquid with fibrous coatings are discussed in the flowing subsections.

1.1.1 Surface Tension, Contact Angle and Capillary Pressure

Surface tension of a fluid surface is one of the most important quantities in the theory of capillarity. In capillary theory, a fluid surface means the interface between the fluid and some other fluid or solid e.g. for a water droplet deposited on a flat surface, there are water-air interface and water-solid interface. Surface tension of a fluid-fluid interface is its tendency to shrink into a surface with minimum surface area. Surface tension has the dimensions of force per unit length or energy per unit area. When a liquid-gas interface meets a liquid-solid interface, a contact angle is formed. Contact angle is measured as the angle between the tangents to liquid-gas interface and liquid-solid interface at the liquid-solid-gas (three phase) contact line. It is a measure of the wettability of the solid surface with the liquid. It is also referred as intrinsic contact angle or Young-Laplace contact angle (YLCA). Contact angle and surface tension is related to each other through Young equation (18):

$$\sigma \cos\theta = \sigma_{SG} - \sigma_{SL} \tag{1.1}$$

Where, θ is the contact angle and σ, σ_{SG} and σ_{SL} denotes the surface tensions of the liquid-gas, solid-gas and solid-liquid interfaces respectively.

The shape of a static liquid-fluid interface depends on the Laplace or capillary pressure which is the pressure difference between the liquid and fluid across the interface. The relation between the Laplace pressure and shape of the liquid-fluid interface is represented by the Young-Laplace equation:

$$\Delta P_c = \sigma\left(\frac{1}{R_1} + \frac{1}{R_2}\right) \tag{1.2}$$

Where, R_1 and R_2 are the principal radii of the liquid-fluid interface. Note that, Laplace pressure is proportional to the surface tension σ of the liquid-fluid interface. Young-Laplace equation

with appropriate boundary conditions has been widely used by the researchers to predict the equilibrium shape of the liquid-gas interface (19 – 23).

1.1.2 Droplet Interactions with a fiber

Interaction of a droplet with a fiber received considerable attention from the scientists and engineers because it is frequently observed in nature and many industrial applications. Initial studies on droplet fiber interactions were mostly focused on droplet equilibrium shape on a horizontal fiber (24 – 29). Droplet deposited on a cylindrical fiber can have two different shapes depending on the fiber diameter, droplet volume, YLCA of the fiber and surface tension of the liquid. They are barrel shape (where the droplet completely engulfs the fiber) and clam-shell shape (where droplet partially wraps around the fiber). The barrel shaped droplet is observed for the large droplet volume or small contact angle. The clam-shell shaped droplet is observed for smaller droplet volume or bigger contact angle.

Later studies focused on the droplet motion along the axis of a fiber due to axial air jet blowing (30), temperature gradient along the fibre (31), vibration (32), gravity (33) and capillary forces (34). Force required moving a droplet along an oleophilic fiber was measured and a model was also proposed to predict the force (35). Droplet motion in a direction perpendicular to the fiber and relative to two intersecting fibers was also investigated (1, 30, 36 – 44). Most of these studies were focused on determining volume of the biggest droplet that a fiber (or two intersecting fibers) could hold (1), or the force required to initiate droplet detachment from the fiber (38). Despite its importance in many industrial applications surprisingly, less attention has been paid to the droplet residue left on a fiber after detachment (30). Droplet residue left on a

fiber (or on a surface) after detachment is for instance the reason for the undesired stains on a clean surface. The current study is devised to calculate the volume of the droplet residue left on the fiber after the detachment along with the detachment force.

1.1.3 Droplet Interactions with Rough Surfaces

There are two main stable wetting states for a droplet residing on a rough surface, the Wenzel state and the Cassie state (see e.g., 45 - 48). The Wenzel state corresponds to the state where the surface asperities are completely submerged in the droplet, whereas the Cassie state represents the condition where a layer of air is trapped underneath the droplet between the peaks of the surface protrusions (49–52). There are also some other wetting states in between or related to these two extreme states e.g., impregnated Cassie state or rose petal state (45). Cassie state is the main reason behind the water repellency of the superhydrophobic surfaces. In general, superhydrophobic (SHP) surfaces can provide droplet contact angles (CAs) in the neighborhood of 150 degrees and very low contact angle hysteresis (53 – 57). There are several examples of SHP surfaces observed in nature e.g. self-cleaning of lotus leaf (57). Making a SHP surface is one of the key issues in surface engineering. It has several industrial applications such as self-cleaning (53), drag reduction (55,56) and many others. Maximum contact angle observed on a flat surface is of the order of 120 degrees. The most effective way to produce a SHP surface is to impart roughness to a hydrophobic surface (53 – 57). One approach to impart roughness to a surface is micro-fabrication. While numerous studies have been focused on lowering the cost of micro-fabrication, manufacturing micro- or nano-roughness, this process has remained costly. Moreover, adding microfabricated roughness to a surface with arbitrary or random curvatures is still a challenge. An alternative approach (amongst many other methods) has therefore been to

impart comparable superhydrophobic behavior to a surface by coating the surface with fibers from a hydrophobic polymer (58 - 62).

Fibrous coatings usually consist of many layers of planar fibers deposited on top of one another in a random fashion. Coatings with random fiber orientations however, do not provide directionality to the mobility of a droplet over the surface. It is expected that controlling the orientation of the fibers in a coating can potentially provide some degrees of control over droplet mobility on a surface. In fact, it has been shown that a droplet can maintain different apparent CAs in different directions on a surface made of parallel grooves, for instance, indicating preferential droplet mobility along the grooves (63 – 72).

While producing a fibrous coating made of parallel fibers that can resemble a grooved surface is not a challenge, controlling the porosity and uniformity of such coatings is quite difficult because the fibers tend to pack relatively densely in a thin layer. A possible solution that helps with increasing the spacing between the fibers is to alternate the orientation of the fibers between the x- and y-directions during the spinning process. Coatings with orthogonally layered fibers tend to have a much higher porosity than their unidirectional counterparts and have been shown to exhibit unique properties for various applications (73–78). Unfortunately, coatings with orthogonal fibers may not necessarily perform like an anisotropic surface depending on the size and surface tension of the droplets, diameter and spacing of the fibers, and the Young–Laplace contact angle (YLCA) of the fiber polymer, as will be discussed later in this work.

1.1.4 Drag Reduction on SHP Surfaces

Superhydrophobic (SHP) coatings have been reported to reduce the friction drag between a body of water and a surface (56, 79-82). This effect is attributed to the ability of a rough hydrophobic surface to entrap air bubbles in its pores and thereby reduce the contact between the solid surface and the water (56, 79 – 82). SHP surfaces can potentially be applied to the hull of a boat or the inner walls of a pipe to reduce friction. Likewise, one can expect a superoleophobic (SOP) coating to potentially reduce the pressure needed to pump an oil-based product through a pipeline (83).

SHP surfaces are often produced by microfabricating small features on a smooth surface and then applying a hydrophobic chemistry to the roughened surface (56, 84). A more cost-effective alternative is to coat the smooth surface with a porous hydrophobic material, e.g., Polystyrene fibers or aerogel particles among many others (59, 85-89). Depending on coating geometry and flow parameters, the Wenzel state (fully-wetted), the Cassie state (fully-dry), or a series of transition states in between these two extreme states may prevail over a submerged SHP surface (45, 49-52). Unfortunately, even a slight departure from the Cassie state may result in a rapid increase in the surface wetted area (solid area in contact with water), and a consequential diminishment of the drag reduction effect.

Predicting the shape and position of the air–water interface over a SHP surface comprised of round objects (e.g., spherical or cylindrical objects) is not a trivial task. This is because the air–water interface does not become pinned to the round entrance of the pores, and so its shape and position can easily vary in response to variations of the instantaneous pressure over the surface.

This in turn makes the drag-reduction benefit of the surface highly pressure dependent. In a previous study, our group developed a modeling method to predict the shape and position of the air–water interface in order to use that information to obtain the wetted area of a granular SHP coating as a function of pressure (90, 91). While the drag force caused by a SHP surface is related to its wetted area, the nature of this relationship is not very clear. As shown by Steinberger et al. (92) and Karatay et al. (93) for instance, the air bubble entrapped in the pores of a SHP surface may protrude into the flow region (if the pressure outside the pores is less than that inside the pores) and increase the surface drag force. SHP surfaces fail to provide any drag reduction at excessive pressure because of failure of the AWI. In addition, the dissolution of the trapped air into the surrounding fluid may also lead to failure of the AWI (94 – 100). Alternate approach is to use LIS (101, 102) or LISTA (103). Wong et al. (101) and Solomon et al. (102) reported that SHP surfaces with a lubricating liquid trapped in its pores do not suffer from these limitations. These surfaces are called slippery liquid infused porous surfaces (SLIPS) or lubricant impregnated surfaces (LIS). Although, these surfaces repel various liquids (water, hydrocarbons, crude oil and blood), maintain low contact angle hysteresis $< 2.5^{o}$ and works at high pressure, they show measurable drag reduction (16-18 % maximum) only when $N \gg 1$ (102). Here, $N = \frac{\mu_w}{\mu_l}$. μ_w and μ_l are the dynamic viscosities of the working fluid (water in the present study) and the lubricant respectively. SLIPS or LIS do not show measurable drag reduction for low viscosity working fluids e.g. water. These surfaces also suffer from the problem of lubricant drainage due to shear or gravity (104 – 107). Hemeda & Tafreshi (103) reported that the drag reduction benefits of LIS can be significantly improved by placing a layer of air below the lubricant. This type of surface is referred to as a liquid infused surface with trapped air (LISTA). LISTA made up of parallel grooves and water as the working fluid can improve the drag

reduction performance significantly compared to its LIS counterpart depending on the flow direction relative to the grooves and drag reduction benefits can be obtained from LISTA even for $N < 1$ (103). The lubricant layer in LISTA reduces the rate of air dissolution into the working fluid (e.g. water) (103). Hemeda & Tafreshi (103) also conjectured that the entrapped air in the LISTA helped to stabilize the lubricant in the grooves.

Adding micro-fabricated roughness to a surface with arbitrary curvature is still costly as well as a challenging process. One alternative approach is to use a fibrous coating of hydrophobic polymers. The current study is devised to calculate the drag reduction advantage of granular and fibrous SHP coatings in terms of its microstructural properties.

1.2 Overall Objectives of This Thesis

Main objective of this dissertation is to investigate the wetting behavior of a liquid droplet with a fiber and fibrous coatings. Several experiments are performed and computational models are developed to predict the capillary force exerted by a droplet on a fiber, volume of the residue left on the fiber after detachment and the shape and stability of a droplet deposited on a single fiber or an array of fibers. Another objective is to investigate the drag reduction performance of fibrous LISTA coating.

First, the wetting behavior of a liquid droplet with a fiber is investigated. Most of the previous studies on droplet-fiber interaction were focused on predicting the shape of the droplet deposited on the fiber or the force required detaching the droplet from the fiber. Less attention was paid to the droplet residue left on the fiber after the detachment despite its importance in many industrial

applications. An experimental study is devised to better our understanding of the role of Young–Laplace contact angle (YLCA), fiber diameter, fluid viscosity, or droplet size on the volume of droplet residue left on a fiber after droplet detachment. This is made possible by using an aqueous ferrofluid droplet deposited on a horizontal filament in a controllable magnetic field. Droplet detachment process is imaged using a high-speed camera and the images are used to obtain residue volume and droplet detachment time. The detachment force is obtained using a sensitive scale. This work is presented in chapter 2.

Chapter 3 presents a detailed investigation on the shape of the liquid bridge and the mechanical forces acting on a liquid bridge between dissimilar fibers in parallel and orthogonal configurations. These shapes and forces are predicted computationally via numerical simulation and validated with experiments. Special attention is paid to the fiber-fiber spacing at which the liquid bridge detached from the fibers, and to how a transition from an equilibrium liquid bridge to a spontaneously (time-dependent) detaching bridge took place. This work also formulates the contribution of the geometrical and wetting properties of the fibers competing for the droplet that result from a liquid bridge detachment, and presents a mathematical expression to predict the fate of that droplet.

The wetting behavior of a droplet with fibrous coating comprised of layers of fibers is discussed in Chapter 4. Superhydrophobic coatings comprised of parallel and orthogonal layers of fibers are studied in terms of their ability to accommodate water droplets at the non-wetting Cassie state. The effects of microstructural properties of these coatings on droplet contact angles and Cassie state stability are investigated via numerical simulation. More specifically, mathematical

expressions are derived to predict whether or not such fibrous coatings can provide sufficient capillary forces for the droplet to remain in the Cassie state. Our numerical simulations conducted using the Surface Evolver finite element code indicated that apparent contact angle of a droplet can be different in longitudinal and transverse directions.

Regarding drag reduction on fibrous LISTA coating, we start with investigating the drag reduction performance of superhydrophobic granular coating because of their geometric simplicity and our previous knowledge about modeling granular superhydrophobic coating. Chapter 5 presents a computational study on the role of microstructural properties of a superhydrophobic granular coating on its drag reducing performance. More specifically, the effects of the Young–Laplace contact angle, particle diameter, and solid volume fraction on slip length are studied for submerged superhydrophobic granular coatings under negative (suction) and positive hydrostatic pressures. In addition, four different particle arrangements are considered to investigate the effects of particle spatial distribution on coatings' drag reduction performance. This was accomplished by accurately predicting the 3-D shape and surface area of a coating's wetted area fraction, and then by using this information to solve the flow field over the coating in a Couette configuration to obtain its drag reduction efficiency.

Chapter 6 presents a computational study on the drag reduction on fibrous liquid-infused surface with trapped air (FLISTA) comprised of fibers with heterogeneous wettability. The effects of different coating parameters and fluid properties on slip length for FLISTA coating are studied. For simplicity, the coating in the present work is made up of parallel fibers in a staggered or random arrangement. The water-lubricant interfaces as well as lubricant-air interfaces were

modelled as circular arcs and all the flow calculations were performed using ANSYS Fluent package. Finally, the overall conclusions of this thesis are presented in chapter 7.

Chapter 2. Effects of Fiber Wettability and Size on Droplet Detachment Residue

2.1 Introduction

Interactions between a droplet and a fiber or a fiber-like structure has received considerable attention from the engineering community for its importance in many new or existing industrial applications. Examples of such applications include, but are not limited to, fog harvesting (1,2), droplet filtration from gaseous streams, e.g., engine exhaust (3,4, 108,109) or droplet–fluid separation, e.g., water droplet removal from fuels (11, 110, 111), textiles and apparel (8,9), microfluidics (12,112), fuel cells (113,114) and many others.

Initial studies on droplet–fiber interactions were mostly focused on droplet equilibrium shape on a horizontal fiber (25 - 29). Later studies considered droplet motion along the axis of a fiber (30 - 35), in a direction perpendicular to a fiber (30, 36 - 39), or relative to two intersecting fibers (40 - 44). Most of the above studies were focused on determining volume of the biggest droplet that a fiber (or two intersecting fibers) could hold (1), or the force required to initiate droplet detachment from the fiber (38). Despite its importance in many industrial applications surprisingly, less attention has been paid to the droplet residue left on a fiber after detachment. To the knowledge of the authors, the work of Sahu et al. (30) is the only published study to report droplet residue on a filament after droplet detachment. Droplet residue left on a fiber (or on a surface) after detachment is for instance the reason for the accumulation of unwanted deposits on the surface of fibers in a liquid–liquid separation media or undesired stains on a clean surface. This study is therefore devised specifically to study droplet residue on a fiber after detachment. As will be seen later in this paper, the volume or shape of a droplet residue left on a

fiber after droplet detachment depends on many factors such as fiber diameter or Young–Laplace contact angle (YLCA).

The remainder of this chapter is structured as follows. Our experimental setup is presented in Section 2.2. Dynamics of droplet detachment from a fiber is qualitatively described in Section 2.3 using high-speed images recorded during detachment process. Section 2.3 also describes our image-based method developed to measure the volume of the droplet residue on the fiber. Effects of fiber diameter and YLCA on droplet detachment residue and detachment time are presented in Section 2.4. Conclusions drawn from the study are given in Section 2.5.

2.2 Experimental setup

Our experimental setup is shown in Figure 2.1. Flurocarbon smooth casting fishing line with radii of 191 μm and 264 μm, and bare copper wires with diameters of 162 μm and 259 μm were used in this study. The fiber was mounted on a 3-D printed holder placed on a Mettler Toledo AG104 balance with an accuracy of 0.1 mg. A New Era NE-300 syringe pump with an infusion rate ranging from 0.73 to 1200 μL/h was used to produce droplets with desired volumes. The liquid used in the experiments was water based ferrofluid (EMG508, Ferrotech, USA) with about 1% Fe_3O_4 nanoparticles (volumetric) and a density of $\rho = 1.05$ g/cm^3 at 25^o C. Glycerol with a viscosity of 1.412 Pa.s and surface tension of 0.066 N/m was mixed with the ferrofluid (having a viscosity of 1 mPa.s and a surface tension of 0.065 N/m) and used in some experiments to study the effects of dynamic viscosity on the droplet detachment process and residue volume. Both the ferrofluid and ferrofluid-glycerol mixtures behaved like a Newtonian fluid (see Appendix A for details about the viscosity measurements of these liquids). An axially magnetized cylindrical

permanent magnet with a diameter of 21.5 mm and a length of 22 mm was mounted on a Mitutoyo electronic height gauge and moved slowly towards the droplet to exert a vertical force on the droplets. Special attention was paid to ensure that the magnet perpendicular to the fiber and is centered with regard to the droplet.

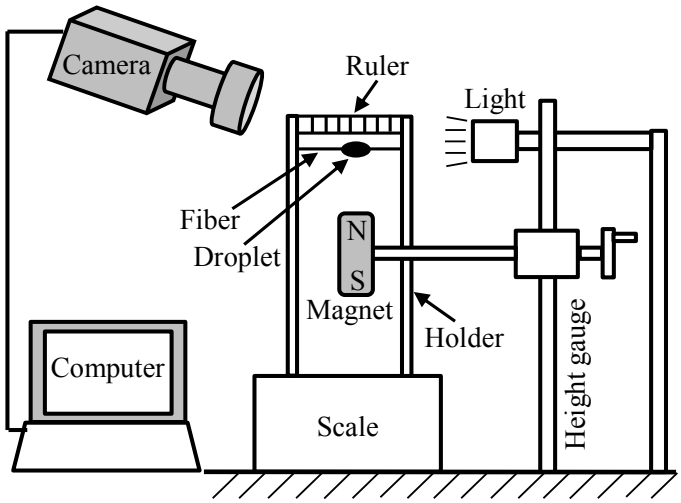

Fig. 2.1: Schematic representation of our experimental setup.

Experiment started by placing a droplet on the fiber and zeroing the scale. The magnet was then moved towards the droplet in small increments. Equilibrium shape of the droplet was imaged in each step of the experiment until a spontaneous detachment process (where no additional force was needed for droplet shape deformation) started (45). The droplet detachment process was recorded with a Phantom Miro LAB340 high-speed camera at 2400 frames per second. As the gravitational and magnetic forces where applied to the droplet in the same direction in our experiments, we zeroed the scale after placing the droplet so that the value read on the scale represent the magnetic force only. The total detachment force (reported in the figures) was obtained by adding the weight of the droplet to the magnetic force obtained from the scale.

We also performed experiments with fishing lines having different YLCAs but same radius. This was done by coating the original fishing line with Heptadecafluoro-1,1,2,2-Tetrahydrodecyl Trichlorosilane (FDTS) which is proven to be effective in increasing the YLCA of polymeric surfaces (111,116,117). To do so, the fiber was placed in a petri dish and a droplet of FDTS was placed far from the fishing line in the same petri dish. The lid was then closed to allow the FDTS to evaporate and deposit on the fiber in a sealed environment for a few hours. Different YLCAs were obtained by varying the fiber exposure time to FDTS. Fishing lines with YLCA values of about 75^o, 90^o and 110^o were obtained using FDTS coating for the present study. To estimate the YLCA of the coated fiber, a droplet with a known volume was placed on the fiber and imaged under the influence of gravity. The same droplet–fiber system was then simulated using Surface Evolver code (118) for fibers with different YLCAs. The distance between the apex of the droplet and the axis of the fiber as well as the profile of the droplet observed from the transverse direction were used to compare the shape of the droplet obtained from simulation to that imaged experimentally when estimating the YLCA of a fiber (see the Appendix A and also the paper by Amrei *et al.*, 38 for more details).

2.3 Droplet detachment dynamics

Consider a ferrofluid droplet deposited on a fiber. Bringing the magnet closer to the droplet, increases the force exerted on the droplet. The droplet goes through a series of shape deformations before it eventually detaches from the fiber (see Figure 2.2a). One can obtain a stable equilibrium shape for any force exerted on the droplet as long as the force is smaller than the detachment force (the minimum force needed to detach the droplet from the fiber).

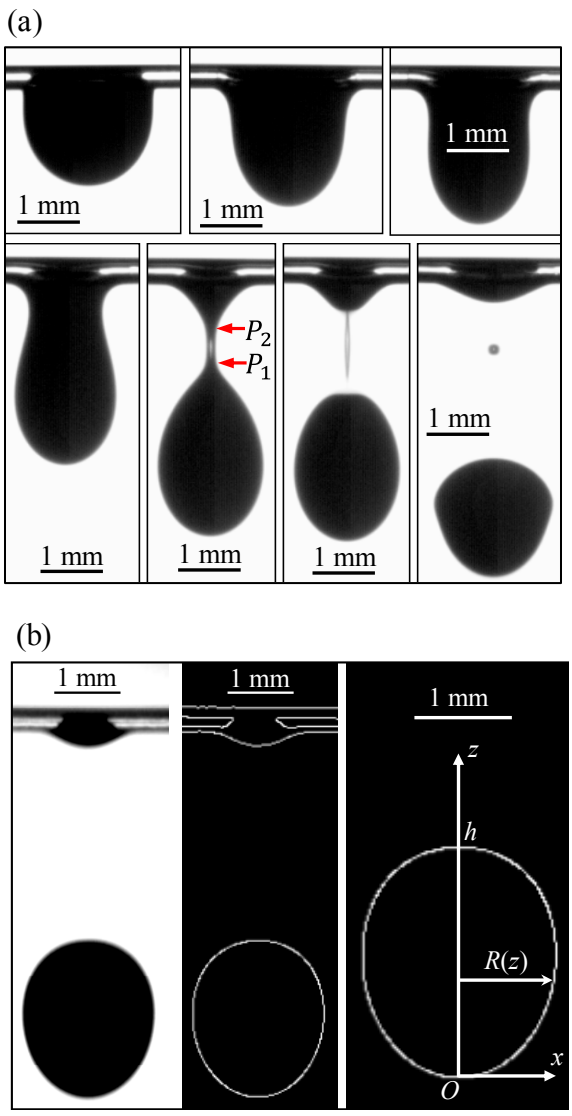

Fig. 2.2: Detachment process of a ferrofluid droplet with a volume of 3.5 µL from a fishing line with radius 191 µm and an YLCA 65° under the influence of an increasing magnetic force (a). Starting from a series of reversible quasi-static droplet deformations (first row of images) to an irreversible spontaneous detachment process (images in the second row). Our image-based residue volume calculation method is shown in (b) using a droplet with a volume of 5.5 µL detaching from the above fiber. The middle image in (b) is obtained by applying an edge-detection algorithm using Mathematica software and used for volume integration as shown in the last image in (b).

When the magnetic force approaches the detachment force, a spontaneous detachment process starts. In this process, a "neck" appears in the droplet profile, and it becomes thinner and longer with time (see Figure 2.2a). At some point, the neck detaches from the main droplet, and few milliseconds later, it detaches from the remainder of the droplet on the fiber (i.e., the residue) to

form a satellite droplet. The satellite most often follows the main droplet and coalesces with it, but it may also travel upward and coalesce with the residue. Volume of the detached droplet V_{dd} and the residue on the fiber V_r depend on the position of the first and second pinch-off points P_1 and P_2 on the neck as shown in Figure 2.2a. Regardless, the satellite volume is too small to make any difference in our calculation of residue volume, and so the satellite and its fate are completely ignored in the current study.

We calculate the residue volume on the fibers via image processing. Direct measurement of residue volume accurately is a challenge because of its minute size and irregular shape. However, the shape of the detached droplet was axisymmetric (see Fig. A4 in the Appendix A). Therefore, we calculate the volume of the detached droplet and subtract it from the volume of the original droplet to obtain the residue volume. We use *Mathematica to* extract the coordinates of the droplet profile after detachment and revolve it about the z-axis to compute the droplet volume (see Figure 2.2b), i.e.,

$$V_{dd} = \pi \int_0^h R(\mathrm{z})^2 \, dz \tag{2.1}$$

In Equation 2.1, h and $R(\mathrm{z})$ are the height and the local radius of the detached droplet, respectively.

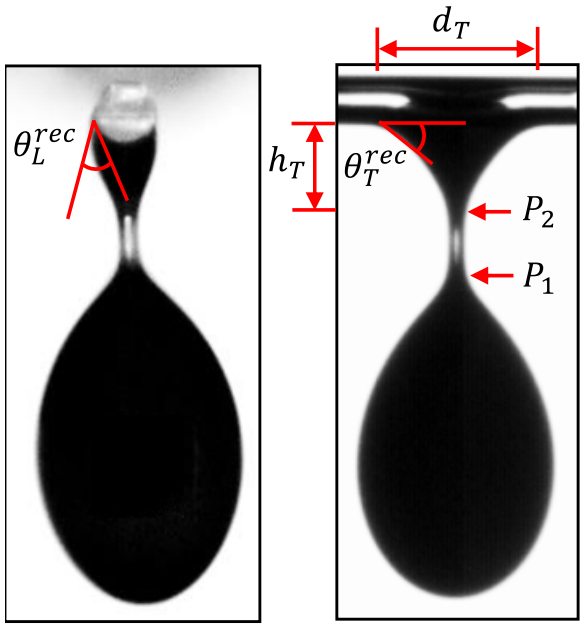

Fig. 2.3: Longitudinal (left image) and transverse (right image) profiles of a droplet with a dimensionless volume of $V / r_f^3 = 506$ detaching from a fiber with $r_f = 191$ µm and $\theta_{YL} = 65^o$ are shown. P_1 and P_2 are the first and second detachment (pinch-off) points, respectively.

To better quantify and analyze the shape of the residue on a fiber, a new terminology is defined and used throughout this paper. Length of the residue on the fiber right before the detachment moment is referred to as transverse contact length (see Figure 2.3) and is denoted with d_T. Distance between the second detachment (pinch-off) point and the lower surface of the fiber is shown with h_T. Receding contact angles in the transverse and longitudinal directions are denoted with θ_T^{rec} and θ_L^{rec}, respectively (see Figure 2.3). Since two high-speed cameras were needed (but one was available) to simultaneously image the droplets from two different angles over time, we chose to only record θ_T^{rec} as it was easier to image, and as it seemed to better illustrate the shape of the droplet during detachment. Nevertheless, our preliminary observations suggest that θ_L^{rec} is generally larger than θ_T^{rec} (but smaller than YLCA of the fiber). Note also that the primary objective of the work presented in this paper was to estimate the volume of residue on the fiber,

and our residue calculation method does not require θ_L^{rec} information. Therefore, in the remainder of the paper we only report d_T, h_T, and θ_T^{rec}.

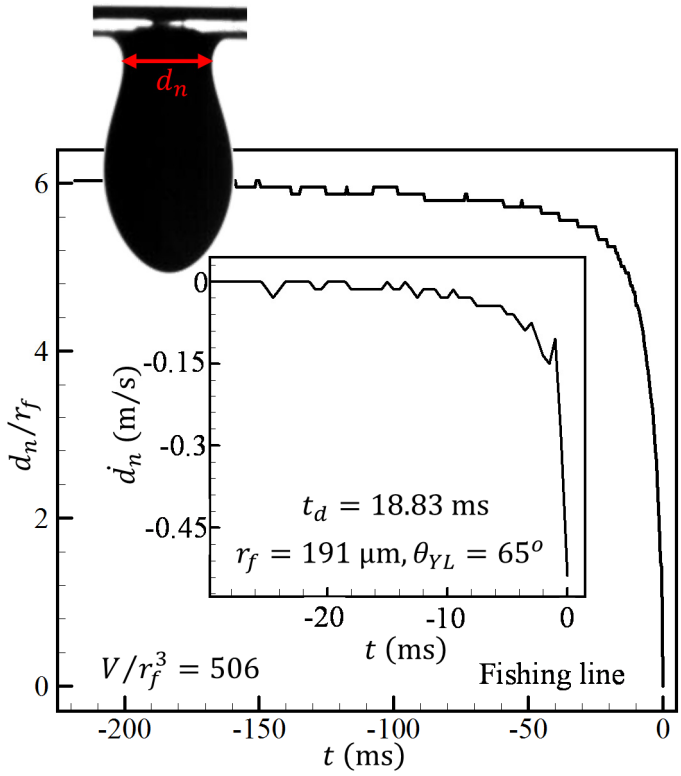

Fig. 2.4: Dimensionless neck diameter vs. time is shown for a droplet with a dimensionless volume of $V / r_f^3 = 506$ detaching from a fiber with a radius of 191 μm and an YLCA of 65°. The rate of change of neck diameter with time $\dot{d}_n$ near the detachment point is shown in the inset.

To better understand the dynamics of droplet detachment, we measured droplet detachment time by monitoring droplet neck diameter d_n over time until it went to zero at the detachment moment. More specifically, we define detachment time as the time period starting when $\dot{d}_n = \left|\frac{\partial d_n}{\partial t}\right| \neq 0$ and ending when $d_n = 0$. Figure 2.4 shows an example of such calculations, where d_n (non-dimensionalized using fiber diameter) is plotted versus time for a droplet with a volume of 3.5 μL on a fiber with a radius of 191 μm and a YLCA of 65° (the inset figure shows $\dot{d}_n$

versus time). A detachment time of 18.83 ms was obtained for this example. Further discussion on the effects of fiber diameter and YLCA on droplet detachment time and residue volume are given in the next section.

2.4 Results and discussion

2.4.1 Effects of YLCA on residue volume and detachment time

In this section, we experiment with fibers having a radius of $r_f = 191\ \mu m$ but different YLCAs. Example images showing droplet detachment from fibers with YLCAs of 65, 90, and 110 degrees are shown in Figure 2.5a. It can obviously be seen that droplet residue is smaller on fibers with a larger YLCA. It is worth mentioning that for the experiments reported in this paper droplets were large enough to exhibit a clamshell profile under gravity $\left(V / r_f^3 \geq 217\right)$.

Figure 2.5b shows droplet detachment time t_d versus droplet volume (non-dimensionalized using fiber radius cube), and it can be seen in this figure that detachment time increases almost linearly with increasing droplet size. Droplet detachment time also increases with decreasing YLCA of the fiber (i.e., it takes longer for a droplet to detach from a more hydrophilic fiber). The effects of YLCA on detachment time can be justified by monitoring how d_T / r_f, h_T / r_f, and θ_T^{rec} vary with YLCA in Figure 2.5c. It is interesting to note that d_T / r_f, h_T / r_f, and θ_T^{rec} are independent of the dimensionless droplet volume V / r_f^3, and θ_T^{rec} values are about one-half of their corresponding θ_{YL} values for most of the cases considered (except for $\theta_{YL} = 110^o$). It is also noticeable that d_T / r_f and h_T / r_f both decrease with increasing YLCA. This means that the second detachment point moves towards the fiber when YLCA is larger, as can be seen in Figure

2.5a (volume of the satellite droplet becomes smaller when YLCA is higher).

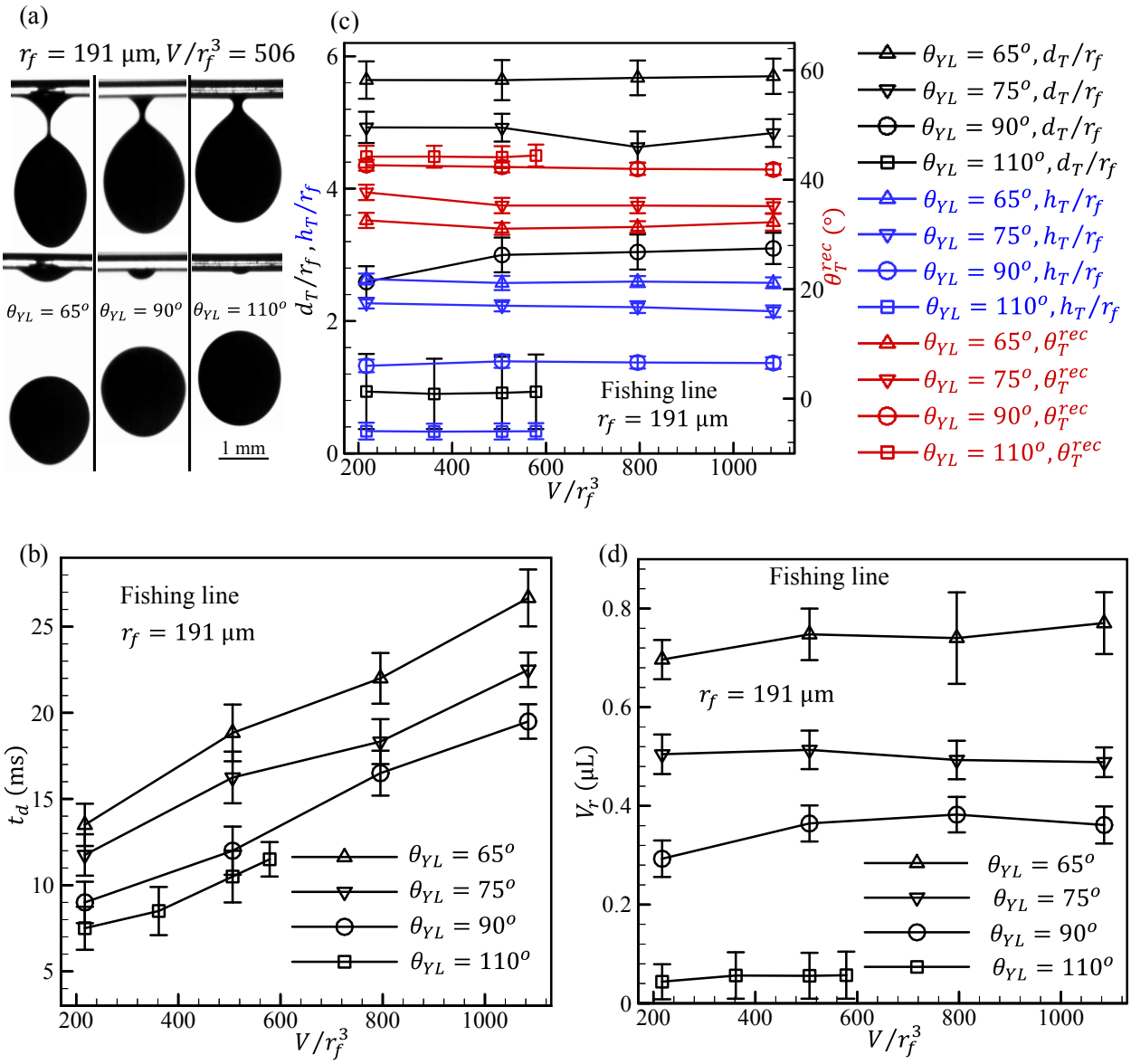

Fig. 2.5: Example images of a droplet with $V/r_f^3 = 506$ detaching from a fiber with a radius of 191 µm but with different YLCAs are given in (a). Droplet detachment time from fibers with a radius $r_f = 191$ µm but different YLCAs is reported in (b) for droplets with different volumes. Effects of YLCA on d_T/r_f, h_T/r_f and θ_T^{rec} are given in (c) for the same droplets and fibers. Droplet residue volume left on the fibers are given in (d).

The results given in Figure 2.5c indicate that volume of the triangle-shaped fluid attached to the fiber (the fluid that eventually becomes the residue on the fiber) decreases with the increase of

YLCA (see Figure 2.5d). In addition, the results presented in Figure 2.5d indicate that residue volume does not depend strongly on the volume of the droplet, which is in agreement with the observations made by Yildirim *et al.* (119) for droplet detachment from a capillary nozzle. The droplet detachment force obtained from these experiments are given in the supplementary materials for interested readers (see Fig. A5 in Appendix A).

2.4.2 Effect of fiber radius on residue volume and detachment time

Droplet detachment experiments were performed with fishing lines of two different radii of 191 μm and 264 μm but a common YLCA of about 65 degrees to study the effects of fiber diameter on droplet detachment time and residue volume. Figure 2.6a shows droplet detachment time from the above fibers. It can be seen that detachment time increases with increasing fiber diameter (the inset figures in Fig. 2.6a show the shape of the droplet at the detachment moment). With regards to droplet shape at the detachment moment, it was observed that d_T/r_f remains same but h_T/r_f decreases slightly with fiber radius (see Figure 2.6b). Note that d_T and h_T increase with increasing fiber radius r_f. This indicates that the second detachment point moves away from the fiber when the fiber diameter is thicker leading to an increase in the residue volume. It was also observed that the first detachment point moves closer to the fiber and the length of the neck becomes shorter when the fiber is thinner. Receding angles θ_T^{rec} are also reported in Figure 2.6b, and for the range of fiber radii considered in our study, no strong dependence on fiber radius was observed. These results indicate that residue volume should increase with the increase of fiber radius which seems to be the case as can be seen in Figure 2.6c. It should be noted that, both the residue volume and the detached volume increase with

increasing fiber diameter when $\frac{V}{r_f^3}$ is kept constant for a droplet–fiber combination. However, if droplet volume V is kept constant (instead of droplet dimensionless volume $\frac{V}{r_f^3}$), then the detached volume decreases with increasing fiber radius. The droplet detachment forces for fibers with different radii are given in Appendix A (see Fig. A5) for interested readers.

Similar experiments were also conducted using copper wires with an YLCA of 50 degrees but two different radii of 162 μm and 259 μm. The conclusions drawn from the copper wire experiments were almost identical to those obtained with fishing lines and so they are only reported in Appendix A (see Fig. A6).

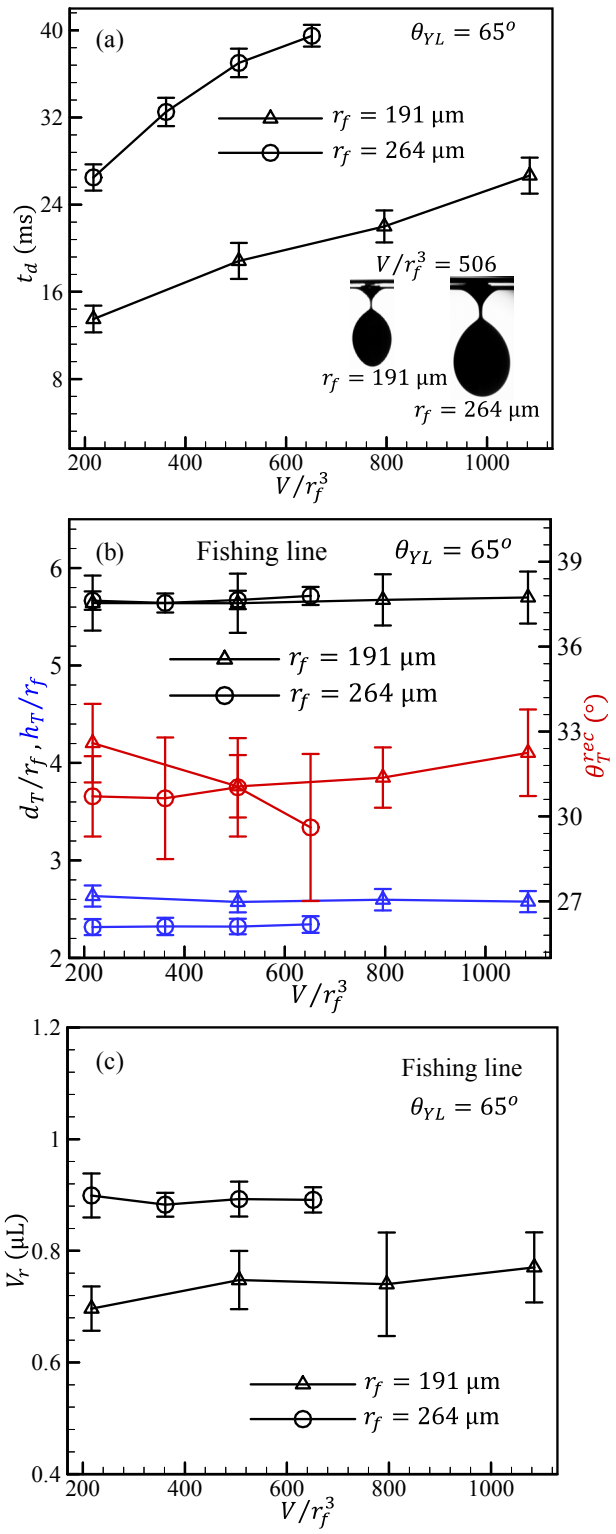

Fig. 2.6: Effects of fiber radius on detachment time for droplets with different dimensionless volumes is given in (a). The inset figure shows example images taken from droplets with a fixed dimensionless volume of $V/r_f^3 = 506$ at the moment of detachment from fibers of different radii. Effects of fiber radius on d_T/r_f, h_T/r_f and θ_T^{rec} are given in (b). Effects of fiber radius on residue volume is given in (c).

2.4.3 Effect of liquid viscosity on residue volume and detachment time

To study effects of fluid's viscosity on detachment time and residue volume, detachment experiments were conducted using ferrofluid–glycerol mixtures with different glycerol concentrations varying from 0 to 45% (resulting in a mixture viscosity ranging from 1 to 5.5 mPa.s measured using an Discovery HR – 3 hybrid rheometer). Note that addition of glycerol did not significantly change the surface tension of the ferrofluid or its contact angle with the fibers. Examples of droplet detachment profiles are given in Figure 2.7a for different glycerol percentages (the images are not taken at the exact detachment moment). As shown in Figure 2.7a, droplet detachment time t_d does not vary significantly with varying fluid viscosity for the range of viscosities considered here (in qualitative agreement with the effects of viscosity in the experiment reported by Dressaire *et al.* (120) and Comtet *et al.* (121)). Interestingly however, residue volume seems to decrease with increasing droplet viscosity as shown in Figure 2.7b, which is consistent with the trend of variations of d_T/r_f, h_T/r_f, and θ_T^{rec} with viscosity shown in Figure 2.7c. In these experiments, we also investigated the effects of viscosity on detachment force as can be seen in Figure 2.7d. It can be seen that for the range of viscosity variation considered, droplet detachment force seems to be unaffected by droplet viscosity. Effects of droplet viscosity is expected to become more prominent when effects of inertia is increased (faster detachment process), or when the droplet viscosity is much higher (119, 122).

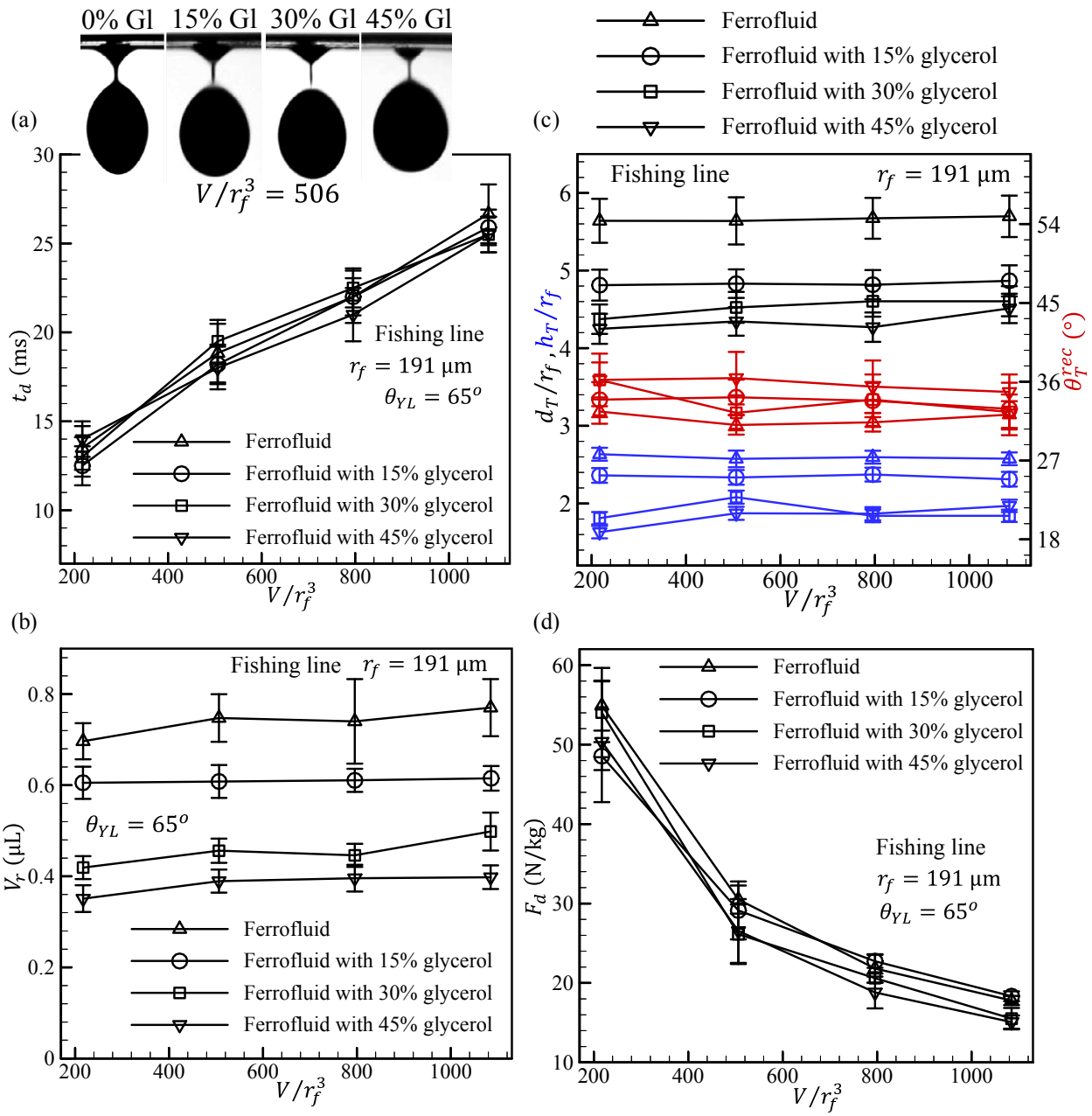

Fig. 2.7: Droplet detachment time from a fiber with a radius r_f =191 µm and an YLCA of 65 deg. is reported in (a) for droplets with different viscosities ranging from about 1 mPa.s (ferrofluid) to about 5.5 mPa.s (ferrofluid with 45% glycerol). Effect of droplet viscosity is reported in (b) for residue volume, in (c) for d_T/r_f, h_T/r_f, θ_T^{rec}, and in (d) for detachment force.

2.5 Conclusions

Droplet detachment from a fiber goes through a series of quasi-static equilibrium states in which droplet shape changes reversibly in response to the force applied to the droplet, and a final spontaneous (irreversible) process where it actually detaches from the fiber over a short period of time referred to here as droplet detachment time. The work presented here was focused primarily on droplet detachment time and droplet residue volume left on the fiber after detachment. Our results indicate that residue volume decreases with increasing fiber YLCA or droplet viscosity (in a viscosity range of 1 to 5.5 mPa.s). Moreover, residue volume was found to increase with increasing fiber diameter (for a given YLCA) but remains almost independent of droplet volume. Droplet detachment time was found to increase with droplet volume or fiber diameter but remained unaffected by increasing droplet viscosity in 1 to 5.5 mPa.s range. Detachment time was also found to decrease with increasing YLCA of the fiber.

Chapter 3. Competing Forces on a Liquid Bridge between Parallel and Orthogonal Dissimilar Fibers

3.1 Introduction

Liquid bridge between two solid surfaces has been the focus of many previous studies for its ubiquitous presence in a variety of applications. The capillary force generated by a capillary bridge contributes to the adhesion force that frogs, insects, or geckoes create to climb a vertical surface (123–125). For instance, a particular type of beetle can generate an adhesion force of more than 60 times its body weight thanks to an array of liquid bridges that forms between its feet and the surface it walks on (126). In industry, liquid bridge plays a crucial role in underground oil recovery (127,128) and granular systems (129-134), wetting and liquid transport in coalescence filters and textiles (3,11,20,135-140), design of magnetic hard-disks (141,142), papermaking (143), fiber-based microfluidics (112,144,145) and fuel cells (113,114) among many others.

Scientific research on liquid bridge started in 1805 by Young who investigated a liquid bridge formed between two flat plates to study the liquid surface tension (146). Later, Gauss derived the Young-Laplace equation which predicts the equilibrium shape of an interface separating two immiscible fluids (147). Since then, many others studied liquid bridge between smooth flat plates for its industrial relevance, and also for the simplicity of its axisymmetric profile. These include many pioneering investigations where the effects of surface roughness or contact angle hysteresis on the shape and stability of capillary bridge were studied (148-153). Significant attention has also been paid to the fluid mechanics of a liquid bridge between two spherical objects, or between a sphere and

a flat plate. The main objective of these studies was to measure the forces between the involved surfaces in terms of the distance between them or as a function of their surface properties in the absence (142,154-158) or presence of gravity (159,160).

Given the decades of research on liquid bridges of different properties, very little attention has been paid to the case of a liquid bridge between two fibers. In contrast to most previous studies, a liquid bridge between two fibers does not have an axisymmetric profile. This makes it harder to develop a mathematical description for the 3-D shape of the bridge. The shape of a liquid bridge between two parallel cylinders with a small spacing and in the absence of gravity was first studied by Princen (161). Later, Protiere et al. (162) modified Princen's equations to study how a liquid body transitions from a droplet shape to a long liquid bridge between two parallel fibers when varying the fiber–fiber spacing, fiber diameter, fiber's Young–Laplace contact angle (YLCA), or the liquid volume. Princen's equation was also used by Schellbach et al. (163) to propose a method to measure the contact angle of natural fibers. Virozub et al., (164) Wu et al., (165) and Bedarkar et al. (166) simulated the 3-D shape of a liquid bridge between two fibers and reported the capillary forces acting on the fibers as a function of fiber–fiber spacing or the relative angle between the fibers (164). Durpat and Protiere (167), Durpat et al. (168), and Soleimani et al. (169) also studied the problem of a capillary bridge between two fibers but with the main focus on fiber deformation in response to capillary forces.

The study presented in this chapter contributes to the above body of literature by presenting a one-on-one experiment–simulation comparison for a capillary bridge formed

between two fibers in parallel and orthogonal configurations in the presence of gravity. Our work compares measured and simulated capillary forces exerted on the fibers by the liquid bridge throughout the stretching process and especially at the moment of bridge detachment from one of the fibers. The detachment force, in particular, is compared to the force required to detach a pendent droplet (with the same volume as the liquid bridge) from the fibers. This work also presents, for the first time, the effects of fiber radius or fiber YLCA dissimilarities on the liquid bridge shape and the capillary forces exerted on the fibers at the moment of liquid–fiber detachment. Special attention is paid to discuss how the two fibers compete for the droplet during bridge detachment, and how their radius or YLCA dissimilarity plays a role in determining the fate of the resulting droplet.

The remainder of this chapter is structured as follows. The experimental setup and the computational technique used in the present study are described in Section 3.2. The general physics of the liquid bridge between two fibers is qualitatively discussed in Section 3.3. Our results are discussed in Section 3.4. This section includes the effect of fiber spacing on the capillary forces, detachment force, and the corresponding shape of the liquid bridge for two fibers (similar and different) in parallel and orthogonal configurations and the transfer of the liquid between the two fibers after detachment. The conclusions from the study are discussed in section 3.5.

3.2 Methods of Investigation

3.2.1 Experimental Setup

Our experimental set-up is shown in Fig. 3.1. Flurocarbon smooth casting fishing line with radii of 105.5 μm and 190.5 μm were used in our study. The YLCA for the fishing lines were obtained using an image-based method reported in our previous work (38,170-172). The experiment was conducted with the two fibers positioned horizontally above one another. The lower fiber was mounted on a 3-D printed holder placed on a Mettler Toledo AG104 balance having an accuracy of 0.1 mg.

The upper fiber was attached to another holder mounted on a Mitutoyo electronic height gauge. A New Era NE-300 syringe pump with an infusion rate ranging from 0.73 to 1200 μL/h was used to produce droplets with desired volumes. The liquid used for the experiment was a water-glycerol mixture (15% by weight) having a surface tension of 0.071 N/m (measured via the pendent droplet method using a DSA25E drop shape analyser), viscosity 1.53 mPa.s (measured using a Discovery HR—three hybrid rheometer), and a density of 1039 kg/m3 at 20^{o} C.

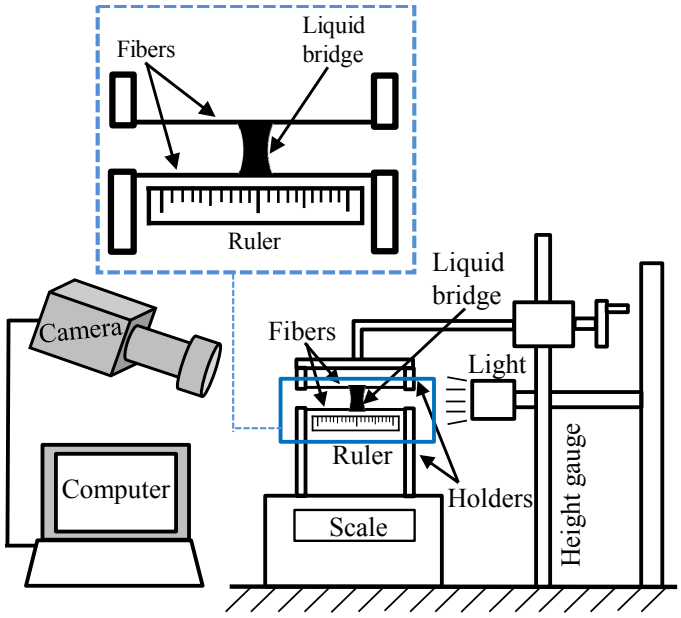

Fig. 3.1: The experimental setup designed for study.

The scale was zeroed at the start of the experiment. A droplet was placed on the upper fiber and a stable liquid bridge was formed by lowering the upper fiber until the droplet touched the lower fiber. The upper fiber was then moved upward slowly to stretch the liquid bridge until a spontaneous detachment process (where no additional stretching was needed to deform the liquid bridge) started. The force applied by the liquid bridge to the lower fiber was read on the scale and the force applied to the upper fiber was obtained by adding the weight of the liquid to that. The force applied to the upper fiber at the onset of spontaneous detachment is referred to here as the detachment force F_d. The liquid bridge stretching process was recorded by a Phantom Miro LAB340 high-speed camera at 100 frames per second.

To ensure that inertial and viscous effects were negligible during the experiments, we calculated the Weber and Capillary numbers, defined respectively, as $We = \rho U^2 d_l \sigma^{-1}$ and

$Ca = \mu U \sigma^{-1}$ (ρ, σ, U, and μ are density, surface tension, upper fiber velocity, and viscosity, respectively and $d_l = \sqrt[3]{6V_l/\pi}$ is the volume-equivalent diameter of the liquid bridge). With a Weber number of $We \ll 1$ and a Capillary number of $Ca \ll 0.1$, it was concluded that our experimental results were not affected by inertial or viscous effects (173).

3.2.2 Modelling Liquid Bridge between Two Fibers

Stretching of a liquid bridge between two fibers can be considered as a quasi-static process (until before the spontaneous detachment), and it can be simulated by an energy minimization algorithm like the one implemented in the finite element based Surface Evolver (SE) software (174). SE computes the equilibrium shape of a liquid body by minimizing the total potential energy of the system given as

$$E = \sigma A_{la} - \sigma \cos\theta_{YL} \iint_{A_{sl}} dA + g \iiint_{V_l} z \rho dV \tag{3.1}$$

Here, A_{la} is the area of the liquid-air interface (LAI), A_{sl} is the area of the solid-liquid interface (SLI), V_l is the volume of the liquid bridge, and g is the gravitational acceleration. It can be seen from Eq. 3.1 that, the total potential energy is the sum of the surface and gravitational energies (gravity needs to be included in the calculations for the range of droplet volumes considered here, 0.5 µL to 7.5 µL). The simulations start with a rectangular cuboid-shaped liquid body placed on two fibers. SE computes the energy of the LAI by computing the area of the LAI. It also calculates the area of the SLI A_{sl} to obtain the contribution of each fiber in the total energy of the system. The SLIs are constrained to remain on the cylindrical surface of the fibers. With SE, one can derive a

path integral to account for the fiber-liquid interfacial area A_{sl} for each fiber and to compute fiber's contribution to the total energy of the system. For the case of two parallel fibers, the path integral for the contribution to the total potential energy due to A_{sl} can be written as,

$$E_{sl} = \sigma \cos\theta_{YL} \oint_{\partial A_{sl}} \left[\frac{yz}{\sqrt{x^2+z^2}} \hat{i} + \frac{yx}{\sqrt{x^2+z^2}} \hat{k} \right] . d\hat{l} - \frac{\rho g}{2} \oint_{\partial A_{sl}} yz^2 dx \tag{3.2}$$

For the case of orthogonal fibers, Eq. 3.2 was used to compute E_{sl} for the lower fiber. The path integral for E_{sl} for the upper fiber can be written as,

$$E_{sl} = \sigma \cos\theta_{YL} \oint_{\partial A_{sl}} \left[\frac{xz}{\sqrt{y^2+z^2}} \hat{j} + \frac{yx}{\sqrt{y^2+z^2}} \hat{k} \right] . d\hat{l} + \frac{\rho g}{2} \oint_{\partial A_{sl}} xz^2 dy \tag{3.3}$$

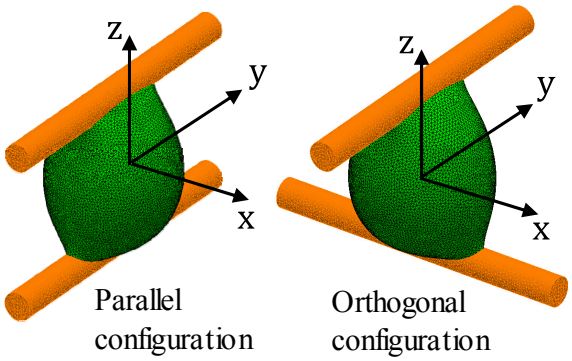

Fig. 3.2: Liquid bridge 3-D shape obtained from SE simulations for a water-glycerol droplet with a volume of $V_l = 3.5$ µL between two fibers in parallel and orthogonal configurations. Fiber radius, YLCA and fiber-fiber spacing are $r_f = 190.5$ µm, $\theta_{YL} = 70^o$, and $s = 2100$ µm respectively.

SE needs to satisfy a constant-volume constraint (input) for the liquid bridge while minimizing the energy of the system. The volume under the LAI is computed by SE through computing the volumes of the vertical prisms formed between each facet of the LAI and the $z = 0$ plane. In order to compute the volume of the liquid bridge V_l, SE needs to subtract the part of the volume of these vertical prisms from the total volume under the

LAI. Since, the SLI was not represented by facets in the simulations, a path integral was then derived to find the volume under the LAI occupied by each fiber. For the case of parallel fibers, we obtain,

$$V_s = \oint_{\partial A_{sl}} zydx \tag{3.4}$$

For the case of orthogonal fibers, we used Eq. 3.4 for the lower fiber, and use Eq. 3.5 for the upper fiber.

$$V_s = \oint_{\partial A_{sl}} zxdy \tag{3.5}$$

Equations 3.2–3.5, allow SE to obtain an equilibrium shape for a liquid bridge with a volume of V_l between the two fibers (see Figure 3.2). In this figure, we considered a water-glycerol mixture (15% by weight) droplet with a volume of $V_l = 3.5$ μL on two fibers with a fiber–fiber spacing of $s = 2100$ μm, a fiber diameter of $r_f = 190.5$ μm, and an YLCA of $\theta_{YL} = 70^o$.

3.3 Physics of Liquid Bridge Between Fibers

Capillary bridge between two cylinders (filaments/fibers) in parallel configuration was first investigated by Princen (161) and later, by Wu et al. (165) and Protiere et al. (162) in the absence of gravity. The two main morphologies observed in these investigations were the barrel-shaped droplet (where droplet completely engulfs the two fibers) and the droplet-bridge (where the droplet partially wraps around the fibers). Figure 3.3 shows experimental and computational images of a liquid bridge with a volume of 3.5 μL between two fibers with a radius of 190.5 μm and a YLCA of $\theta_{YL} = 70^o$ in parallel (Figs. 3.3a and 3.3b) and orthogonal (Figs. 3.3c and 3.3d) configurations. It can be seen for the

case of parallel fibers that an asymmetric (about the y-z and x-y planes) droplet-bridge is formed at a small fiber spacing of $s = 600\ \mu m$. In an earlier study by Farmer and Bird (175), asymmetric droplet-bridge between two spherical particles were reported but in the absence of gravity. This indicates that gravity cannot be the main factor responsible for the observed asymmetry about the y-z plane (the asymmetry about the x-y plane is due to gravity). The asymmetric shape in fact corresponds to the lowest energy state for the fiber–droplet system at the given spacing. As the fiber spacing was increased, droplet-bridge penetrated more into the space between the fibers, although the asymmetry with respect to the y-z and x-y planes sustained till $s < 1500\ \mu m$. Further increase in spacing from $s = 1500\ \mu m$ to $s = 2400\ \mu m$ resulted in the droplet-bridge becoming symmetric about the y-z plane but still remaining asymmetric with respect to the x-y plane. Note in this range of spacing that, the bridge becomes narrower on the top, which is in qualitative agreement with the work of Sun et al. (176) on liquid bridge between two parallel fibers.

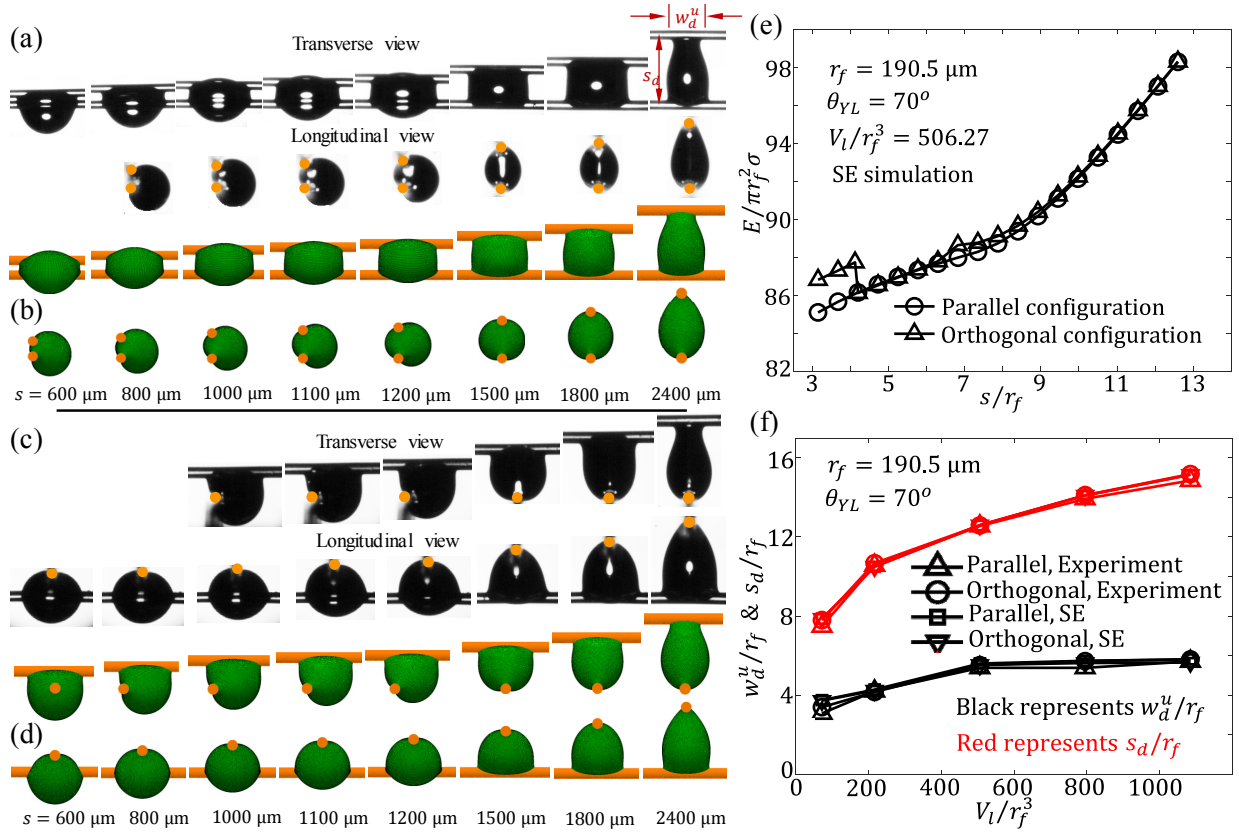

Fig. 3.3: Variation of liquid bridge 3-D shape with fiber-fiber spacing is obtained: (a) from experiment in parallel position; (b) from simulation in parallel position; (c) from experiment in orthogonal position; and (d) from simulation in orthogonal position. In all the cases $r_f = 190.5$ μm, $\theta_{YL} = 70^o$, $V_l = 3.5$ μL, and the liquid is a water-glycerol mixture (15%). Droplet energy versus spacing is given in (e). Final droplet width on the upper fiber w_d^u and final fiber-fiber spacing s_d are also given in (f) versus droplet volume.

Figures 3.3c and 3.3d show the evolution of the same droplet but when the fibers are orthogonal to one another. The shape of the liquid bridge in this case was neither a barrel-shaped droplet nor a droplet-bridge for $s \le 750$ μm, and so we refer to it as the semi-barrel droplet in this paper. The semi-barrel droplet was not imaged (although observed) during the experiment due to difficulty in capturing images from a longitudinal view at small fiber spacing. Our numerical simulation results revealed a transition from the semi-barrel droplet to the droplet-bridge at a spacing of about $720\ \mu\text{m} < s < 780\ \mu\text{m}$. This transition was also noted in the evolution of the energy of the system as a function of fiber–fiber spacing

(only the case of orthogonal fibers) in Figure 3.3e. Overall, depending on the geometrical and wetting properties of the given droplet–fibers system, one of the barrel-shaped droplet, semi-barrel droplet, or droplet-bridge configurations can be expected to prevail.

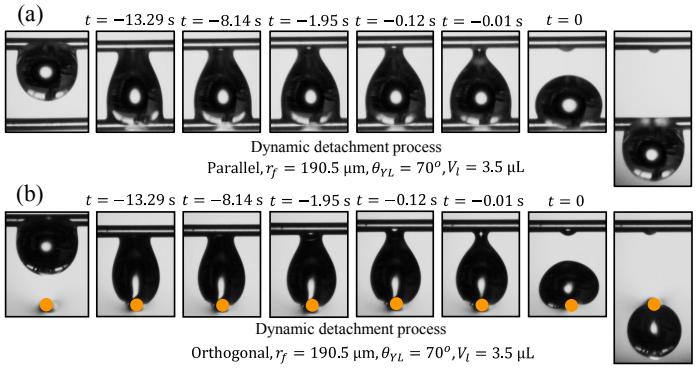

Fig. 3.4: Spontaneous detachment process for parallel (a) and orthogonal (b) fiber configurations for $r_f = 190.5$ μm , $\theta_{YL} = 70^o$, and $V_l = 3.5$ μL .

For the experiment reported in Figure 3.3 (parallel and orthogonal fiber configurations), the liquid bridge becomes unstable for $s > 2400$ μm . This starts by droplet changing its shape spontaneously with no further increase in the fiber–fiber spacing, leading to detachment from the upper fiber. Images in the last column on the right side of Figures 3.3a-3.3d show the final equilibrium state of the liquid bridge between the fibers. Any increase in the fiber–fiber spacing results in liquid bridge detachment from the upper fiber (gravity helps the liquid to remain on the lower fiber). The final fiber–fiber spacing s_d and bridge width (on the upper fiber) w_d^{μ} are measured and shown in Figure 3.3f for both parallel and orthogonal fiber configurations. Figure 3.4 shows the dynamic detachment process for the liquid bridge shown in Fig. 3.3. It can be seen that the dynamic detachment process accelerates as the liquid bridge proceeds towards the detachment.

3.4 Force Balance Analysis

Figure 3.5a shows a free body diagram for a liquid bridge between two parallel fibers. The upward force is the total reaction force N_1 from the upper fiber. The downward forces are the weight of the liquid bridge $\rho V_l g$ and the reaction force N_2 from the lower fiber. Here, N_1 and N_2 represent the net reaction force. Due to the static equilibrium assumption for the liquid bridge, one can write (159,160),

$$N_1 = N_2 + \rho V_l g = F \tag{3.6}$$

To avoid confusion, the forces acting on the upper and lower fibers are denoted here as $F^u = F$ and $F^l = F - \rho V_l g$, respectively. The force acting on the liquid bridge can also be calculated at any fiber–fiber spacing by taking the derivative of the total potential energy of the droplet $E(s)$ i.e.

$$F(s) = \frac{dE}{ds} \tag{3.7}$$

Note that the force obtained from Eq. 3.7 is the force between the liquid bridge and the upper fiber since the gravity is downward. The vertical force exerted by the liquid bridge on the fibers is the resultant of the forces from three different sources. One is the vertical component of the surface tension force acting along the contact line, the other is the force due to Laplace pressure, and the last one is the buoyancy force (fiber's partial submersion in liquid bridge) (160). Note that as will be shown later in the next section, the contribution of buoyancy force in the interfacial force between a droplet and a fiber is quite negligible near the onset of dynamic detachment process. The total force acting on each fiber can be described as,

$$F^i = \sigma \int_{L^i} \cos\alpha^i(l)dl - A_p^i \Delta P^i \pm \rho V_b^i g \tag{3.8}$$

where $i = l$ or u, and α is the angle between the direction of the capillary force at each point on the contact line and the vertical direction (see Fig. 3.5b), A_p is the projected wetted area (see Fig. 3.5c), L is the length of the contact line (see Fig. 3.5d), ΔP is the droplet pressure near the fiber, and V_b is the volume of the submerged fiber (see Fig. 3.5c). The upper and lower planes shown in Fig. 3.5b were considered for calculating pressures ΔP^u and ΔP^l on the upper and lower fibers, respectively.

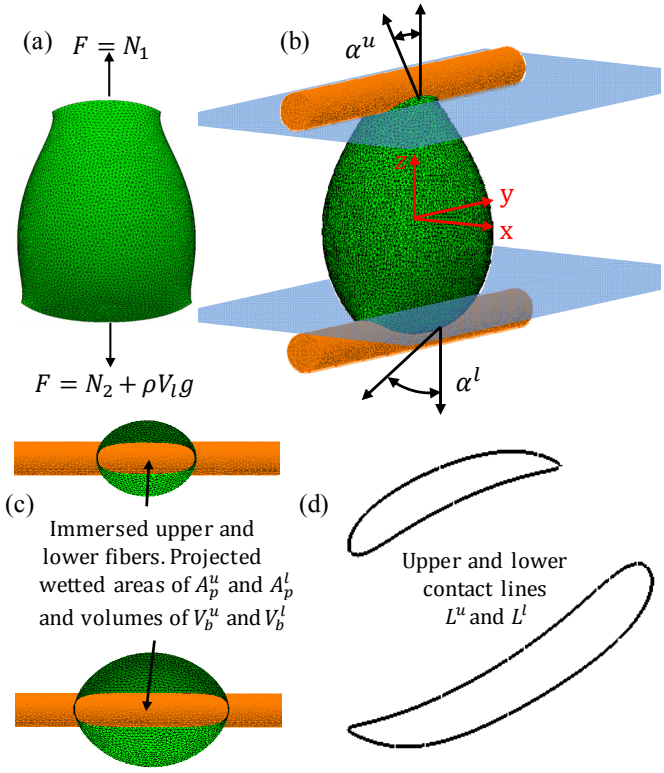

Fig. 3.5: A free body diagram for a liquid bridge between two parallel fibers is shown in (a). The immersion angle α for the upper and lower fibers, the panes at which the pressure forces are calculated are shown in (b). Wetted area and three phase contact line are shown in (c) and (d) respectively, for the upper and lower fibers.

3.5 Results and Discussion

3.5.1 Liquid Bridge between Similar Fibers

We start this section by studying the effects of fiber–fiber spacing on the net force between the bridge and fibers for a system with a fiber diameter of $r_f = 190.5\ \mu\text{m}$, a YLCA of $\theta_{YL} = 70^o$, and a droplet volume of $V_l = 3.5\ \mu\text{m}$. Recall from the previous section that the liquid bridge between two fibers may have an asymmetric profile about the vertical planes passing through the fiber's axis when the spacing is small (leading to droplet morphological transitions).

Moreover, the liquid bridge between two closely-spaced parallel fibers has a tendency to slowly (but continuously) spread along the fibers in the form of a narrow liquid sheet. This prolongs the time to reach equilibrium and adds errors to the experiments (144,177). For these reasons, we focused our experiments on the range of fiber–fiber spacing at which the droplet-bridge remains symmetric about the vertical planes passing through the fibers ($1500\ \mu\text{m} \le s \le 2400\ \mu\text{m}$ here). Figures 3.6a and 3.6b show the forces on the upper fiber for the parallel and orthogonal fiber configurations, respectively. It can be seen that the interfacial force between a bridge and the upper or lower fiber increases with increasing the spacing between the fibers. Good general agreement can be seen between the experimental and computational forces for all cases considered (upper and lower fibers in parallel and orthogonal configurations).

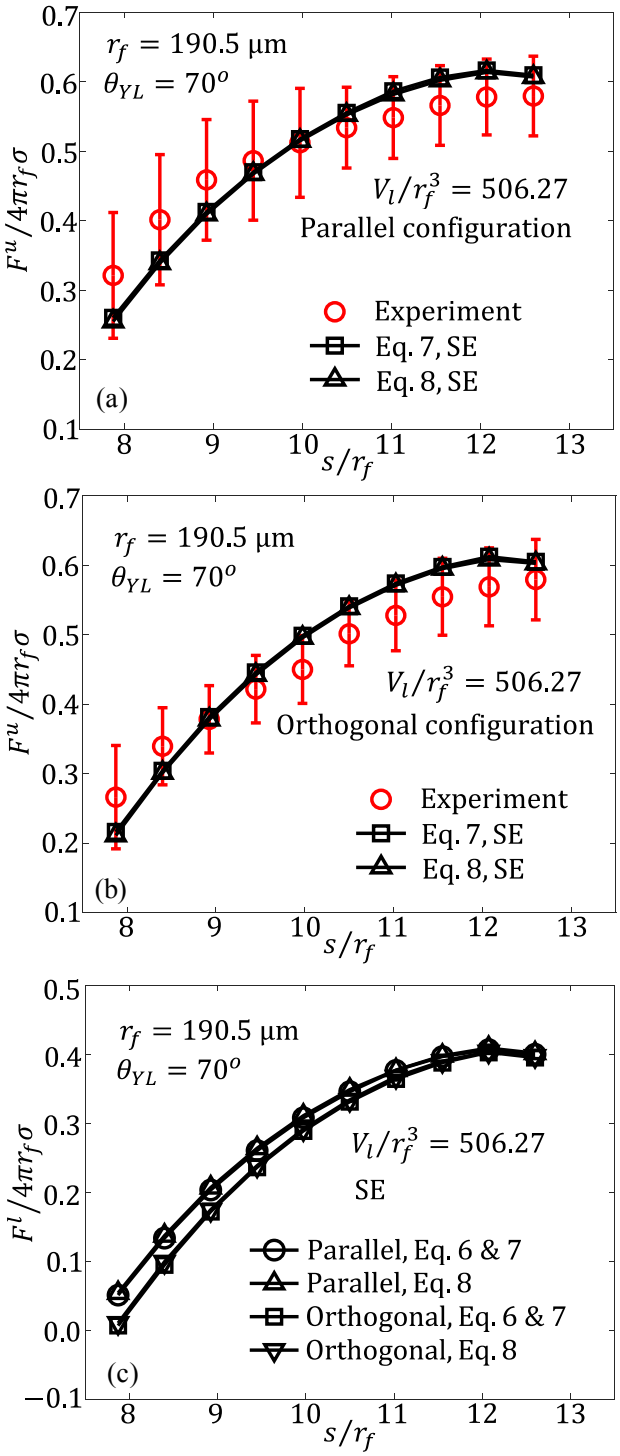

Fig. 3.6: Interfacial force between the upper fiber and the liquid bridge versus fiber spacing for fibers in parallel (a) and orthogonal (b) configurations. (c) Interfacial forces between the lower fiber and the liquid bridge versus fiber spacing. For all the cases, $r_f = 190.5$ μm, $\theta_{YL} = 70^o$, and $V_l = 3.5$ μL with the water-glycerol (15%) mixture as the liquid.

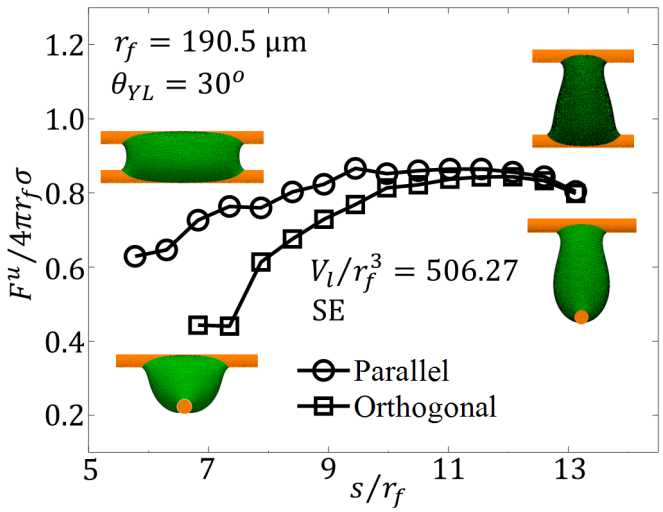

Fig. 3.7: Interfacial force between the upper fiber and the liquid bridge versus fiber spacing for fibers in parallel and orthogonal configurations with $r_f = 190.5$ μm, $\theta_{YL} = 30^o$, and $V_l = 3.5$ μL with water-glycerol (15%) mixture as the liquid.

To ensure the accuracy of our force analysis, we considered both the energy approach of Eq. 3.7 and the force balance method of Eq. 3.8, and they both methods produced identical predictions, as can be seen in Figures 3.6a–3.6c). Note in these figures that detachment force is the same for parallel and orthogonal fiber arrangements (see Fig. B1 in the Appendix B for detailed data analysis). Our results also revealed that contribution of the buoyancy force in the detachment force is generally less than 1% (see Fig. B1e in the Appendix B). For this reason, buoyancy is not considered in our detachment force calculations in this work.

We also considered a bridge between two more hydrophilic fibers ($\theta_{YL} = 30^o$) to confirm the above-mentioned behavior. It can interestingly be seen in Figure 3.7 that F^u follows two different paths for the case of parallel and orthogonal fibers, but they eventually reach the same point right before the start of the spontaneous detachment process (at $s \approx 2500$ μm for this case).

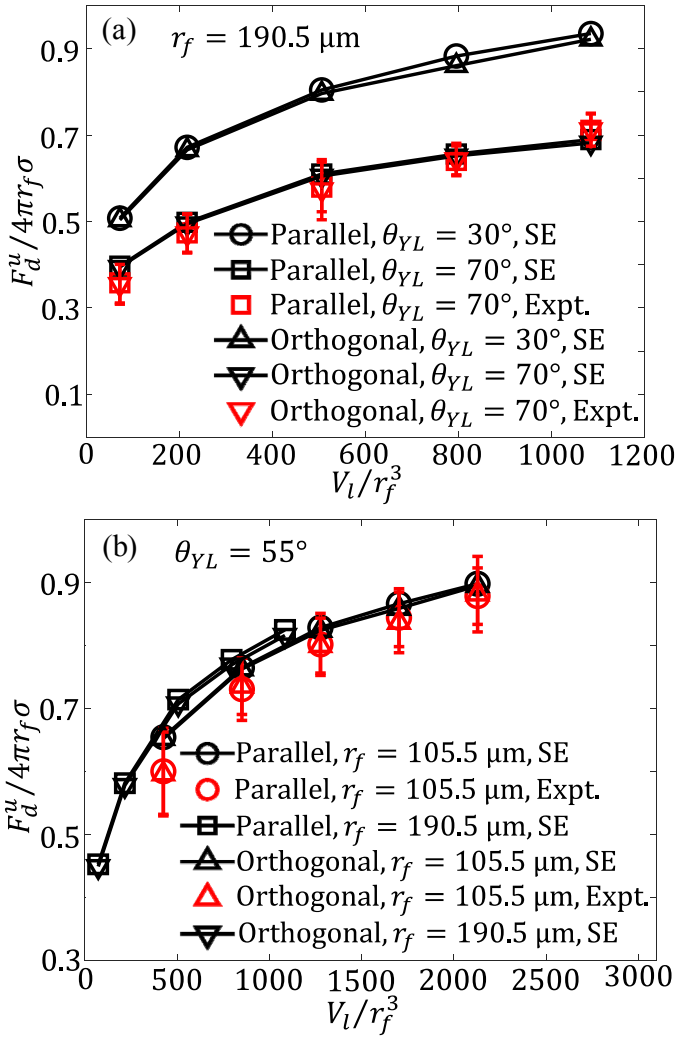

Fig. 3.8: Detachment force F_d^u (non-dimensionalized by $4\pi\sigma r_f$) versus liquid volume for different θ_{YL} (a) and fiber radius r_f (b) with water-glycerol (15%) mixture as the liquid.

Referring to the force applied to the upper fiber at the moment of detachment as F_d^u, Figure 3.8a shows detachment force versus droplet volume for parallel and orthogonal fibers with two different YLCAs of $\theta_{YL} = 30^o$, and $\theta_{YL} = 70^o$ but a radius of $r_f = 190.5$ µm. It can again be seen that detachment force does not depend on the orientation of the fibers relative to each other (liquid bridge detached from the upper fiber in all cases reported in Figure 3.8a). The detachment force between the liquid bridge and the fibers depends on the length of the contact line, angle between the direction of surface tension force and the

vertical direction, droplet pressure, and the projected wetted area of the fibers at $s = s_d$ (see Fig. B2 and related discussions in Appendix B for a detailed data analysis).

It can be seen that the detachment force increases with increasing the YLCA. Detachment force was also measured experimentally for fibers having a YLCA of $\theta_{YL} = 55^o$ (with $r_f = 105.5\ \mu\text{m}$), and the results are added to Figure 3.8b. Excellent agreement can again be seen between the experimental and computational results.

3.5.2 Liquid Bridge between Dissimilar Fibers

In this section, we present our results for a liquid bridge between fibers having different radius and/or YLCAs. To do so, we considered an upper fiber with a radius of $r_f^u = 105.5\ \mu\text{m}$ and a YLCA of $\theta_{YL}^u = 55^o$, but a lower fiber with a radius of $r_f^l = 190.5\ \mu\text{m}$ and a YLCA of $\theta_{YL}^l = 70^o$.

Figure 3.9a shows examples of a liquid bridge with a volume of $V_l / r_f^{u3} = 2129$ between the above-mentioned fibers from experiment and simulation at the moment of detachment. Figure 3.9b shows the detachment force for liquid bridges of different volumes in parallel and orthogonal fiber configurations. The figure also includes detachment force obtained using a lower fiber identical to the upper fiber for comparison. It can be seen that detachment force does not depend on the relative angle between the fibers or on the radius and YLCA of the lower fiber, as long as the detachment is from the upper fiber. Additional computational data are given in the Appendix B (see Fig. B3) in support of the results shown in Figure 3.9b. However note that, if the lower fiber is much bigger in

diameter (or is much more hydrophilic) than the upper fiber, then the detachment may happen at a smaller spacing. This was observed in a series of SE simulations conducted for the same upper fiber but a lower fiber with a radius of $r_f^l = 500$ μm and a YLCA of $\theta_{YL}^l = 30^o$ for a liquid volume in the range of $425.8 \le V_l / r_f^{u3} \le 2129$.

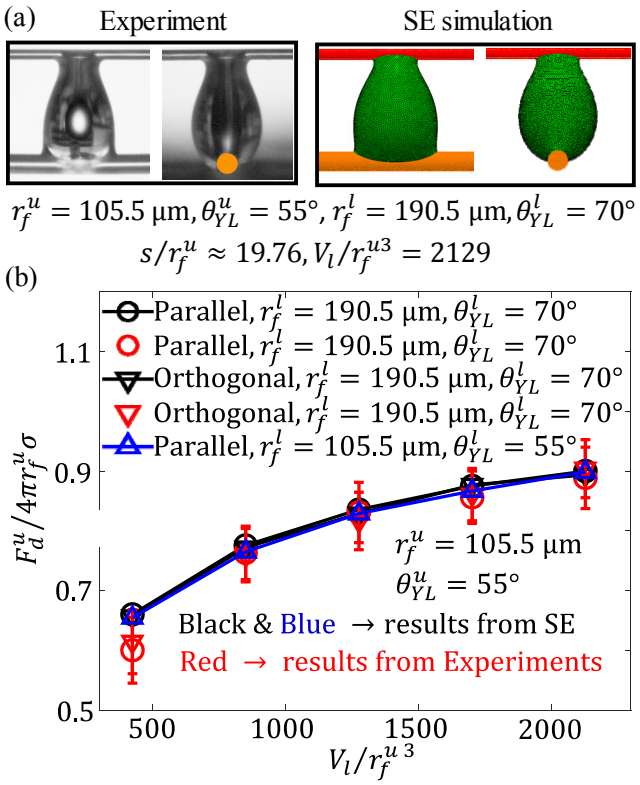

Fig. 3.9: (a) Liquid bridge between parallel and orthogonal dissimilar fibers having different radius and wettability from experiment and simulation. (b) Detachment force F_d^u (non-dimensionalized by $4\pi\sigma r_f^u$) vs normalized liquid volume for the upper and lower fibers with different properties.

The detachment force can be regarded as an attribute of the fiber that determines whether or not a droplet originally on the upper fiber will move to the lower fiber after detachment. While a droplet would obviously move to the lower fiber after detachment when the fibers are identical (due to gravity), the same cannot be said for when the fibers have different physical and wetting properties. The latter depends on the interfacial forces

between the droplet and the upper or lower fibers. In fact, if the detachment force of the upper fiber is greater than the sum of the detachment force of the lower fiber and the weight of the droplet (i.e., $F_d^u > F_d^l + \rho V_l g$), then the droplet most probably remains on the upper fiber after detachment.

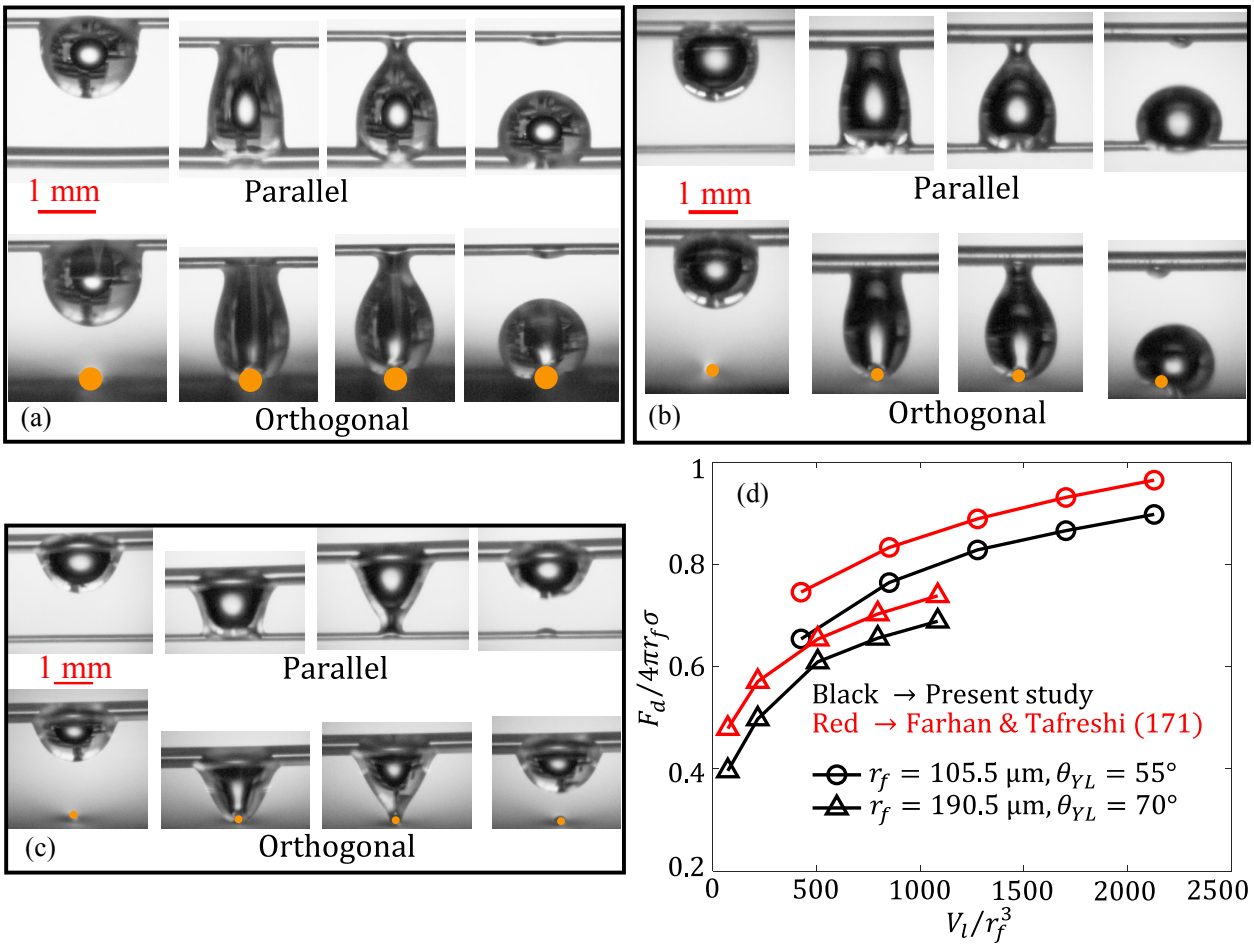

Fig. 3.10: Droplet transfer between the upper and lower fibers for the case of $r_f^u = 105.5$ μm , $\theta_{YL}^u = 55^o$, $r_f^l = 190.5$ μm , and $\theta_{YL}^l = 70^o$ (a), $r_f^u = 190.5$ μm , $\theta_{YL}^u = 70^o$, $r_f^l = 105.5$ μm , and $\theta_{YL}^l = 55^o$ (b), $r_f^u = 264.1$ μm , $\theta_{YL}^u = 30^o$, $r_f^l = 105.5$ μm , and $\theta_{YL}^l = 55^o$ (c). Comparison between the detachment forces obtained in the present study and those of the correlation of Farhan and Tafreshi (171) is given in (d).

Consider a liquid bridge with a volume of $V_l = 2.5$ μL between an upper fiber with $r_f^u = 105.5$ μm and $\theta_{YL}^u = 55^o$, and a lower fiber with $r_f^l = 190.5$ μm and $\theta_{YL}^u = 70^o$ (Figure 3.10a).

In this case, detachment forces for the upper and lower fibers can be found to be $F_d^u = 84.72$ μN and $F_d^l = 97.6$ μN, respectively. The droplet therefore remains with the lower fiber after detachment. Swapping the fibers, will not change this outcome as $F_d^u = 97.6$ μN will still be smaller than $F_d^l + \rho V_l g = 84.72 + 25.48$ μN $= 110.2$ μN, as can be seen in Figure 3.10b). Figure 3.10c however shows the case where the same droplet is placed between an upper fiber with $r_f^u = 264.1$ μm and $\theta_{YL}^u = 30^o$, and a lower fiber with $r_f^l = 105.5$ μm and $\theta_{YL}^l = 55^o$. The detachment force for upper fiber is now $F_d^u = 142.2$ μN which is greater than $F_d^l = 84.72$ μN plus the weight of the droplet (i.e., $84.72 + 25.48$ μN $= 110.2$ μN), and so the droplet remains on the upper fiber. It is therefore evident that the outcome of a liquid bridge detachment experiment can be predicted using quantitative information about the detachment force of the individual fibers.

In a recent study, Farhan and Tafreshi (171) proposed a correlation to predict the force required to detach a pendent droplet from a fiber (see also the work of Ojaghlou et al., 178 and Aziz et al., 170). Since the detachment force investigated in the present study depends mainly on the properties of the fiber from which the droplet detaches, we compared our results with the detachment force values from the correlation of Farhan and Tafreshi (171) in Figure 3.10d. It can be seen that the detachment forces obtained in the present study are about 15–20% lower than those obtained from the above correlation. This difference can be attributed to the differences between the shape of a detaching pendent droplet and that of a detaching liquid bridge. Nevertheless, given the close agreement between the two, the correlation of Farhan and Tafreshi (171) is used in this study to predict if a droplet resulting from liquid bridge detachment remains on the upper

fiber or if it moves to the lower fiber. In other words, we expect the droplet to remain on the upper fiber if the following criterion is satisfied.

$$\left(\frac{r_{ref}}{r_f^u}\right)^2 \frac{\sigma}{\sigma_{ref}}\left(1+\cos\theta_{YL}^u\right)\varphi\left(\frac{V_l}{r_f^{u3}}\right)^{\xi}\left(1-\frac{R_r^{2+3\xi}}{R_\theta}\right) > g \qquad (3.9)$$

Here $\varphi = 3894$, $\xi = -0.84$, $\sigma_{ref} = 0.0649$ N/m, $r_{ref} = 190.5\times10^{-6}$ m, $R_r = r_f^u / r_f^l$, and $R_\theta = \frac{\left(1+\cos\theta_{YL}^u\right)}{\left(1+\cos\theta_{YL}^l\right)}$.

Equation 3.9 can be of great significance to applications like fog harvesting (1,2,43), coalescence filtration (3,11,30,137-140) and membrane desalination (179-183) among many others (127,128,112-114,143-145), where liquid droplets have to travel through a network of vibrating and/or deforming fibers, and where the rate of droplet transport depends on how the fibers compete for the droplet (in the presence of gravitational and/or a hydro/aerodynamic fields).

3.6 Conclusions

Experiment and numerical simulation were devised to study a liquid bridge formed between two parallel or orthogonal fibers with similar or dissimilar geometrical or wetting properties. It was quantitatively shown that the 3-D shape of the liquid bridge and its interactions with the fibers vary significantly with varying the spacing between the fibers. Focusing on the transition from a liquid bridge in equilibrium to one that is detaching from one of the fibers spontaneously, it was shown that the relative angle between the fibers does not affect the outcome of a liquid bridge detachment (i.e., the fiber–fiber spacing at which detachment occurs is independent of the angle between the fibers). It was also shown that the liquid bridge detaches from the fiber that provides a weaker capillary force (after factoring the weight of the liquid), and the force needed for

detachment does not strongly depend on the size or the YLCA of the other fiber (as long as it provide a larger capillary force, of course). It was also shown that a mathematical criterion can be developed to predict which of the two fibers accommodating a liquid bridge will take the droplet that is resulted from the bridge detachment.

In the previous and present chapters we presented our investigations on the detachment of a droplet from a fiber and the detachment of a liquid bridge between two fibers, respectively, which are interesting physical processes. They are also relevant to many important applications such as coalescence filtration, fog harvesting, fuel cells and many more. For example, in coalescence filtration liquid droplet detaches from a porous medium composed of multiple layers of fibers which is an extremely complex process. So, we chose to investigate the simple versions of this problem to start with. The experimental and computational methods used in the current study can be extended to investigate the more complex problem of droplet detachment from a porous medium composed of multiple layers of fibers. The results obtained in the present investigations help us to understand the basic mechanism of droplet-fiber interaction. In the previous chapter it was shown how the droplet detachment residue changed with fiber radius and YLCA of the fiber. In the current chapter we showed how the detachment force changed with the fiber radius and YLCA of the fiber. These qualitative relations should be true for the case of droplet detaching from multiple layers of fibers. Effects of the length of the contact line and wetted area of the fibers on the detachment force can be obtained from the numerical simulations performed in the current chapter. These qualitative relations should also be true for the case of droplet detaching from multiple layers of fibers

It should be noted that in the applications like coalescence filtration, the fibers are randomly arranged. It is almost impossible to measure accurately the length of the contact line and the wetted area for a droplet to be detached from it. So, it is almost impossible to predict the detachment force accurately for a droplet detaching from a porous medium composed of randomly arranged fibers beforehand. However, we can obtain an approximate value of the detachment force required to detach a droplet from a porous medium composed of randomly arranged fibers. For example we want to get an approximate value of the force required to detach a water (with 15% glycerol) droplet of volume 2.5 μL from a porous medium composed of randomly arranged fibers having fiber radius $r_f = 105.5$ μm and YLCA 55º. Assuming that the droplet is of spherical shape (with volume $\frac{4}{3}\pi r_l^3$), the radius of the droplet is $r_l = 841.95$ μm. So, the maximum number of fibers the droplet can be in touch with is $r_l / r_f = 841.95 / 105.5 \approx 8$. We already know from the present study that the force required to detach a water (with 15% glycerol) droplet of volume 2.5 μL from a fiber of radius 105.5 μm and YLCA 55º is around $F_d = 84.72$ μN. It can be said that the maximum force required to detach the droplet from the given fibrous medium will be 8×84.72 μN $= 677.76$ μN. It should be noted that this is the maximum possible detachment force and actual detachment force can be significantly lower than this value (140). However, we have an estimate of the detachment force value which is almost impossible to predict accurately beforehand.

There are many other factors that can affect the detachment force value and detachment residue volume e.g. inhomogeneity in the distribution of fibers, roughness of the fiber surface which may promote pinning of the contact line, complex arrangement of fibers

which may make the shape of the contact line very complicated. It is a challenging task to include the effects of these factors in the detachment force and residue volume calculations. This should be the motivation to design more sophisticated experiments and develop more accurate mathematical models in future.

Chapter 4. Modeling Cassie Droplets on Superhydrophobic Coatings with Orthogonal Fibrous Structures

4.1 Introduction

Superhydrophobic surfaces are generally known for their ability to provide droplet contact angles (CAs) in the neighborhood of 150 degrees, and they are often produced by imparting roughness to a hydrophobic surface (53–57). There are two main stable wetting states for a droplet residing on a rough surface, the Wenzel state and the Cassie state (45–48). The Wenzel state corresponds to the state where the surface asperities are completely submerged in the droplet, whereas the Cassie state represents the condition where a layer of air is trapped underneath the droplet between the peaks of the surface protrusions (49–52). There are also some other wetting states in between or related to these two extreme states e.g., as impregnated Cassie state or rose petal state (45).

While numerous studies have been focused on lowering the cost of micro-fabrication, manufacturing micro- or nano-roughness has remained a costly process. Moreover, adding microfabricated roughness to a surface with arbitrary or random curvatures is still a challenge. An alternative approach (amongst many other methods) has therefore been to impart comparable superhydrophobic behavior to a surface by coating the surface with fibers from a hydrophobic polymer (58–62). Fibrous coatings usually consist of layers of planar fibers deposited on top of one another in a random fashion. Coatings with random fiber orientations however, do not provide directionality to the mobility of a droplet over the surface. It is expected that controlling the orientation of the fibers in a coating can potentially provide some degrees of control over a droplet mobility on a surface. In fact, it has been shown that droplet can maintain different

apparent CAs in different directions on a surface made of parallel grooves for instance, indicating preferential droplet mobility along the grooves (63–72). While producing a fibrous coating made of parallel fibers that can resemble a grooved surface is not a challenge, controlling the porosity and uniformity of such coatings is quite hard as the fibers tend to pack relatively densely in a thin layer. A possible solution that helps with increasing the spacing between the fibers is to alternate the orientation of the fibers between the x- and y-directions during the spinning process. Coatings with orthogonally layered fibers tend to have a much higher porosity than their unidirectional counterparts and have been shown to exhibit unique properties for various applications (73-78,86). Unfortunately, coatings with orthogonal fibers may not necessarily perform like an anisotropic surface depending on the size and surface tension of the droplets, diameter and spacing of the fibers, and the Young–Laplace contact angle (YLCA) of the fiber polymer, as will be discussed later in this paper.

Figure 4.1a shows a two-layer Polystyrene coating comprised of orthogonally oriented fibers with an average diameter of about 5 μm. As can be seen in the inset figure, such coatings tend to exhibit large CAs in the neighborhood of 150 degrees (droplet volume is 0.5 μl). Figure 4.1b shows water droplet CA on different Polystyrene coatings with having the same average fiber diameter but different average fibers spacing. Note that as fiber spacing varies significantly across each coating, we used solid area fraction (SAF) to characterize the density of the fibers in each coating (see (89) for more information on obtaining SAF values from SEM images) as the best alternative, although we recognize that fiber spacing and SAF are only weakly correlated. The experimental measurements given in this figure indicate that apparent contact angle generally decreases with increasing SAF but the trend is not monotonic due to variety of reasons,

some of which will be discussed later in this chapter. In this chapter, we study how fiber diameter and fiber spacing can cause a droplet on a coating with orthogonal fibers departs from the Cassie state, and provide analytical expression for such transition whenever possible. Such information can be quite useful in design superhydrophobic fibrous surfaces for variety of applications such as self-cleaning and anti-icing.

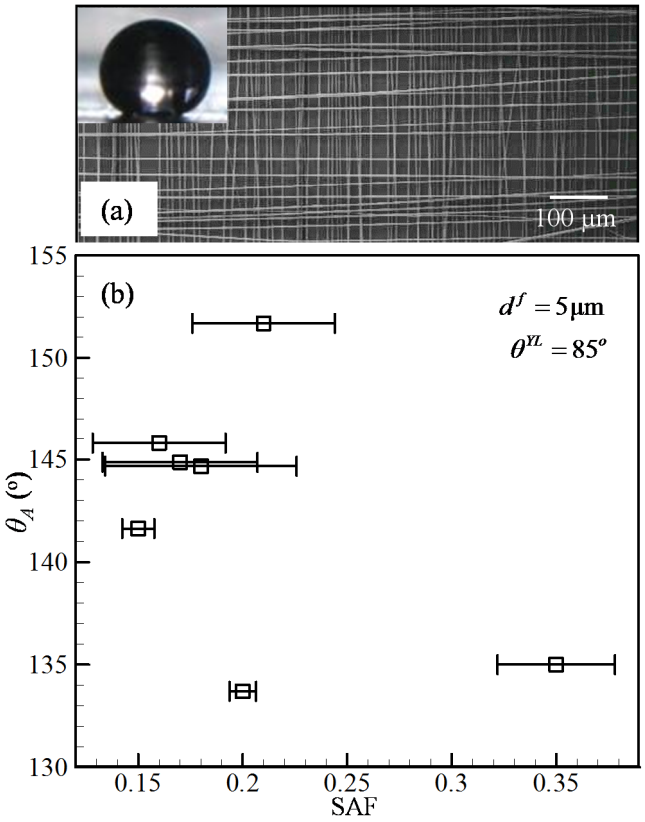

Fig. 4.1: (a) An example SEM image of an electrospun superhydrophobic Polystyrene coating with two layers of orthogonal fibers. (b) Apparent CA measured using a 0.5 µl water droplet for coatings with different solid area fractions. Average fiber diameter was measured to be 5 µm.

The remainder of this chapter is organized as follows. Section 4.2 presents our force balance method used to predict the stability of the air–water interface (AWI) underneath a droplet deposited on a coating. Section 4.3 describes our numerical simulation of droplet shape on fibrous coatings surface using the Surface Evolver (SE) finite element code

(174). Results of our simulations and analytical predictions are given in Section 4.4 followed by our conclusions in Section 4.5.

4.2 Analytical Equations for Air-Water Interface

As mentioned earlier, a droplet deposited on a fibrous coating may be in the Cassie or Wenzel state depending on the volume of the droplet as well as the coating's microstructural parameters. In this section, we derive a set of analytical expressions that can be used to predict the condition where a droplet may departure from the Cassie state.

4.2.1 Balance of Forces on an Air-Water Interface

We start by considering the maximum pressure that an AWI between the fibers of a coating underneath a droplet can tolerate before it fail and wet the coating (partially or completely). We first consider a droplet deposited on a coating made of parallel fibers (see Fig. 4.2).

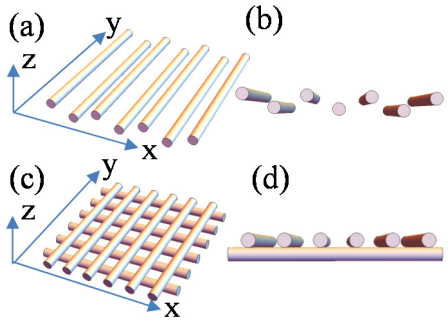

Fig. 4.2: Schematic representation of our virtual coatings made of two layers of parallel (a–b) or orthogonal fibers (c–d).

The AWI between two adjacent parallel fibers is shown schematically in Fig. 4.3a. To make the expressions more general, the fibers are assumed to have different diameters and YLCAs, and are placed in different horizontal planes. The fiber diameter and YLCA are assumed to be d_1^f and θ_1^{YL} for the top layer, and d_2^f and θ_2^{YL} for the bottom layer, respectively. Fiber spacing is assumed

to be the same for both layers for the sake of simplicity. In a plane cutting through the center of the droplet, the AWI can be represented as an arc of a circle (a 2-D approximation). The forces acting on the AWI are the droplet pressure and the capillary forces from the fibers. Writing the balance of these two forces in the direction of z' axis, which passes through the middle of the line AB (see Fig. 4.3a), one can relate the pressure acting on the AWI $P_{FB}^{\parallel}$ to the location of the AWI between the fibers,

$$P_{FB}^{\parallel} = -2\sigma\cos\phi\left\{\frac{\sin\left(\theta_1^{YL}+\alpha_1-\phi\right)+\sin\left(\theta_2^{YL}+\alpha_2+\phi\right)}{s-d_1^f\sin\alpha_1-d_2^f\sin\alpha_2}\right\} \tag{4.1}$$

where, $\phi=\tan^{-1}\left\{\frac{2c+d_1^f\cos\alpha_1-d_2^f\cos\alpha_2}{s-d_1^f\sin\alpha_1-d_2^f\sin\alpha_2}\right\}$ is the angle between the z' axis and the vertical direction, and c is the vertical center-to-center distance between the fibers in the first and second layers. In this equation, α_1 and α_2 are the immersion angles. The maximum pressure that an AWI between two parallel fibers can withstand can be calculated by solving the following coupled equations for α_1 and α_2, and then by substituting these values in Eq. 4.1.

$$\frac{\partial P_{FB}^{\parallel}}{\partial\alpha_1}=0 \;\;\&\;\; \frac{\partial P_{FB}^{\parallel}}{\partial\alpha_2}=0 \tag{4.2}$$

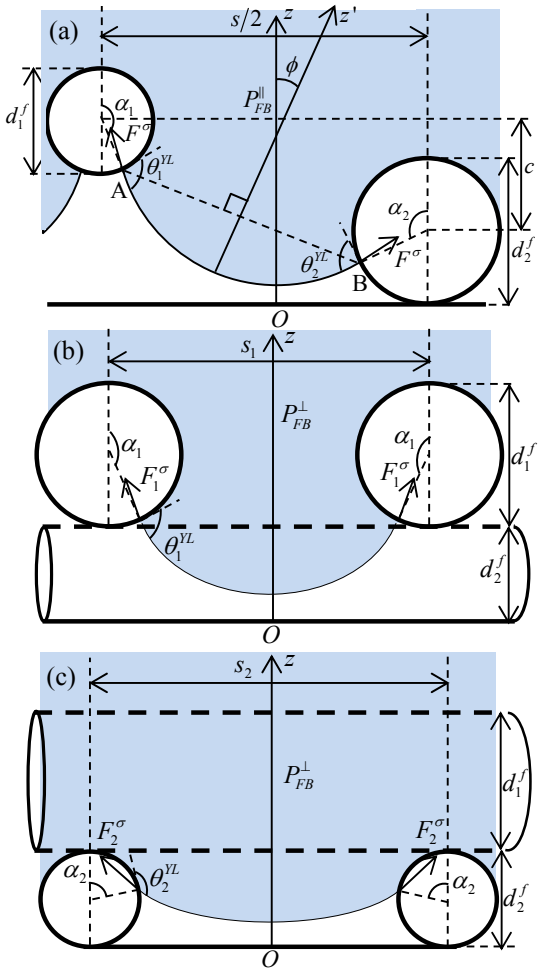

Fig. 4.3: Balance of forces across the AWI for parallel layers of fibers in (a), for orthogonal layers of fibers viewed from a direction along the fibers in the top layer in (b), and for orthogonal layers of fibers viewed from a direction perpendicular to the fibers in the top layer in (c).

Figures 4.3b and 4.3c show a schematic drawing of the AWI in a coating with orthogonal fiber-layers, from two different directions of along and perpendicular to the fibers in the top layer. Once again, one can relate the pressure over the AWI $P_{FB}^{\perp}$ to the location of the AWI between the fibers by writing the balance of force in the vertical direction. In our derivations, the changes in α_1 and α_2 along the length of the fibers were neglected for simplicity. The force in the vertical direction due to droplet pressure can be taken as $P_{FB}^{\perp}\left(s_1 - d_1^f \sin\alpha_1\right)\left(s_2 - d_2^f \sin\alpha_2\right)$. This force is

balanced by the vertical components of fiber capillary forces $2\sigma\left(s_2 - d_2^f \sin\alpha_2\right)$ and $2\sigma\left(s_1 - d_1^f \sin\alpha_1\right)$. From the balance of forces, we obtain,

$$P_{FB}^{\perp} = -2\sigma\left\{\frac{\sin\left(\theta_1^{YL} + \alpha_1\right)}{s_1 - d_1^f \sin\alpha_1} + \frac{\sin\left(\theta_2^{YL} + \alpha_2\right)}{s_2 - d_2^f \sin\alpha_2}\right\} \tag{4.3}$$

where s_1 and s_2 are the center-to-center distance between the fibers in the first and second layers, respectively. Maximum $P_{FB}^{\perp}$ can again be found by taking the derivative of Eq. 4.3 with respect to α_1 and α_2 and by solving the resulting coupled equation using the same approach presented earlier.

It is important to note that an AWI may come into contact with the substrate underneath the fibers at pressures much smaller than those predicted by Eqs. 4.1–4.3 for certain coating geometries (fiber diameters, fiber spacing, or YLCAs). It is also possible that the AWI meets and coalesces with itself inside the coating under the first layer of fibers resulting in partial or complete wetting transition of the coating. These conditions are explained in the next two subsections.

4.2.2 Cassie-to-Wenzel Transition. Mechanism I: Interface Sagging

The first scenario of a droplet transitioning from the Cassie state is when the droplet comes into contact with the hydrophilic substrate underneath the coating before the pressure over its AWI exceeds the coating's maximum capillary pressure (59). Consider a droplet deposited on a coating made of parallel fibers. An AWI between two adjacent fibers is shown schematically in Fig. 4.4a for when the AWI reaches deep into the coating to touch the substrate. It can be shown that the radius of curvature of this AWI $R_{sag}^{f,\parallel}$ can be derived as,

$$R_{sag}^{f,\parallel}=\frac{\left[\left\{\frac{ms^2\zeta_2}{d_1^f}+\frac{1}{d_1^f}\left\{\frac{2c}{d_1^f}-(1-\zeta_1)+m(1-\zeta_2)\right\}\left\{s^2+4c^2+d_1^{f\,2}(m^2-1)+4cmd_1^f\right\}\right\}^{1/2}-\left\{\frac{ms^2\zeta_2}{d_1^f}\right\}^{1/2}\right]^2}{4\left\{\frac{2c}{d_1^f}-(1-\zeta_1)+m(1-\zeta_2)\right\}^2} \tag{4.4}$$

where $m=\frac{d_2^f}{d_1^f}$, $\zeta_i=1-\cos\theta_i^{YL}$ with subscript $i=1,2$ representing the layers and $c\neq 0$ when $d_1^f=d_2^f=d^f$ and $\theta_1^{YL}=\theta_2^{YL}=\theta^{YL}$.

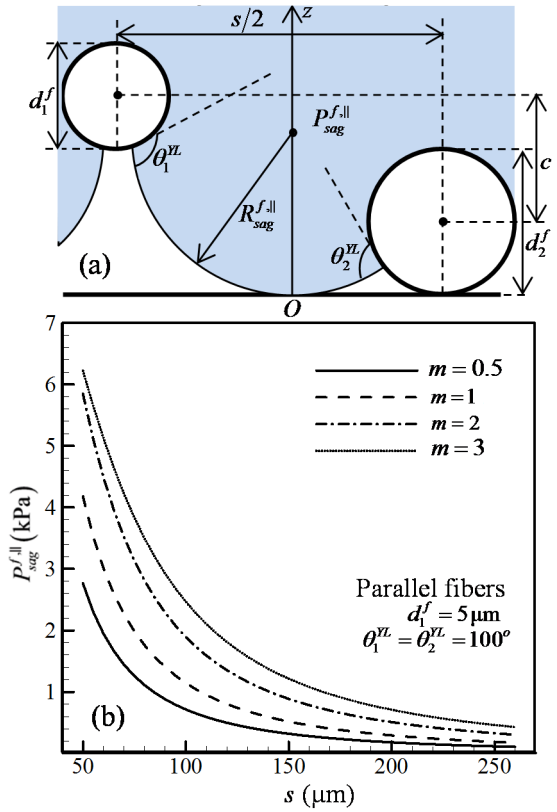

Fig. 4.4: (a) Schematic representation of AWI coming into contact with the substrate for a coating with two parallel layers of fibers. (b) Transition pressure versus fiber spacing in coatings with parallel fiber having different fiber diameter in the top and bottom layers. $\theta_1^{YL}=\theta_2^{YL}=100^o$, $d_1^f=5\,\mu m$.

The AWI's transition pressure $P_{sag}^{f,\parallel}$ can then be obtained from Laplace's theorem,

$$P_{sag}^{f,\parallel}=\frac{\sigma}{R_{sag}^{f,\parallel}} \tag{4.5}$$

Equation 4.4 can significantly be simplified for when the fibers of the top and bottom layers have the same diameters and YLCAs, i.e., $d_1^f = d_2^f = d^f$, $\theta_1^{YL} = \theta_2^{YL} = \theta^{YL}$, and $c = d^f$.

$$R_{sag}^{f,\parallel} = \left[\left\{ \frac{s^2(2+\zeta)}{16 d^f} + d^f \right\}^{1/2} - \left\{ \frac{s^2 \zeta}{16 d^f} \right\}^{1/2} \right]^2 \tag{4.6}$$

For given values of s, d^f and θ^{YL}, transition pressure $P_{sag}^{f,\parallel}$ for an AWI over parallel layers of fibers can be calculated using Eqs. 4.4–4.6. For instance, with $d^f = 10\,\mu\text{m}$, $\theta^{YL} = 85^o$, and $s = 264\,\mu\text{m}$, this pressure becomes equal to the Laplace pressure for a droplet with a volume of $0.524\,\mu\text{l}$. In other words, a droplet with a volume of $0.524\,\mu\text{l}$ will not remain at the Cassie state on such coatings if $s \geq 264\,\mu\text{m}$. Figure 4.4b shows the variation of $P_{sag}^{f,\parallel}$ with s for a surface coated with parallel fibers with different diameters. It can be seen that $P_{sag}^{f,\parallel}$ decreases with increasing fiber spacing, but it increases with increasing the diameter of the fibers in the lower layer.

Figures 4.5a and 4.5b show a schematic illustration for the AWI over a coating with orthogonal fibers from two different views of along and perpendicular to the fibers in the upper layer. These figures are drawn for when the AWI comes into contact with the substrate. Assuming that the AWI in a plane passing through the droplet center is part of an ellipsoid, the radius of curvature of the AWI will be the harmonic mean of the radii of curvature of the circular arcs shown in Figs. 4.5a and 4.5b. Each layer of fibers has a different fiber diameter, fiber spacing, or YLCA. These radii of curvature can be derived to be,

$$R_{sag,1}^{f,\perp} = \frac{\frac{s_1^2}{4 d_1^f} + m^2 d_1^f + m d_1^f}{2m + \zeta_1} \tag{4.7}$$

$$R_{sag,2}^{f,\perp} = \frac{s_2^2}{4d_2^f \zeta_2} \tag{4.8}$$

The transition pressure for the AWI over orthogonal layers of fibers can then be obtained as,

$$P_{sag}^{f,\perp} = \sigma\left(\frac{1}{R_{sag,1}^{f,\perp}} + \frac{1}{R_{sag,2}^{f,\perp}}\right) \tag{4.9}$$

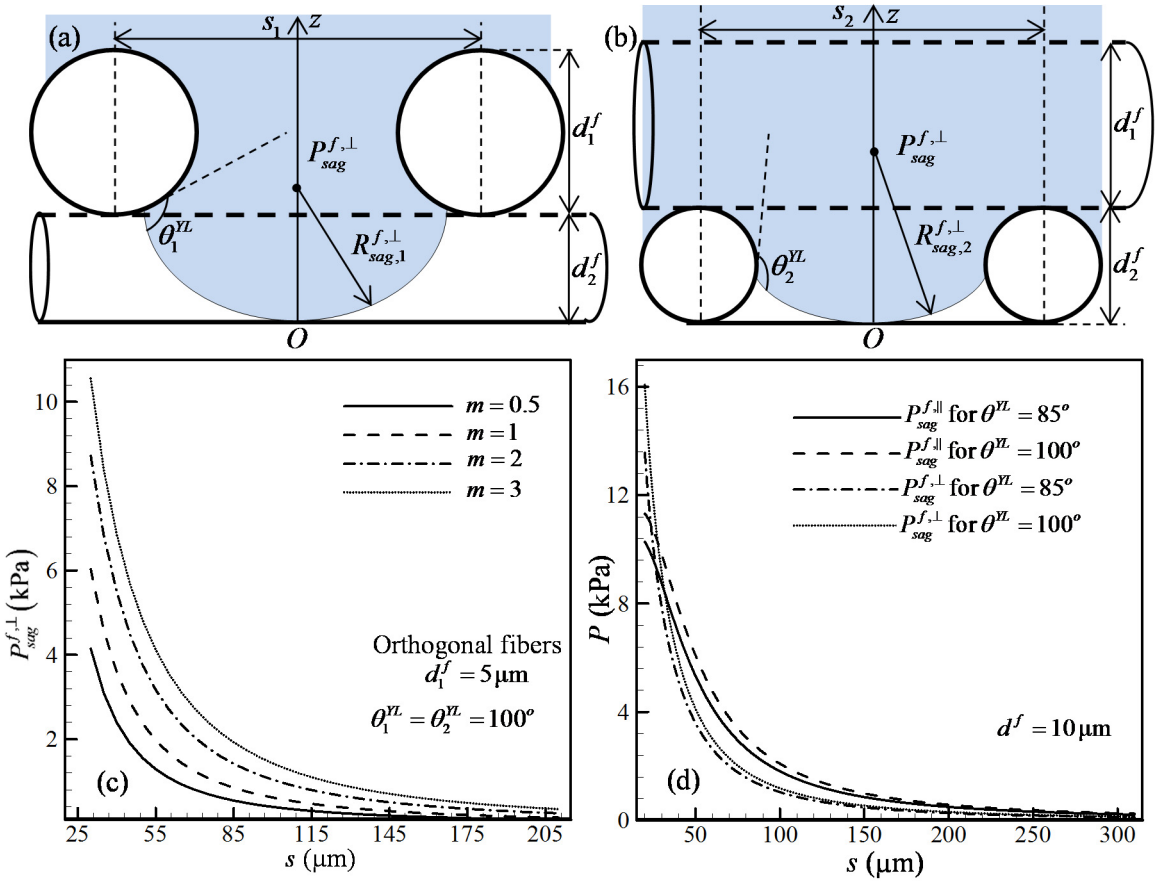

Fig. 4.5: Schematic representation of AWI coming into contact with the substrate for a coating with two orthogonal layers of fibers, with the view along the fibers of the top layer in (a) and along the fibers in the bottom layer in (b). Transition pressure versus fiber spacing in coatings with orthogonal fibers having different fiber diameter in the top and bottom layers in given in (c) for $\theta_1^{YL} = \theta_2^{YL} = 100^o$, $d_1^f = 5\,\mu m$. Transition pressures obtained for orthogonal and parallel-fiber coatings are compared with one another in (d) for $d^f = 10\,\mu m$.

From Eqs. 4.7–4.9, one can obtain,

$$P_{sag}^{f,\perp} = 4\sigma d_1^f \left[\frac{2m + \zeta_1}{s_1^2 + 4d_1^{f\,2}\left(m^2 + m\right)} + \frac{m\zeta_2}{s_2^2}\right] \tag{4.10}$$

For the special case of $d_1^f = d_2^f = d^f$, $s_1 = s_2 = s$, and $\theta_1^{YL} = \theta_2^{YL} = \theta^{YL}$, Eq. 10 simplifies to the following equation.

$$P_{sag}^{f,\perp} = 4\sigma d^f \left(\frac{2+\zeta}{s^2 + 8d^{f\,2}} + \frac{\zeta}{s^2} \right) \tag{4.11}$$

For instance, with $d^f = 10\,\mu\text{m}$, $\theta^{YL} = 85^o$, and $s = 194.1\,\mu\text{m}$, this pressure becomes equal to the Laplace pressure for a droplet with a volume of $0.524\,\mu\text{l}$, and so such a droplet will not stay at the Cassie state on such coatings if $s \geq 194\,\mu\text{m}$. Figure 4.5c shows the variation of $P_{sag}^{f,\perp}$ with fiber spacing for a coating with orthogonal layers of fibers having different diameters. It can be seen that $P_{sag}^{f,\perp}$ decreases with the increasing s, but it increases with the increasing the diameter of the fibers in the bottom layer. Figure 4.5d shows the transition pressures versus fiber spacing for $d^f = 10\,\mu\text{m}$, $\theta^{YL} = 85^o$, $\theta^{YL} = 100^o$ for both coatings with parallel and orthogonal layers of fibers. It can be observed that $P_{sag}^{f,\parallel}$ is always higher than $P_{sag}^{f,\perp}$ when the fiber spacing, fiber diameter, and YLCA are kept constant. This means that a droplet deposited on coating with parallel fibers transitions from the Cassie state at a greater fiber spacing compared to the same droplet sitting on a coating with orthogonal fiber-layers with the same fiber diameter and YLCA.

4.2.3 Cassie-to-Wenzel Transition. Mechanism II: Interface Coalescence

Another cause of departure from the Cassie state is the coalescence of different segments of the AWI inside a coating in such a way that it results in the submersion of a fiber-layer (70). As depicted in Fig. 4.6, if the diameter of the fibers in the bottom layer is large enough, the AWI from the lateral sides of a fiber may come into contact with one another and coalesce into one AWI underneath the fiber. Consider the transition pressure for an AWI over a coating with

parallel fibers as shown in Fig. 4.6a. Each layer of fibers has different fiber diameter and YLCA, but the fiber spacing is the same for both layers. The radius of curvature of the AWI when it is about to meet itself below the first layer should satisfy the following equation.

$$\left(s + d_1^f \cos\theta_1^{YL} - d_2^f \cos\theta_2^{YL}\right) R_{coal}^{f,\parallel} + \left(d_1^f + d_2^f\right)\left(\frac{d_1^{f\,2}}{4} - R_{coal}^{f,\parallel} d_1^f \cos\theta_1^{YL}\right)^{1/2} = \frac{s^2}{4} + \frac{d_1^f}{2}\left(d_1^f + d_2^f\right) \tag{4.12}$$

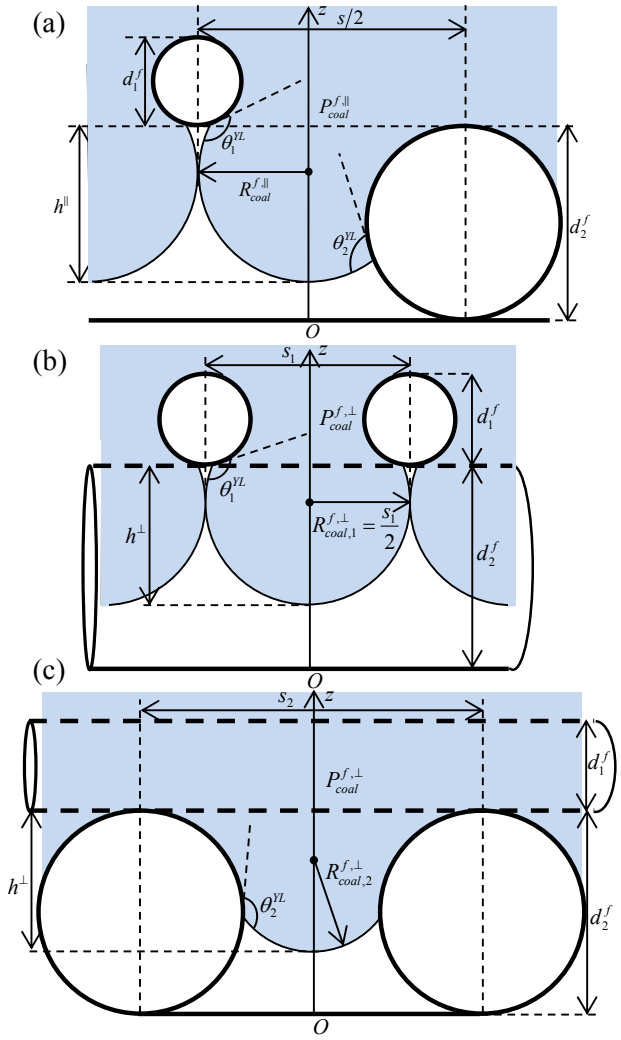

Fig. 4.6: Schematic representation of departure from the Cassie state due to AWI coalescing is given in (a) for coatings with parallel layers of fibers and in (b) and (c) for coatings with orthogonal fibers. Figures (b) and (c) are views along the fibers in the top layer and along the fibers in the bottom layer, respectively.

Departure from the Cassie state takes place through this mechanism for coatings if $d_2^f > h^{\parallel}$. Here, $h^{\parallel}$ is the height of the AWI below the first layer at the moment of coalescence (see Fig. 4.6a), and it can be calculated as,

$$h^{\parallel} = \left(\frac{d_1^{f\,2}}{4} - R_{sag}^{f,\parallel} d_1^f \cos\theta_1^{YL} \right)^{1/2} - \frac{d_1^f}{2} + R_{sag}^{f,\parallel} \tag{4.13}$$

Transition pressure for such coatings $P_{coal}^{f,\parallel}$ can then be calculated using Eq. 4.12 and the Laplace equation,

$$P_{coal}^{f,\parallel} = \frac{\sigma}{R_{coal}^{f,\parallel}} \tag{4.14}$$

Figures 4.6b and 4.6c show the transition through AWI coalescence in coatings comprised of orthogonal fibers. For such coatings, the transition takes place when $d_2^f > h^{\perp}$ where $h^{\perp}$ is the height of the AWI when it is about to meet itself below the first layer (see Fig. 4.6b), i.e.,

$$h^{\perp} = \frac{d_1^f}{2}\left(1 - \frac{2s_1 \cos\theta_1^{YL}}{d_1^f} \right)^{1/2} + \frac{1}{2}\left(s_1 - d_1^f \right) \tag{4.15}$$

The AWI radii of curvature can be calculated to be,

$$R_{coal,1}^{f,\perp} = \frac{s_1}{2} \tag{4.16}$$

$$R_{coal,2}^{f,\perp} = \frac{s_2^2 + 4h^{\perp}\left(h^{\perp} - d_2^f \right)}{4\left(2h^{\perp} - d_2^f - d_2^f \cos\theta_2^{YL} \right)} \tag{4.17}$$

The transition pressure $P_{coal}^{f,\perp}$ can again be obtained using the Laplace equation,

$$P_{coal}^{f,\perp} = 2\sigma\left[\frac{1}{s_1} + \frac{2\left(2h^{\perp} - d_2^f - d_2^f \cos\theta_2^{YL} \right)}{s_2^2 + 4h^{\perp}\left(h^{\perp} - d_2^f \right)} \right] \tag{4.18}$$

Figure 4.7a shows transition pressure for coatings with parallel and orthogonal fibers versus fiber spacing in the bottom layer s_2. It is important to note that s_1 is equal to s_2 for coatings with

parallel fibers, but this is not the case for coatings made of orthogonal layers. For both coatings $d_1^f = 1\,\mu\text{m}$, $d_2^f = 20\,\mu\text{m}$, and $\theta_1^{YL} = \theta_2^{YL} = 100^o$, and $s_1 = 30\,\mu\text{m}$. It can be seen that $P_{coal}^{f,\perp} = P_{sag}^{f,\perp}$ at the s_2 value for which $h^{\perp} = d_2^f$. For smaller fiber spacing, departure from the Cassie state occurs due to AWI coalescence, and the transition pressure can be calculated using Eq. 4.18. Similarly, $P_{coal}^{f,\parallel} = P_{sag}^{f,\parallel}$ at the s_2 value for which $h^{\parallel} = d_2^f$. For smaller spacing, the transition happens due to AWI coalescence, and $P_{coal}^{f,\parallel}$ can be calculated using Eqs. 4.12 and 4.14. Figure 4.7a also shows that for all s_2 values, $P_{FB,\max}^{\parallel}$ is higher than $P_{sag}^{f,\parallel}$ and $P_{coal}^{f,\parallel}$, while $P_{FB,\max}^{\perp}$ remains higher than $P_{sag}^{f,\perp}$ and $P_{coal}^{f,\perp}$. Therefore, for the conditions considered in this chapter, transition from the Cassie state takes place either due to the AWI coming into contact with the substrate or coalescing with itself below the first layer.

Figure 4.7b shows an example of a droplet with a volume of $0.524\,\text{mm}^3$ deposited on a two-layer coating composed of parallel fibers ($d^f = 10\,\mu\text{m}$, $\theta^{YL} = 100^o$, and $s = 170\,\mu\text{m}$). Figure 4.7c shows the same droplet on a similar coating but with orthogonal fibers. Two additional magnified images are added to these figures to better show the AWI between consecutive fibers in a plane cutting through the center of the droplet. The magnified images clearly show that a transition due to sagging mechanism is about to happen upon further increasing the fiber spacing in both cases.

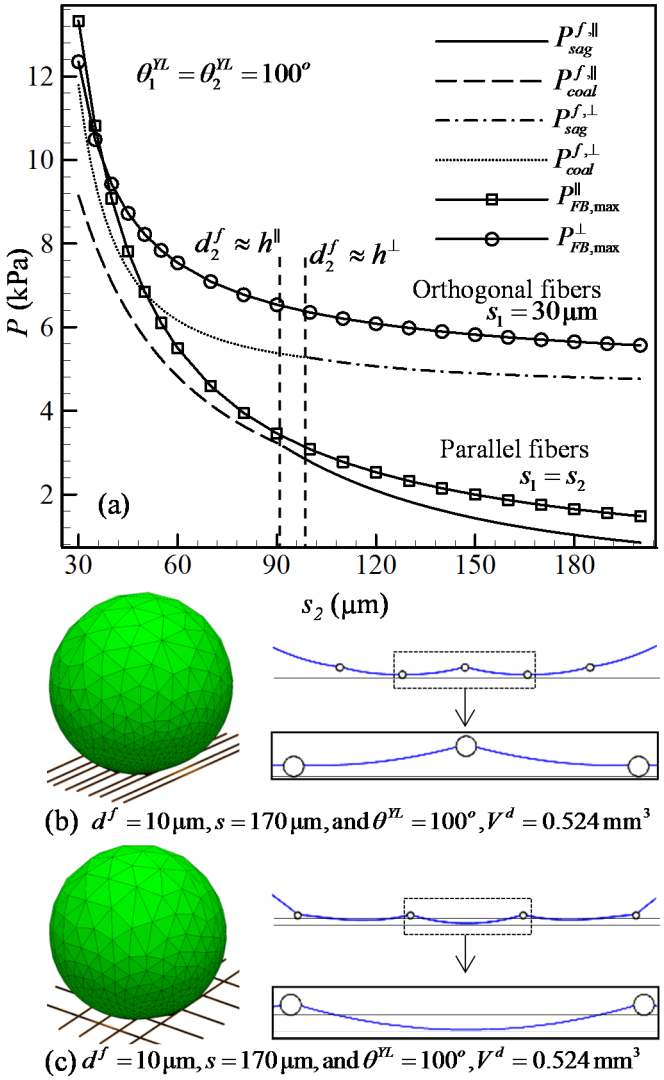

Fig. 4.7: Transition pressure versus s_2 for coatings with orthogonal and parallel layers of fiber is given in (a) for $d_1^f = 1\,\mu m$, $d_2^f = 20\,\mu m$, $\theta_1^{YL} = \theta_2^{YL} = 100^o$, $s_1 = 30\,\mu m$ for coatings with orthogonal fibers, and $s_1 = s_2$ for coatings with parallel fibers. Droplet AWI coming into contact with the substrate on coatings with parallel and orthogonal layers of fiber are shown in (b) and (c), respectively. Here $V^d = 0.524\,\mu l$, $\theta^{YL} = 100^o$, $d^f = 10\,\mu m$, $s = 170\,\mu m$.

The equations derived in this paper can be used to predict if a droplet can achieve the Cassie state on a coating with parallel or orthogonal fibers. For instance, consider a droplet with a volume of $0.524\,mm^3$ (a Laplace pressure of 288 Pa assuming a spherical droplet) on a coating with parallel layers of fibers with $d^f = 10\,\mu m$ and $\theta^{YL} = 100^o$. To determine the fiber spacing at

which departure from the Cassie state takes place, one can assume a transition pressure of $P_{sag}^{f,\parallel}=$ 288 Pa in Eq. 4.5 and then solve this Eqs. 4.5 and 4.6 for s (resulting in $s=284.2\mu m$). Similar calculations can be conducted for the orthogonal counterpart of this coating using in Eq. 4.16 to obtain a fiber spacing of $s=207.1\mu m$. Likewise, one can calculate a critical fiber spacing a given droplet on coatings with different microstructural parameters. Figure 4.8 shows the critical fiber spacing versus fiber diameter for coatings with parallel and orthogonal fibers at a Laplace pressure of 288 Pa and a YLCA of $\theta^{YL}=100^o$. This figure compares the predictions of our analytic calculations with those of SE simulations. It was found that s^c is greater for coatings with parallel fibers compared to their orthogonal counterparts. This is because of the staggered arrangement of fibers in coatings with parallel fibers, where the AWI is supported by a fiber from the top layer and a fiber from the bottom layer (see Fig. 4.7b).

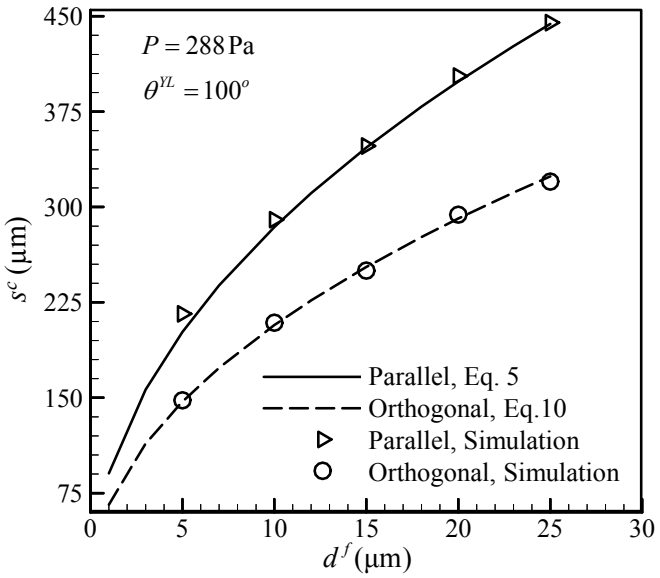

Fig. 4.8: Critical fiber spacing versus fiber diameter for coatings with parallel and orthogonal layers of fiber.

4.3 Modeling Droplet Shape on Fibrous Coatings

The roughness geometry of a coating comprised of parallel fibers is different from that of a coating made up of orthogonal of fibers. As such, one expects to observe different apparent CAs on these coatings. The CAs are expected to depend on fiber diameter, fiber spacing, and YLCA of the fiber material which will be discussed later in this paper. Among different methods reported in the literature (184–187) for modeling droplet shape on a surface, Surface Evolver (SE) code was considered in our study for its modest computational requirements and its availability in the public domain (174). SE computes the equilibrium shape of a droplet by minimizing the free energy of the fiber–droplet system (174). The system's free surface energy can be expressed as:

$$E = \sigma A_{aw} - \sigma \cos\theta^{YL} \iint_{A_{sw}} dA \tag{4.19}$$

The subscripts *a, w,* and *s* denote surrounding air, water, and solid (fibers), respectively. In this equation, A_{aw} and A_{sw} are surface areas of the AWI and solid–water interface. The effects of gravity are not included in our work, as the droplets are assumed to be fairly small. To calculate fibers' energy contribution, the integrand dA in Eq. 4.19 must be derived for each fiber in the simulation domain. For the sake of simplicity, the fibers of the top layer are aligned in the y-direction for all the coatings discussed in this work, i.e.,

$$dA = -\frac{yz}{\sqrt{x^2 + z^2}} dx + \frac{xy}{\sqrt{x^2 + z^2}} dz \tag{4.20}$$

For an energy calculation, the volume of the fibers must be removed from the total volume under the AWI. This is done here by deriving an expression for the fiber's volume element and incorporating that in the SE calculations, i.e.,

$$dV = yzdx \tag{4.21}$$

For coatings with orthogonal layers, the area and volume elements for the fibers in the bottom layer (aligned in the *x*-direction) should also be described mathematically and programed in SE. With the customized area and volume elements, SE can produce the equilibrium shape of a droplet by minimizing the energy of the system while keeping the droplet volume constant. Starting from an arbitrary initial shape (represented with a piecewise linear set of triangular facets), SE can obtain the equilibrium shape of a droplet iteratively. Longitudinal and transverse apparent contact angles were measured from the full size longitudinal and transverse images of the droplet on a computer screen. In the absence of a universally accepted contact angle measurement method for a droplet on a rough surface, we estimated droplet apparent contact angles, at the intersection point of a horizontal baseline (drawn 6 – 8 μm above the coating's top surface) and the droplet profile. Obviously, close attention was paid to the consistency and reproducibility of these readings.

4.4 Results and Discussion

4.4.1 Effects of Fiber Diameter on Apparent Contact Angle

Consider a droplet with a fixed volume deposited on a coating comprised of parallel fibers. Since the apparent CA is not uniform along the droplet contact line, it is expected that the apparent CA observed from a direction parallel to the fibers (longitudinal) will be different from that from a direction perpendicular to the fibers (transverse) as shown in Fig. 4.9a–4.9c.

Figure 4.9d shows how longitudinal and transverse apparent CAs vary with fiber diameter for coatings with parallel fibers having a fiber spacing of $s = 40\,\mu\text{m}$. As expected, apparent CAs are

greater than the YLCA in all cases, as the contact area between the droplet and solid surface is reduced in the Cassie state. More importantly, it can be seen that apparent CAs decrease with increasing fiber diameter. This is because the number of fibers on which the droplet sits increases with increasing the fiber diameter for a given fiber spacing. Therefore, the total wetted area of the coating increases with increasing fiber diameter. It can also be seen in Fig. 4.9d that longitudinal apparent CA is greater than its transverse counterpart (see Figs. 4.9a–4.9c). Figure 4.9e presents the wetted area of the coating under the droplet. It can be seen that wetted area increases with increasing fiber diameter and it is always higher for coatings with smaller YLCA. The inset in Fig. 4.9e shows the fibers wetted length in planes cutting through the middle of the droplet in longitudinal and transvers directions. It can be seen that wetted length in the transverse direction is larger than that in the longitudinal direction especially when the fibers are thin. This seems to correlate well with how apparent CAs in the longitudinal and transvers directions behave in Fig. 4.9d, where a longer wetted length is observed for smaller apparent CAs.

Although we started this subsection by assuming a coating comprised of parallel fibers, it is important to note that the above discussion also applies to coatings with orthogonal fibers as long as the spacing between the fibers is small enough for the droplet to remain in contact with the first layer only (the case shown in Fig. 4.9). It is in fact quite easy to analytically calculate the maximum fiber spacing below which a given droplet never comes into contact with the fibers in the second layer, regardless of the orientation of the fibers in the second layer. One can calculate the pressure at which the AWI deflects as much as one fiber diameter to reach the fibers in the second layer (assuming the point of contact with the fibers in the second layer is at an equal distance from the centers of the fibers in the first layer, i.e., the AWI is symmetric).

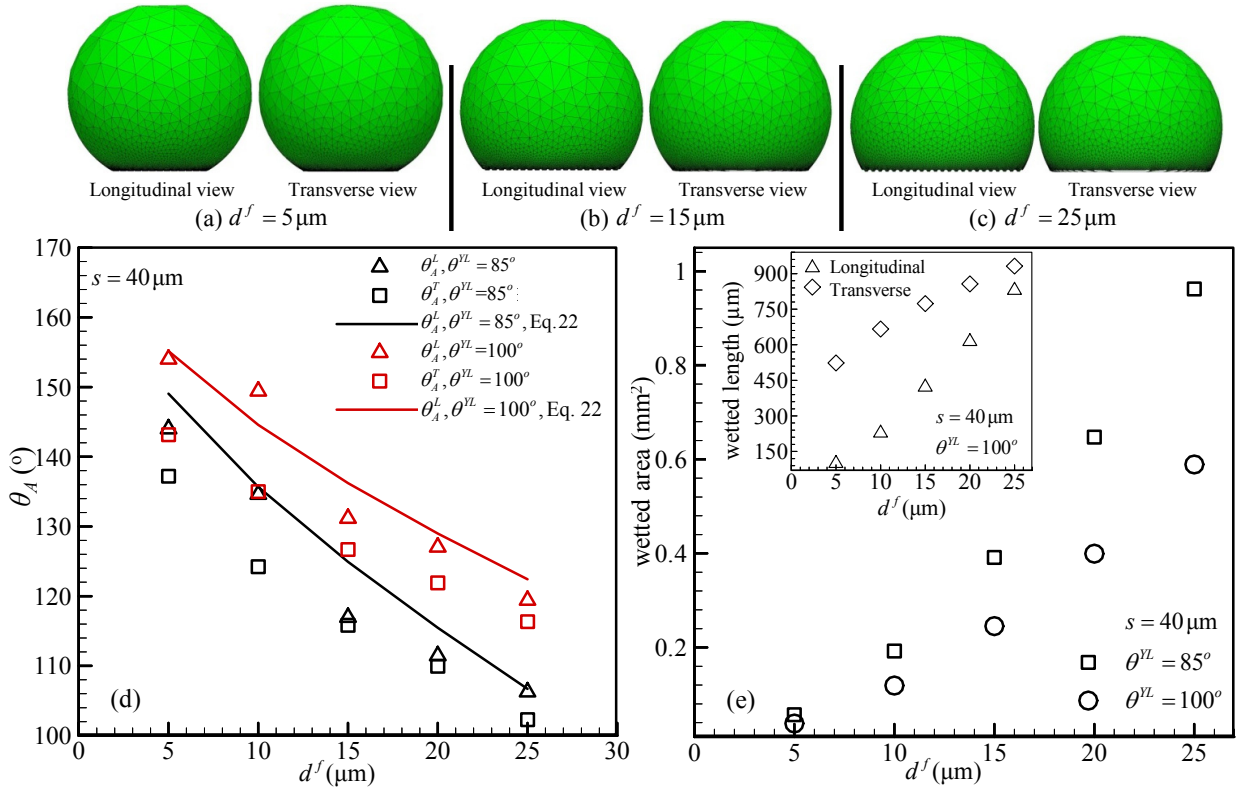

Fig. 4.9: Example simulation results showing a droplet on coatings with parallel fibers from longitudinal and transverse views: (a) $d^f = 5\,\mu m$, (b) $d^f = 15\,\mu m$, and (c) $d^f = 25\,\mu m$ with $\theta^{YL} = 100^o$. Apparent CA and coatings wetted area in the longitudinal and transvers directions are shown for coatings with different fiber diameters with $\theta^{YL} = 85^o$ and $\theta^{YL} = 100^o$ in (d) and (e), respectively. The inset figure in (e) shows the wetted length under the droplet.

Let us consider a droplet deposited on the first layer of fibers in a fibrous coating. Using the Cassie–Baxter equation, for the apparent CA in the longitudinal direction (the Cassie–Baxter equation does not apply to transverse CAs), one can obtain,

$$\cos\theta_A^L = \frac{\alpha d^f}{s}\cos\theta^{YL} + \frac{d^f \sin\alpha}{s} - 1 \tag{4.22}$$

where α is the immersion angle, and it is dependent on droplet pressure, fiber diameter, fiber spacing, and YLCA (70,188).

$$P_{drop} = -\frac{2\sigma\sin\left(\theta^{YL} + \alpha\right)}{\left(s - d^f \sin\alpha\right)} \tag{4.23}$$

Predictions of Eqs. 4.22 and 4.23 are added to Fig. 4.9d, and show good agreement with the results of our numerical simulations. Note that the effects of fiber diameter on droplet apparent CA for when the droplet is in contact with both fiber-layers (i.e., for large fiber spacing values) is not discussed in this subsection, for the sake of brevity.

It is interesting to note that the longitudinal CA value of $\theta_A^L = 144^o$ shown in Fig. 4.9d for a coating with a fiber diameter of 5 μm is within 5% of its experimental counterpart given in Fig. 4.1b (i.e., $\theta_A^L = 152^o$) for a SAF 0.23 which corresponds to the SAF the virtual orthogonal coating used in Fig. 4.9d.

4.4.2 Effects of Fiber Spacing on Apparent Contact Angle

The effects of fiber spacing on θ_A^L and θ_A^T in coatings with an arbitrary fiber diameter of 10 μm is studied in this subsection. As mentioned earlier in subsection 4.4.1, increasing the fiber spacing can result in the droplet coming into contact with the fibers in the bottom layer. The wetting behavior of a droplet becomes quite different when it is in contact with more than one layer of fibers, and that behavior is different depending on whether the second layer is perpendicular or parallel to the fibers in the top layer (see Figs. 4.10a–4.10i). For the set of parameters considered in the present study, the critical fiber spacing is found to be s_t = 95.54 μm for coatings with an YLCA of $\theta^{YL} = 85^o$ and, s_t =108.3 μm for those with a YLCA of $\theta^{YL} = 100^o$. It can be seen in Figs. 4.10j–4.10k that both the longitudinal and transverse CAs increase almost monotonically with s for $s < s_t$ (the number of fibers on which the droplet sits decreases and so the coating's wetted area decreases). Predictions of Eq. 4.22 (applicable to longitudinal direction only) are also added to Figs. 4.10j and 4.10k for $s < s_t$, and good general agreement with the

results of our simulations can be observed. For $s \geq s_t$, the droplet sits on two layers of fibers, and the variation in the longitudinal and transverse CAs with s depends strongly on the orientation of the fibers in the second layer (see Figs. 4.10a–4.10i). The longitudinal CA seems to periodically decrease and increase in different ranges of fiber spacing (e.g., from about 100 to 200 μm for the case of coatings with parallel fibers and an YLCA of $\theta^{YL} = 85^o$) for both the orthogonal and parallel-fiber coatings. This behavior can be explained by considering the number of fibers in contact with the droplet for each fiber spacing. Note that immersion angle increases with increasing the spacing between the fibers, when the number of fibers in contact with the droplet is fixed. This in turn increases the coating's wetted line in the longitudinal direction, and consequently decreases the longitudinal CA. Further increase in the fiber spacing forces the droplet to detach from some of the fibers farther away from the center. This decreases the coating's wetted line in the longitudinal direction and increases the longitudinal CA. Further increase in the fiber spacing repeats the above effects, leading to the reported fluctuating longitudinal CAs. Note that despite these fluctuations, the net effect of increasing the fiber spacing is an overall (yet marginal) increase in the longitudinal CA. Similar variations in apparent CA was has also been reported for droplets deposited on a chemically heterogeneous substrate (63, 189). The data given in Figs. 4.10j and 4.10k seem to indicate that CA fluctuations become less significant when droplet diameter (about 1 mm here) is more one order of magnitude larger than 1 fiber spacing.

Transverse CA, unlike its longitudinal counterpart, seems to be relatively independent of fiber spacing (transverse wetted length varies insignificantly with fiber spacing as shown in Figs. 4.10a–4.10i). It is interesting to note a sudden drop in transvers CAs given in Figs. 4.10j and

4.10k for coatings with parallel fibers. This is accompanied with a sudden increase in the wetted length of the coatings in the transvers direction at the moment a droplet penetrates deep into the coating to reach the second layer of fibers (not shown with numbers for the sake of brevity but can be seen in Figs. 4.10c–4.10i).

Overall, it can be seen that longitudinal CAs are greater than their transverse counterparts for both the orthogonal and parallel-fiber coatings. We observed for $s \geq s_t$ that, CA on a coating with orthogonal fibers is higher than that of a similar coating with parallel fibers. However, a droplet deposited on the orthogonal coating is more susceptible to fiber spacing, and it may depart from the Cassie state earlier (as the droplet evaporates, for instance) than the same droplet on the coating with parallel fibers. Our analytical equations for a droplet with a volume $0.524\,\mu\text{l}$ (see Secs. 4.2.2 and 4.2.3) indicated a departure from the Cassie state at a spacing of $s = 194.1$ μm, for $\theta^{YL} = 85^o$, and $s = 207.1$ μm, for $\theta^{YL} = 100^o$, on a coating with orthogonal fibers, and at $s =$ 264 μm, for $\theta^{YL} = 85^o$, and $s = 284.2$ μm, for $\theta^{YL} = 100^o$ on the same coating but with parallel fibers.

Maintaining the Cassie state on a fibrous coating depends on droplet volume, fiber diameter, fiber spacing, and YLCA of the fiber material. One can define the smallest YLCA for which an apparent contact angle greater than 90^o is attainable as the minimum YLCA $\theta_{90}^{YL\,\min}$ for a fibrous coating to be hydrophobic. To do so, one needs to first find the minimum YLCAs required for a droplet to remain at the Cassie state $\theta_{Cas}^{YL\,\min}$, and then among them, find those that correspond to an apparent contact angle greater than 90^o (i.e., $\theta_{90}^{YL\,\min}$).

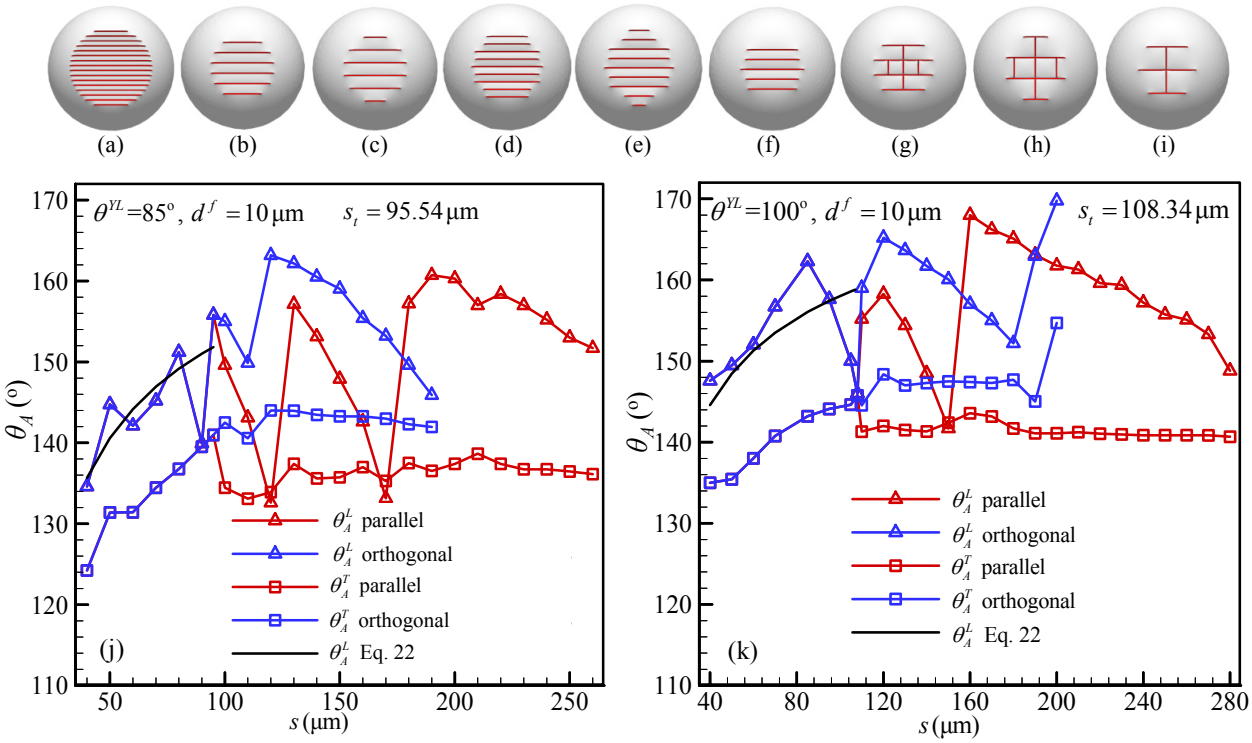

Fig. 4.10: Bottom views of a droplet with a volume of 0.524 μl deposited on coatings with parallel or orthogonal layers of fiber with different fiber spacing having $\theta^{YL} = 100^o$ and $d^f = 10\,\mu m$. For (a) through (c) and the droplet is in contact with the top layer only ($s = 40\,\mu m$, $s = 85\,\mu m$, and $s = 105\,\mu m$ in (a), (b), and (c), respectively). For (d) through (f) the droplet is in contact with both layers of a coating with parallel fibers ($s = 120\,\mu m$, $s = 150\,\mu m$, and $s = 160\,\mu m$ in (d), (e), and (f), respectively). For (g) through (i) the droplet is in contact with both layers of a coating with orthogonal fibers ($s = 120\,\mu m$, $s = 170\,\mu m$, and $s = 190\,\mu m$ in (g), (h), and (i), respectively). Longitudinal and transvers CAs versus fiber spacing for $\theta^{YL} = 85^o$ and $\theta^{YL} = 100^o$ are given in (j) and (k), respectively.

Let us consider the simple case of a droplet on a coating with a single layer of parallel fibers. It can be shown that, departure from the Cassie state (due to interface sagging) happens only when the following equation is satisfied,

$$\cos\theta_{Cas}^{YL\,\min} = 1 - \frac{P_{drop} s^2}{4\sigma d^f} \tag{4.24}$$

It can clearly be seen from Eq. 4.24, that $\cos\theta_{Cas}^{YL\,\min}$ is proportional to s^2 but inversely proportional to d^f (i.e., stronger dependence on fiber spacing). In using this equation, note that $s > d^f$. This is in conceptual agreement with the work of (51) and (190) who showed surfaces

with re-entrant geometry may exhibit hydrophobic behavior even with YLCAs less than 90 degrees. Note however that, if the sparing between the fibers becomes so small that the fibers come into contact with one another, the coating geometry will no longer provide a re-entrant structure, and no Cassie droplet should be expected for $\theta^{YL} < 90^o$.

Equations 4.22 and 4.23 can be used to calculate $\theta_{90}^{YL\min}$ by assuming $\theta_A^L = 90^o$, i.e.,

$$\cos\theta_{90}^{YL\min} = \frac{s}{\alpha d^f} - \frac{\sin\alpha}{\alpha} \tag{4.25}$$

and

$$P_{drop} = -\frac{2\sigma\sin\left(\theta_{90}^{YL\min} + \alpha\right)}{\left(s - d^f\sin\alpha\right)} \tag{4.26}$$

For instance, for a droplet with a volume of $0.524\,\mu l$ on a coating comprised of a single layer of fibers with $d^f = 5\,\mu m$ and $s = 5.5\,\mu m$, one obtains $\theta_{Cas}^{YL\min} = 6.31^o$ and $\theta_{90}^{YL\min} = 86.4^o$. This means that such a coating can exhibit hydrophobic behavior for $\theta^{YL} > 86.4^o$. To confirm that the droplet is at the Cassie state, one should check if $\theta_{90}^{YL\min} > \theta_{Cas}^{YL\min}$.

4.5 Conclusions

The Cassie state of a droplet deposited on a coating with orthogonal fibers is studied in this paper. For comparison, similar coatings comprised of parallel fibers are also studied, as a droplet may only interact with a layer of parallel fibers when the fiber spacing is smaller than some critical spacing value. Easy-to-use analytical expressions are derived to predict the condition in which a droplet may depart from the non-wetting Cassie state by partially or completely wetting the coating below it. The numerical simulations conducted

in this work indicate that apparent contact angles of a droplet can be increased by decreasing the diameter of the fibers in the coating for a given fiber spacing (fiber count per unit length). Similarly, it was shown that increasing the fiber spacing, up to a critical value, can also help to increase the contact angles on a coating with a given fiber diameter. However, droplet contact angle can exhibit considerable fluctuations with varying fiber spacing. Considerable differences was observed between droplet contact angles on orthogonally layered and parallel-fiber coatings, i.e., a droplet may achieve higher contact angles on a coating with orthogonal fibers.

Chapter 5. Role of Particles Spatial Distribution in Drag Reduction Performance of Superhydrophobic Granular Coatings

5.1 Introduction

Superhydrophobic (SHP) coatings, coatings that bring about roughness and hydrophobicity, have been reported to reduce the friction drag between a body of water and a surface (55,56,80,84,191-194). This effect is attributed to the ability of a rough hydrophobic surface to entrap air bubbles in its pores and thereby reduce the contact between the solid surface and the water. The contact area and the friction between the water body and the SHP surface can be manipulated by controlling the volume and the pressure of the air bubbles entrapped in the pores of the SHP surface in the submerged condition (195) as well as for the case of a droplet deposited on a SHP surface (196,197). SHP surfaces can potentially be applied to the hull of a boat or the inner walls of a pipe to reduce friction (82,198,199).

SHP surfaces are often produced by microfabricating small features on a smooth surface and then applying a hydrophobic coating to the roughened surface (84,192). A more cost-effective alternative is to coat the smooth surface with a porous hydrophobic material, e.g., Polystyrene fibers or aerogel particles among many others (58,86,87,89,200). Depending on coating geometry and flow parameters, the Wenzel state (fully-wetted), the Cassie state (fully-dry), or a series of transition states in between the two extreme states may prevail over a submerged SHP surface (78,45,51,52,195). Unfortunately, even a slight departure from the Cassie state may result in a rapid increase in the surface wetted area (solid area in contact with water), and a consequential diminishment of the drag reduction effect, as will be discussed later in this paper (201).

Predicting the shape and position of the air–water interface over a SHP surface comprised of round objects (e.g., spherical objects) is not a trivial task. This is because the air–water interface does not become pinned to the round entrance of the pores, and so its shape and position can easily vary in response to variations in the instantaneous pressure over the surface (87,202). This in turn makes the drag-reduction benefit of the surface highly pressure dependent. In a previous study, we developed a modeling method to predict the shape and position of the air–water interface in order to obtain the wetted area of a granular SHP coating as a function of pressure (90,91). While the drag force caused by a SHP surface is related to its wetted area, the nature of this relationship is not very clear, as will be discussed with more details in the next section. Therefore, the current study is devised to calculate the drag reduction advantage of a granular SHP coating in terms of its microstructural parameters. For the sake of simplicity, our study is limited to the case of granular coatings made of spherical particles with identical size but ordered or random spatial distributions.

The remainder of this chapter is organized as follows. In Section 5.2, we present a brief overview on the drag reduction benefits of SHP granular coatings. Section 5.3 presents our approach to model the shape and position of the air–water interface (AWI) over a SHP granular coating. Our drag reduction calculation method is described in Section 5.4 along with a validation study in Section 5.5. Results and discussion are given in Section 5.6 followed by our conclusions in Section 5.7.

5.2 Drag Reduction from Superhydrophobic Granular Coatings

As mentioned earlier, a cost-effective approach to produce a SHP surface is to coat a substrate with a hydrophobic material that can add roughness to the surface. Figure 5.1a shows an example of such a surface made of pulverized aerogel particles. When the void between the particles is completely filled with air, the surface is generally considered to be at the Cassie state (fully dry).

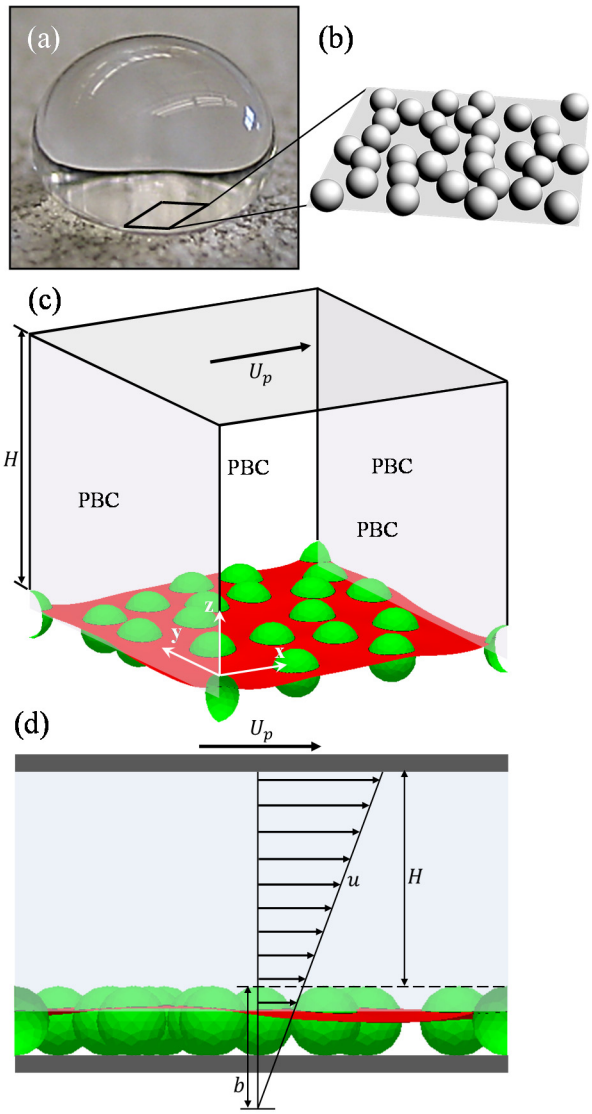

Fig. 5.1: (a) Droplet deposited on a granular surface made of pulverized aerogel particles (b) schematic representation of an idealized granular coating deposited on a flat surface (c) Schematic representation of the computational domain considered for calculating the flow over a superhydrophobic granular coating in a Couette configuration. (d) Schematic diagram describing the slip length concept for flow over granular SHP coating.

However, when the pressure over the AWI is elevated (either because droplet's Laplace pressure is too high or because the surface is submerged), water may penetrate into the void space between the particles to partially wet the surface (i.e., causing the surface to depart from the Cassie state). Figure 5.1b shows a schematic of an idealized granular coating deposited on a flat surface (a layer of spherical particles with identical diameters). As discussed previously (78,87,90,91,202), the balance between the forces acting on the AWI (shown with red color in Figures 5.1c and 5.1d), will eventually determine the location of the AWI and the wetting state of the surface. Knowing the location of air–water–solid contact-line (referred to here as three-phase contact-line or contact-line for brevity) from the balance of forces, and the surface geometry, one can predict the wetted area of the surface (green area above the AWI in Figures 5.1c and 5.1d). A body of water moving over a SHP granular coating experiences frictional (no-slip) contact with the coating's wetted area, but slippery (shear-free) contact along the AWI (see Figures 5.1c and 5.1d). Overall, one can expect a reduction in the total surface friction due to the reduction in the total wetted area of the surface in comparison to the uncoated flat surface. The decrease in the friction drag over a SHP surface is often characterized using slip length b which is a geometric interpretation based on the average distance underneath the top of the particle coating at which the velocity extrapolated to zero (see Figure 5.1d).

While the drag force caused by a SHP surface is related to its wetted area, the nature of this relationship is not very clear. As shown in (92,93) for instance, the air bubble entrapped in the sharp-edged pores of a SHP surface may protrude into the flow region (if the pressure outside the pores is less than that inside the pores) to increase the drag force

without increasing the wetted area of the surface (wetted area remains the same due to AWI pinning). As will be seen later in this paper for unpinned AWIs (round pores), bubble protrusion into the flow domain does not severely affect the surface drag reduction performance as it comes with a decrease in the surface wetted area. However, the drag reduction benefits of a surface comprised of round-edged pores (or particles, for instance) is generally lower than those of sharp-edged pores (e.g., a surface made of vertical mirco-posts) with identical solid area fractions. This is because of the aforementioned need for the AWI to move into the pore space to a depth that allows it to conform to the Young–Laplace contact angle (YLCA). This will obviously increase the wetted area of the surface even in the absence of a hydrostatic pressure over the surface. In fact, friction on a SHP granular surface depends on three main parameters, area and the 3-D shape of the wetted solid surface, area and the 3-D shape of the AWI (either concave or convex), and the size distribution of the individual wetted areas (or individual shear-free areas). To further study these parameters in this paper, we produce virtual SHP granular coatings with random or ordered particle arrangements and study their drag reduction performance in a Couette flow geometry as shown in Figures 5.1c and 5.1d. The calculation details are given in Section 5.3 and 5.4.

5.3 Modeling Air-Water Interface Over Superhydrophobic Granular Coatings

As mentioned earlier, we expect water drag force on a SHP granular coating to be dependent on the wetted area, shear-free area, and relative size of the individual wetted areas. While our main objective here is to study coatings having particles with random spatial distributions (for obvious practical reasons), we also consider coatings with ordered particle distributions in square and staggered arrangements for comparison.

The Surface Evolver (SE) finite element code (174) is used in this study to predict the 3-D shape and the location of the three-phase (air–water–solid) contact-line over the particles. SE computes the equilibrium shape of the AWI by minimizing the free energy of the entire system given as

$$E = \sigma A_{aw} - \sigma \cos\theta^{YL} \iint_{A_{sw}} dA - P_h V_a \tag{5.1}$$

Here, σ is surface tension of water, θ^{YL} is Young-Laplace contact angle (YLCA) of the granular particles, A_{aw} is area of the AWI, A_{sw} is area of the wetted solid, P_h is the prescribed pressure on the AWI and V_a is volume of the air under AWI. We start the SE simulation with an arbitrary initial shape of the AWI represented with a piecewise linear set of triangular facets. The shape of the AWI is updated in each iteration. SE computes the energy of the AWI by computing the area of the AWI represented with a piecewise linear set of triangular facets and multiplying that area by σ. SE also needs to compute A_{sw} to calculate the energy contribution of the particles. The solid-water interface is constrained to lie on the surface of the spherical particles. In SE, it is more convenient to use a path integral for each solid-water interface or particle-water interface area to compute their energy contribution to the total energy E. Using the SE manual (174) we derived the path integral to account for the particle-water interface area:

$$\iint_{A_{sw}} dA = \oint_{\partial A_{sw}} \left[\frac{zr}{x^2 + y^2} \left(-y\hat{i} + x\hat{j} \right) \right] . d\hat{l} \tag{5.2}$$

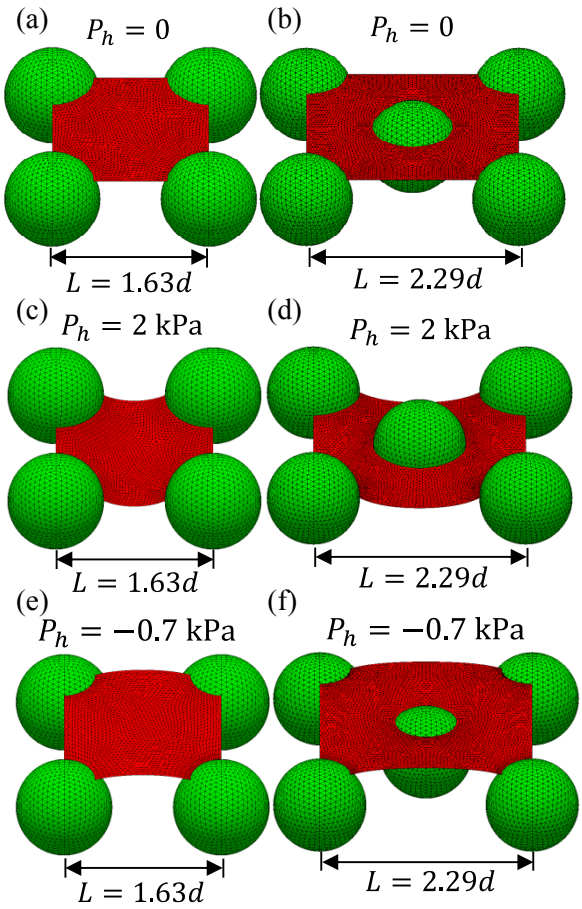

Fig. 5.2: Air–water interface over a unit cell of coatings with square and staggered particle arrangements under arbitrary positive, zero, and suction pressures. For all cases $d = 30\,\mu\text{m}, \theta^{YL} = 120^o$ and SVF=0.2 .

SE needs to calculate the total volume of air under the AWI i.e. V_a . In order to do that SE needs to subtract the part of the volume under the AWI occupied by the particles from total volume under the AWI. The volume under the AWI is computed by SE by computing the volume of the vertical prisms between each facet of the AWI and $z = 0$ plane. Since we don't represent the particle-air interface by facets in the simulation, we had to use a path integral for each particle to find the volume under the AWI occupied by the particle. Using the SE manual (174) we derived the path integral:

$$V_s = \oint_{\partial A_{sw}} \left[\frac{z^3}{3\left(x^2 + y^2\right)} \left(-y\hat{i} + x\hat{j}\right) \right] . d\hat{l} \tag{5.3}$$

With the above expressions of the path integrals for the particle-water interface area and volume V_s, SE can then be used to produce the equilibrium shape of the AWI that minimizes the energy of the system at a given pressure P_h iteratively. Figure 5.2 shows examples of such calculations conducted for coatings with square and staggered arrangements of particles under zero, positive and negative pressures (only a unit cell is shown due to periodicity of the geometry). Figure 5.2 shows that the AWI penetrates deeper into the coating with the hydrostatic pressure P_h increasing from a suction pressure (negative pressure) to a positive pressure leading to an increase in the wetted area of the surface.

It is important to mention here that the hydrostatic pressure at which the three-phase contact-line leaves the pore entrance (pore's top surface) is generally referred to as the critical hydrostatic pressure of the surface (52,87,90,202). This definition was originally intended for pores with a sharp-edged entrance where the interface pins itself to the edges of the pore. The definition of critical hydrostatic pressure is not as clear when it comes to pores with a round entrance (e.g., void between particles). This is because the unpinned three-phase contact-line in this case needs to move down into the pores to conform to a shape that maintains an angle with the wall equal to the YLCA. Therefore, for the lack of a better alternative, critical hydrostatic pressure for a pore formed between spherical particles (or cylindrical objects) is taken to be the hydrostatic pressure at which the AWI moves deep into the pore to reach a critical immersion angle of $\alpha = \alpha^{cr}$ for which the capillary pressure P_{cap} is maximum (see (78,87,90,201-203) for more detailed information).

Note that pressure in our SE simulations is meant to represent the difference between the pressure above the AWI in water and the pressure in the air entrapped in the void between the particles, regardless of the source or cause of the pressure. This pressure can be present due to just a hydrostatic pressure or a combination of hydrostatic and hydrodynamic pressures. We have assumed that the flow is slow and steady (no time-dependent pressure fluctuations or turbulent effects), but a geometry-induced effect can cause the pressure to vary from one case to another or even become negative (e.g., flow over a macroscopically-large curved surface like a hydrofoil or whenever in a Venturi-like effect can be observed).

5.4 Slip-Length Calculation

To simplify an otherwise overwhelmingly difficult problem, we assume the drag-reduction performance of a SHP surface to be time-independent for a given hydrodynamic condition. We then solve the Navier–Stokes equations for the flow over the surface comprised of a series of frictional solid areas (wetted areas) and shear-free AWI areas. The 3-D shape and the location of these areas are obtained from the simulations discussed earlier in Section 5.3. The continuity and momentum equations for a steady incompressible Couette flow of water over our SHP granular coatings are solved numerically using the finite volume method implemented in ANSYS CFD code,

$$\frac{\partial u_i}{\partial x_i} = 0 \tag{5.4}$$

$$\rho u_j \frac{\partial u_i}{\partial x_j} = -\frac{\partial P}{\partial x_i} + \mu \frac{\partial^2 u_i}{\partial x_j \partial x_j} \tag{5.5}$$

where u_i is the velocity, x_i is the Cartesian coordinate directions, ρ is water density, P is pressure, and μ is water viscosity. We used the no-slip boundary condition for the wetted area, but considered the symmetry boundary condition for the AWI to resemble a shear-free boundary. As was shown in Figure 5.1c, periodic boundary condition (PBC) is considered in the streamwise and lateral directions. The Reynolds number Re, defined based on the Couette gap distance H and upper wall velocity U_p, was varied from 0.01 to 18. Following Choi and Kim (192) and Srinivasan et al. (204), we define effective slip length as

$$b_u = (\frac{\tau_{ns}}{\tau_s} - 1)H \tag{5.6}$$

where τ_s and τ_{ns} are the shear stress at the upper plate in a Couette flow with a SHP bottom plate and stationary bottom plate without a SHP coating, respectively. Treating a woven screen as a planar surface, an approximate but yet easy-to-use effective slip length expression (Equation 5.7) was provided by Davis and Lauga (205) and Srinivasan et al. (204) and is used here for comparison.

$$b_{app} = \frac{L}{3\pi} \ln \frac{2\left(1+\sqrt{1-A_w}\right)}{\pi A_w} \tag{5.7}$$

Here, A_w is wetted area fraction, and it is calculated based on the actual solid–liquid interface area obtained from SE simulations in our work. In this equation L is center-to-center spacing between two particles in an aligned granular coating. It should be mentioned that, our simulations are set up on a one-way-coupling basis in which the AWI can affect the flow field but not the other way around. In other words, it is assumed that hydrodynamic stresses are too small to deform the AWI. This is justified based on the fact that the capillary number $Ca = \mu \dot{\gamma} d / 2\sigma$ for our coatings is much smaller than one ($\dot{\gamma}$ is a characteristic shear rate, e.g.,

U_p / H) (93, 206, 207). For instance, for an upper plate velocity of $U_p = 0.1$ m/s and a gap distance of $H = 179$ μm, we can obtain $\dot{\gamma} \cong U_p / H = 558\ \text{s}^{-1}$ and so $Ca \cong 5 \times 10^{-4} << 1$ for a coating comprised of particles with a diameter of $d = 30$ μm (with water having viscosity and surface tension coefficients of $\mu = 10^{-3}$ Pa.s and $\sigma = 72 \times 10^{-3}$ N/m, respectively).

5.5 Validation

In this section, we examine the accuracy of the computational data produced in our study for both the AWI modeling and slip length calculation. As mentioned earlier, the equilibrium shape of the AWI was produced using SE. To validate our SE simulations, we compare the wetted area fraction obtained from our simulations with those obtained using a force balance (FB) equation (78, 87, 202). For this comparison, we considered a SHP granular coating having a particle diameter of $d = 30\,\mu\text{m}$, a YLCA of $\theta^{YL} = 120^o$, and a solid volume fraction (SVF) of 0.1 on a square particle arrangement. Balance of forces acting on an AWI between four particles in a square packing at equilibrium requires the hydrostatic pressure in the *z*-direction to be countered by the capillary forces generated by the particles, i.e.,

$$P_h\left(L^2 - \frac{\pi d^2 \sin^2\alpha}{4}\right) = \pi\sigma d \sin\alpha \cos\left(\frac{3\pi}{2} - \theta^{YL} - \alpha\right) \tag{5.8}$$

For a given hydrostatic pressure P_h, we can obtain immersion angle α by solving Equation 5.8 (87, 202). The wetted area fraction can then be computed as,

$$A_w = \frac{\pi d^2}{2L^2}\left(1 - \cos\alpha\right) \tag{5.9}$$

It can be seen in Figure 5.3a that our SE simulation results are in very good agreement with those from FB equations. It is worth mentioning that we use SVF to characterize the

density (or crowdedness) of our coatings as it represents the mass of the particles placed on the surface (one layer thick coatings), and it is a parameter that can be used in manufacturing. This is somewhat in contrast to some studies in the literature where solid area fraction (SAF) or gas area fraction (GAF) has been used in the discussing slip length over a SHP surface. It is important to note that SAF (or GAF) is more suitable for SHP surfaces with flat-top asperities (e.g., surfaces comprised of sharp-edged micro-posts) as in such cases SAF is practically the same as the wetted area, and it is a constant value independent of pressure (due to AWI pinning). In our work on the other hand, the AWI is not pinned and so it is allowed to move up or down in response to pressure. This makes the wetted area pressure dependent. To ensure that our slip-length calculations are not affected by the choice of grid size, we repeated one of our simulations using different mesh densities, and monitored how our slip length predictions were affected. More specifically, a SHP coating comprised of particles with a diameter of $d = 30\,\mu\text{m}$, a YLCA of $\theta^{YL} = 120^{o}$, and square packing fraction of 0.1 is considered in Couette flow at a hydrostatic pressure of $P_h = 200\,\text{Pa}$. An upper plate velocity of $U_p = 0.1\,\text{m/s}$ and a gap distance of $H = 179\,\mu\text{m}$ were considered for the simulations. The computational domain was meshed using a tetrahedral mesh refined near the AWI and the particles. The effective slip length was calculated using Equation 5.6 for different mesh size δ on the three phase contact line. As can be seen in Figure 5.3b, increasing the mesh density by a factor of 4 only impacted the slip length by a factor of 0.96, and no measureable mesh dependence was overserved for $d/\delta \geq 34$. A mesh density of $d/\delta \geq 34$ has then been considered for all the simulations reported in this chapter (see (208) for more information about slip length calculation). To investigate how particles' random spatial positons in a

coating can impact its effective slip length, four statistically identical coatings having different particle distributions are simulated and their drag reduction performance is shown in Figure 5.3c. It can be seen that effective slip length values average to about 19.3 μm with a standard deviation of about 1 μm (a wetted area fraction of $A_w \approx 0.19$ was observed for all four coatings). It is also worth mentioning that no dependence on the upper plate velocity was observed for the slip length values reported in this paper (for the range tested, i.e., 0.005 $< U_p <$ 0.1 m/s), which is in agreement with the work of Cottin-Bizonne et al. (209).

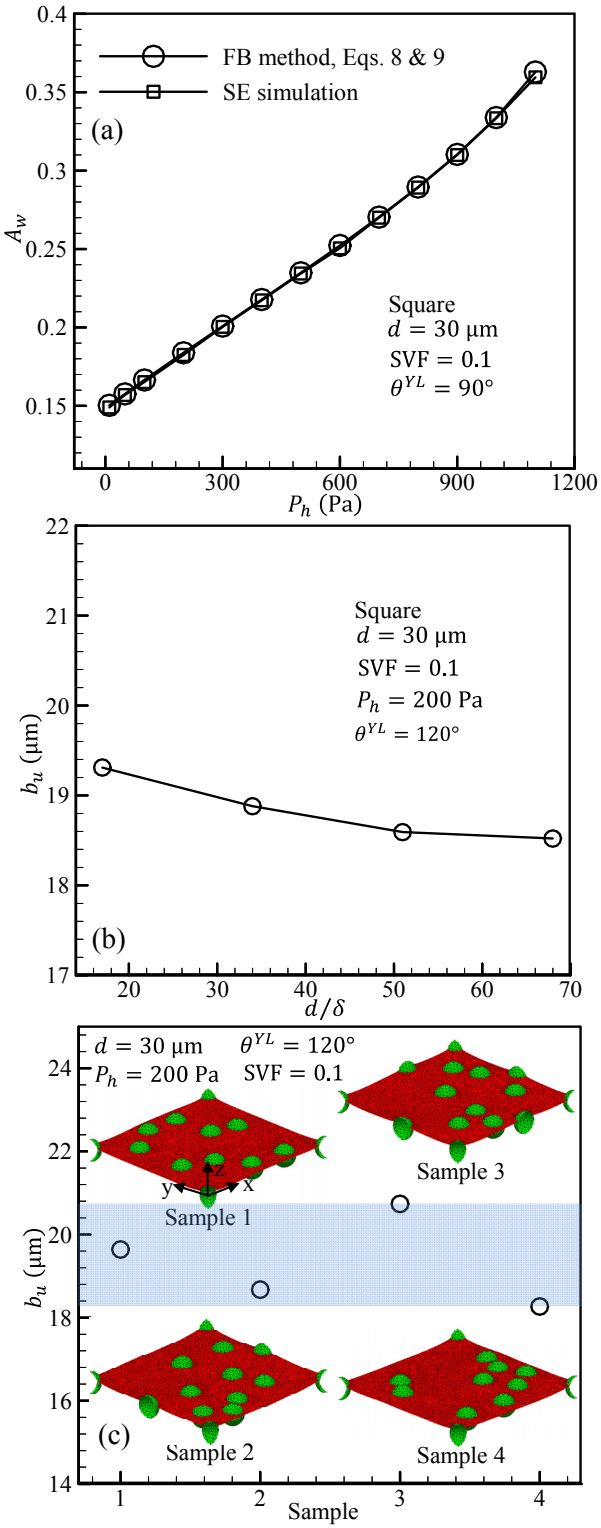

Fig. 5.3: (a) Comparison between wetted area fractions obtained from our SE simulations and from analytical force balance calculations for a granular coating with square particle packing. (b) Effects of mesh density on effective slip length for a granular coating with square particle packing. (c) Effects of different particle arrangements on slip length in granular coatings with a constant SVF but different random distribution of particles.

5.6 Results and Discussion

5.6.1 Effects of hydrostatic pressure on slip length

As discussed in previous works (90,91), a coating's wetted area may vary significantly with hydrostatic pressure (non-dimensionalized using a length scale characterizing the inter-particle spacing, i.e., unit cell length L, and surface tension). As can be seen in Figure 5.4a, the wetted area fraction increases rapidly with increasing hydrostatic pressure from a negative suction pressure (e.g., caused by the Venturi effect) to a positive compression pressure (e.g., flow in a pressurized channel). This is because the AWI moves deeper into the coatings with increasing pressure but tends to move upward to protrude into the flow domain with deceasing pressure as shown earlier in Figure 5.2. Reduction in the wetted area fraction due to negative suction pressure for a hierarchical SHP surface in submerged conditions were earlier reported by Verho et al. (195). It can also be seen in Figure 5.4a that spatial distribution of the particles (other parameters held constant), does not significantly affect the relationship between the wetted area and normalized hydrostatic pressure. Figure 5.4b shows normalized effective slip length versus normalized pressure for the same coatings. It can again be seen that slip length is not very sensitive to spatial distribution of the particles in a coating, and it decreases with increasing wetted areas (e.g., caused by pressure). Interestingly, the increase in slip length at negative pressures is much more significant than its decrease in positive pressure. Note that, while the drag reduction behaviors of these three types of coatings are similar, coatings with ordered (square or staggered) arrangements have high critical hydrostatic pressures, and are therefore less prone to failure (90, 91). We obtained critical hydrostatic pressures of about 1125 Pa and 930 Pa for the ordered (identical for square and staggered) and random coatings simulated in Figure 5.4.

Likewise, the critical suction pressures for ordered and random coatings were found to be about 390 Pa and 370 Pa, respectively.

For comparison, effective slip length is also calculated using Equation 5.7 for coatings with square particle packing and the predictions are added to Figure 5.4b. Note that Equation 5.7 provides the same slip length values for coatings with staggered or random particle arrangements as they all have the same wetted area fractions. It can be seen that the approximate expression given in Equation 5.7 under-predicts the slip length values, and the mismatch increases at lower pressures. We believe this is because Equation 5.7 was originally derived for planar woven geometries with relatively high wetted area fractions and so it becomes inaccurate when used for a granular surface under a negative (suction) pressure (208). Our simulation results indicate that slip length is strongly dependent on pressure (wetted area fraction) at low hydrostatic pressures, but the dependence becomes progressively weaker at higher pressures (wetted area fractions). It should also be noted that the difference between b_u and b_{app} increases in negative pressure. In the negative pressure, slip length increases due to the decrease of wetted area fraction and also due to the penetration of the shear free AWI into the water domain. b_{app} cannot capture the increase in slip length due to the protrusion of the AWI into the water domain, because it was derived for flat AWI. But accurate AWI shape obtained from SE was used for the calculation of b_u. So, both of these effects were taken care of while calculating b_u. That's why b_u was much higher compared to b_{app} under negative pressure.

It is important to mention that slip length over a SHP surface comprised of sharp-edge pores may reach a maximum value with decreasing hydrostatic pressure as discussed in

some pioneering works such as (92, 93, 206, 210, 211). However, this was not observed for our granular coatings where the unpinned AWI could easily move up or down in response to pressure (wetted area fraction is pressure-dependent here, and it varies monotonically with pressure). Figure 5.4c shows slip velocity contour plots along the AWI for a coating with a random particle arrangement at two different pressures of $P_h = -350$ Pa and $P_h = 900$ Pa. It can be seen that slip velocity is much higher (and so the slip length is bigger) when the coating is exposed to a negative pressure.

In a previous work, Samaha et al. (81) reported that the drag reduction performance of microfabricated surfaces comprised of randomly distributed sharp-edged microposts were significantly better than that of a similar surface with a staggered arrangement of microposts at low solid area fractions. They showed that with the random post configuration, there was always a possibility that the flow would find larger passages between the posts leading to a higher overall slip velocity. However, it is important to note Samaha et al. (81) assumed a flat profile for the AWI between their sharp-edged posts. As shown in Figure 5.4, the shape and position of the AWI varies with pressure. Deflection of the AWI under pressure has an adverse effect on the drag reduction performance of a SHP surface as mentioned by Sbragaglia and Prosperetti (212). Deflection of the AWI is larger in regions where particles are farther away from each other in a SHP coating with randomly distributed particles, and this tends to work against (or perhaps cancel) the positive effect of having a larger local passage area mentioned by Samaha et al. (81). This further highlights the importance of including the AWI curvature in studying drag reduction performance of SHP surfaces.

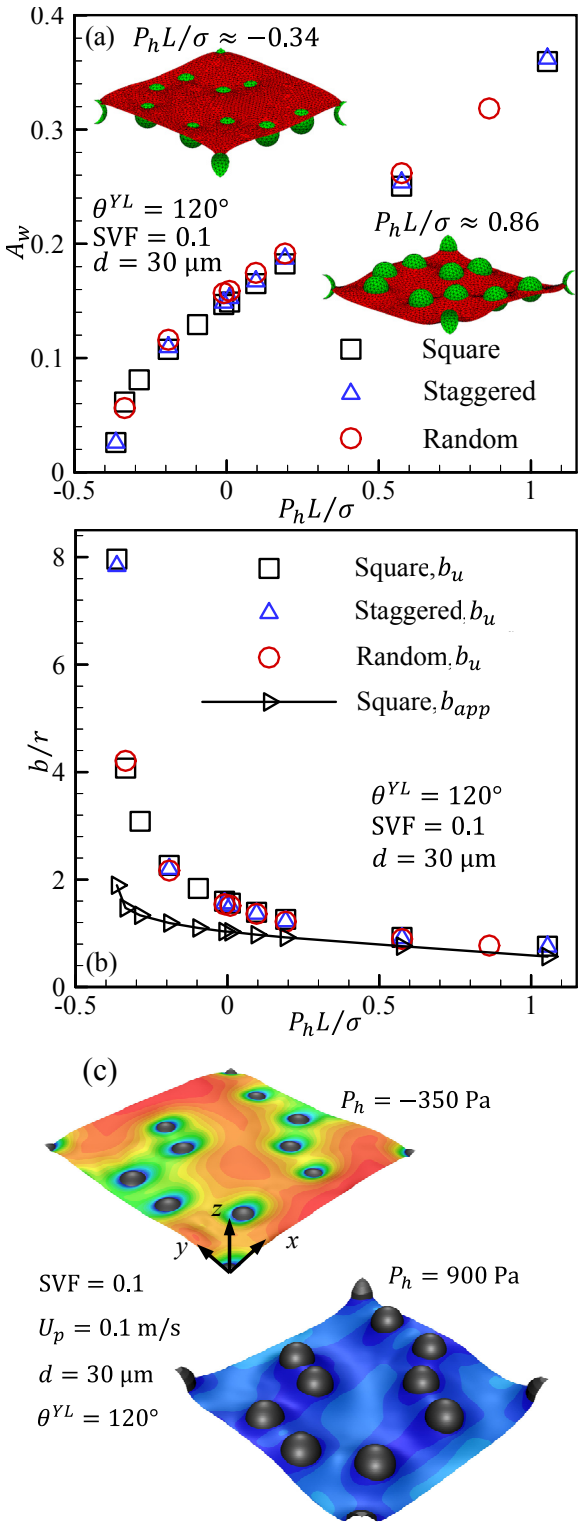

Fig. 5.4: Effects of normalized hydrostatic pressure on wetted area fraction (a) and normalized slip length (b) for coatings with square, staggered, and random particle arrangements. Contours of slip velocity in the x-direction for coating with random particle distributions at hydrostatic pressures of $P_h = -350$ Pa and $P_h = 900$ Pa are given in (c). Dark blue to dark red represent slip velocity from 0 to 0.0382 m/s. For all these cases Re = 17.8.

5.6.2 Effects of coatings' particle diameter on slip length

Effects of particle diameter on coatings' effective slip length are discussed in this section. Since identical slip lengths were obtained for coatings with ordered and random particle arrangements (see Section 5.6.1), we only consider coatings with square particle packing in this section.

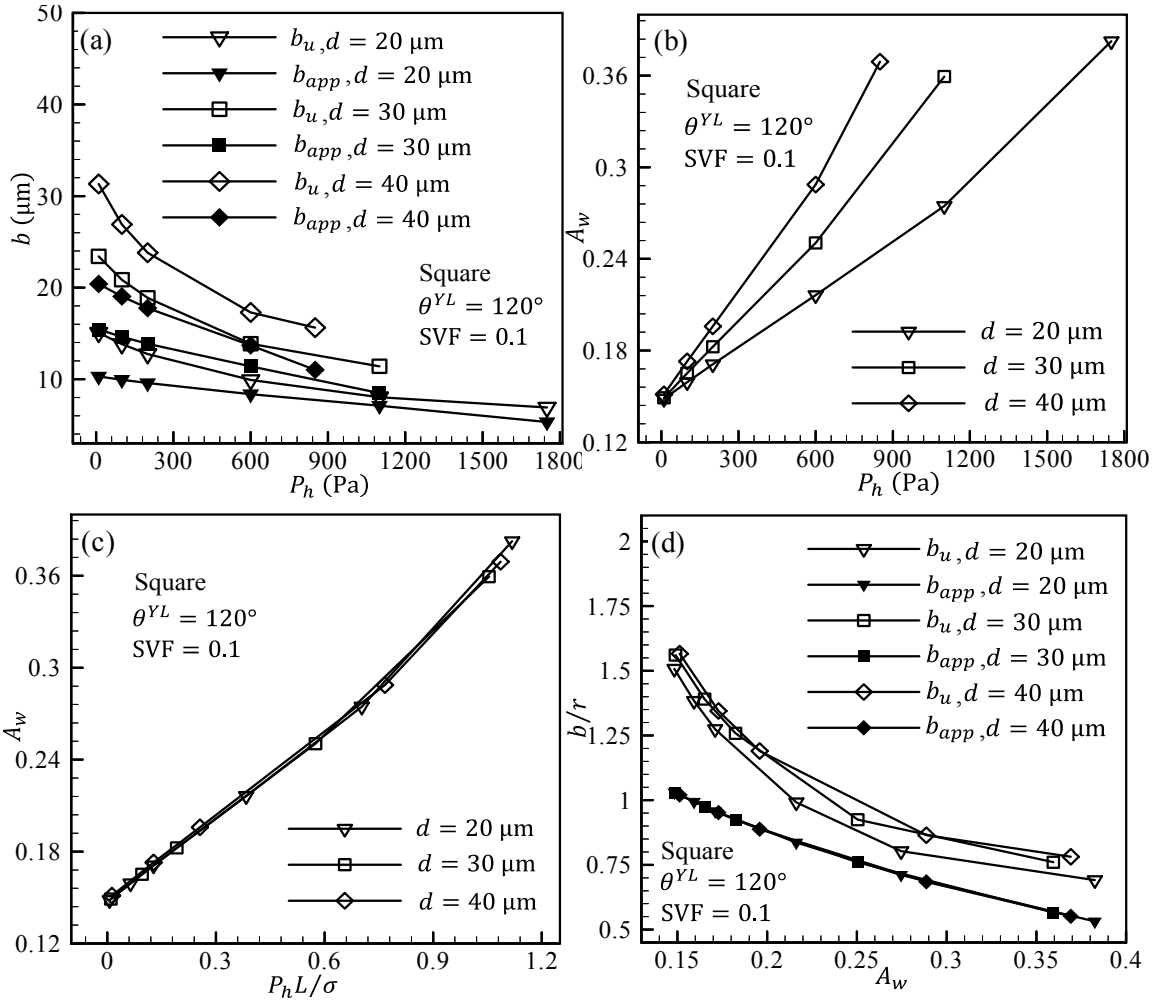

Fig. 5.5: Effects of pressure on slip length (a) and wetted area fraction (b) for coatings having a square particle arrangement made of particles with different diameters. Wetted area and slip length data are shown in dimensionless forms in (c) and (d), respectively. For all these cases $\mathrm{Re} = 17.8$.

Figures 5.5a, and 5.5b show the effects of pressure on slip length and wetted area fraction for coatings with a fixed SVF of 0.1 but varying particle diameters. It can be seen that the slip length and wetted area fraction both increase with increasing particle diameter. This rather surprising behavior can be attributed to the fact that for a surface with a given SVF, decreasing diameter of

the particles increases the number of particles per unit area of the surface (although the wetted area of each particle will be smaller), and this tends to prevent the formation of a strong slip velocity along the AWI.

In a previous work on 2D flow in microchannel (213), it was shown that a surface having fewer number of large slip patches provides more drag reduction than a surface having large number of smaller slip patches. This effect can also be explained using Equation 5.7, where effective slip length shows more dependence on the pitch between the particles L (linearly dependent on particle size) than on the wetted area fraction A_w (independent of particle size at zero pressure, but mildly dependent on particle size at higher pressures) when SVF is kept constant. To further discuss this effect we present the coatings' wetted area fraction versus dimensionless pressure in Figure 5.5c. It can be seen that the wetted area fraction is a single-valued function of dimensionless pressure (no dependence on particle size). On the other hand, presenting dimensionless slip length versus wetted area fraction (see Figure 5.5d), we can observe some dependence on particle size (albeit weak). This again indicates that the wetted area (or SAF/GAF) alone is not sufficient for slip length prediction. It is however, interesting to note that a pressure-independent wetted area model (Eq. 5.7) fails to recognize this dependence (see the solid symbols in Figure 5.5d).

It is also interesting to note that according to Equation 5.9, wetted area fraction is a linear function of SVF ($\pi(d/L)^2/6$) for a coating with particles packed in a square arrangement, when the pressure is zero (i.e., when the immersion angle is a constant number

$\alpha = 180^o - \theta^{YL}$). This is why wetted area fraction is independent of particle diameter if the SVF is kept constant and in the absence of hydrostatic pressure (see Figure 5.5b).

5.6.3 Effects of coatings' solid volume fraction on slip length

Effects of varying a coating's SVF on its drag reduction performance are shown in Figure 5.6a. It can be seen that the effective slip length decreases with an increasing SVF for all the three types of coatings considered (predictions of Equation 5.7 are also added for the case of coatings with square particle packing for comparison). This is primarily because the coatings' wetted area fraction increases monotonically with increasing the SVF (see the inset in Figure 5.6a). Also, it can be seen that the arrangement of the particles has no significant effects on the wetted area fraction or on slip length. To better visualize the effects of the SVF on slip length, slip velocity is shown in Figure 5.6c for coatings with ordered and random particle positions at two different SVFs of 0.05 and 0.25 on the same plot. Higher slip velocities are evident for coatings with lower SVFs.

Figure 5.6b shows the effects of SVF on slip length under an arbitrary suction pressure of -100 Pa. For the sake of brevity, we have only considered coatings with square particle packing. As expected, slip length decreases with the increasing SVF, and the rate of decline is higher at lower SVFs. Predictions of Equation 5.7 are also added to this figure for comparison, and it can be seen that this equation significantly under predicts the slip length at low SVFs.

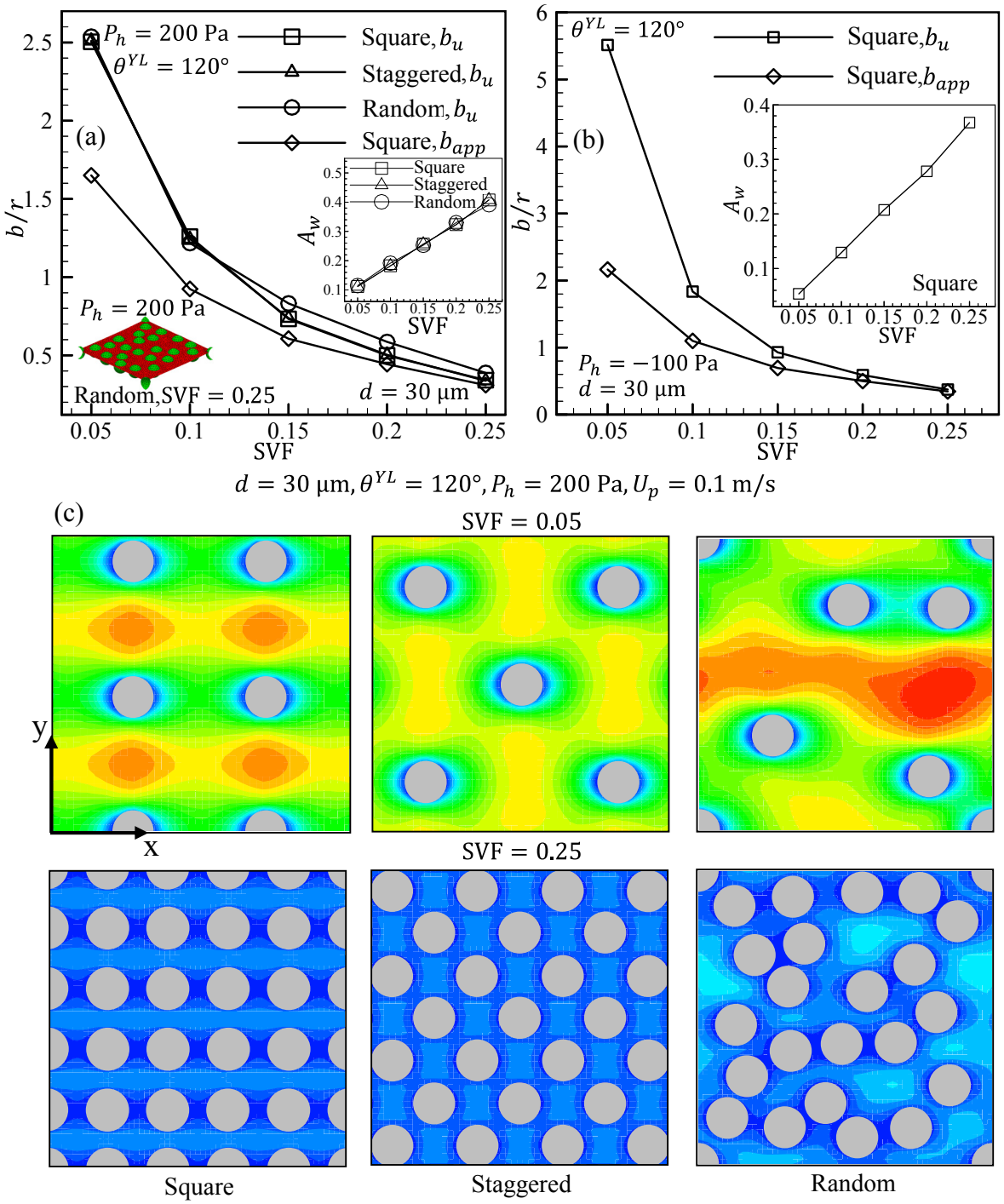

Fig. 5.6: Effects of SVF on the normalized slip length under arbitrarily chosen positive (a) and negative (b) hydrostatic pressures (wetted area fractions are given as inset). (c) Contours of slip velocity in the x-direction for coatings with square, staggered, and random particle arrangement at SVFs of 0.05 and 0.25. Dark blue to dark red represents slip velocity from 0 to 0.0263 m/s . For all these cases Re = 17.8 .

5.6.4 Effects of coatings' Young–Laplace contact angle on slip length

Our simulations conducted for coatings with different YLCAs indicate that slip length increases while increasing the YLCA, as can be seen in Figure 5.7. This is because the wetted area fraction decreases with increasing YLCA as the AWI penetrate less deeply into the pore space between the particles when the YLCA is higher.

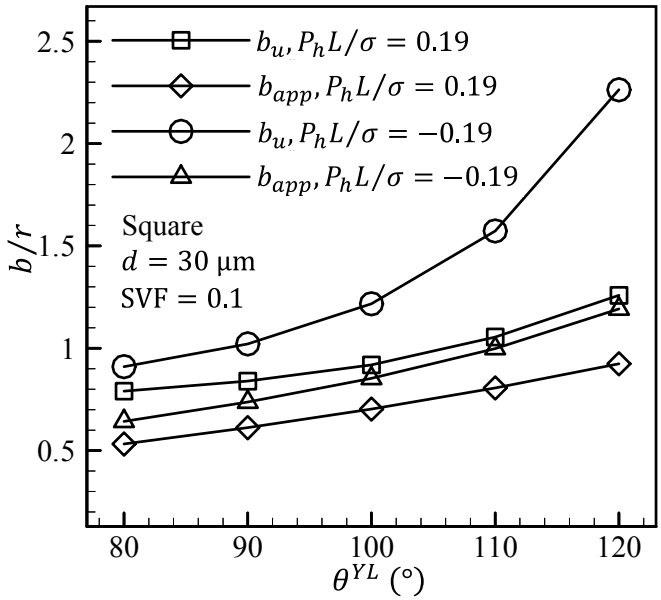

Fig. 5.7: Effect of Young–Laplace contact angle on normalized effective slip length for coatings with square particle arrangements. For all these cases $\mathrm{Re} = 17.8$.

Our results indicate that slip length increases more significantly with YLCA under suction pressures. Predictions of Equation 5.7 are also added to Figure 5.7, and it can once again be seen that they under-predict the numerical simulation results. While the results presented here are obtained for coatings with square particle packing, we expect similar performances from coatings with random particle distributions based on the observations made in earlier parts of this paper.

5.6.5 Effects of particles' spatial distribution on slip length

In a recent study, Vidal and Botto (207) showed that arranging particles in a square reticulated pattern (see the inset in Figure 5.8a) results in higher slip length values compared to uniform square packing. In their study, these authors assumed the particles to have a YLCA of 90 degrees and also ignored the effects of the AWI curvature in their calculations (i.e., the effects of hydrostatic pressure on AWI and so on slip length were ignored). In this section, we simulate slip length performance of these two particle spatial configurations under positive and negative hydrostatic pressures (AWI is not assumed to be flat). Our objective here is to see how coatings with reticulated-square particle packing and uniform-square particle packing compare to one another in terms of drag reduction performance. To do so, we obtained the 3-D shape of the AWI over coatings with reticulated particle arrangements under different positive and negative hydrostatic pressures and used them in our slip length calculations. We also simulated the coatings' slip length at zero hydrostatic pressure (assuming a flat AWI) to be able to directly compare our numerical data with those in (207) before discussing our pressure-dependent slip length results. Here it should be noted that Vidal and Botto (207) used the following equation to calculate slip length,

$$b = \left. \frac{\langle u \rangle}{\frac{d\langle u \rangle}{dz}} \right|_{z=\frac{d}{2}} \tag{5.10}$$

Here $\langle u \rangle = \frac{1}{L^2} \iint u dx dy$. The slip length values computed using the present method and that of Vidal & Botto (207) are within the margin of numerical errors (about 10%). We chose the method of calculating slip length using Eq. 5.6 because it is the same way an experimentalist would calculate slip length using a rheometer (92, 192, 206, 208). Moreover, when the pressure

is negative, the AWI may move above the $z = d/2$ baseline, which renders the slip length calculations using Eq. 5.10 inaccurate.

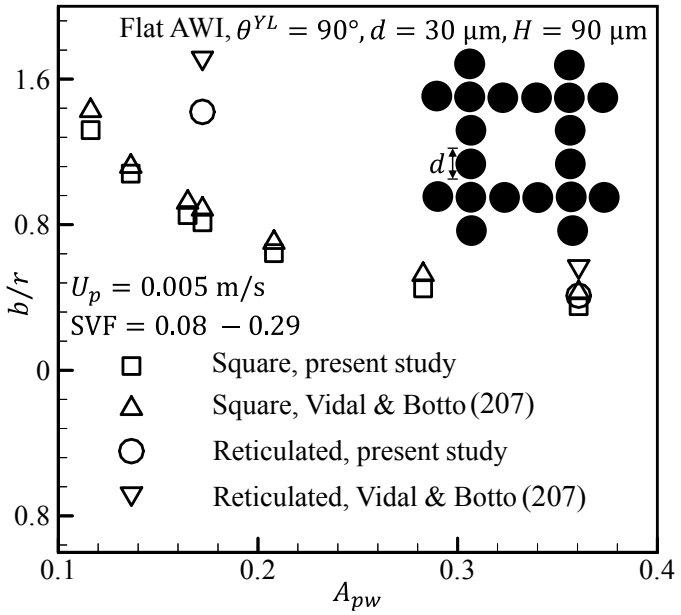

Fig. 5.8: Comparison of the normalized slip length values obtained from the present study with those reported by Vidal and Botto (207) for square and reticulated particle packing. The air–water interface is assumed to be flat for the results presented in this figure. For all these cases $\mathrm{Re} = 0.45$.

Figure 5.8 compares the slip length values (normalized by particle radius r) obtained from our simulations with those reported by Vidal and Botto (207) (flat AWI, and $\theta^{YL} = 90^o$) versus A_{pw} which is the wetted area fraction definition based on the projected wetted area of solid particles in the work reported by Vidal and Botto (207). Note that, to ease meshing for the space between the particles for both the AWI tracking and slip length simulations, we had to consider a small gap ($\varepsilon = 0.1d$) between the particles (unlike the geometry of reticulated-square particle packing studied by Vidal and Botto, 207). This is believed to be the reason for around 24% of the mismatch between our results and those reported by Vidal and Botto (207) for the coatings with reticulated particle packing.

However, for the square particle packing we considered what was the similar to that of Vidal and Botto (207). The mismatch between our results and that of Vidal and Botto (207) for square particle packing was around or less than 10% i.e. within the margin of numerical errors. It can obviously be seen that reticulated particle packing results in significantly higher slip lengths compared to square particle packing but only for low A_{pw} values, as was also discussed by Vidal and Botto (207).

Figure 5.9a compares the pressure-dependent drag reduction performance of two coatings having an identical SVF of 11.5% but with different particle arrangements of reticulated and square packing. It can be seen that the drag reduction advantage of the reticulated arrangement sharply declines as the hydrostatic pressure is increased from a negative suction pressure to a positive compression pressure. When calculating the wetted area fractions of these two coatings, it can be seen in Figure 5.9b that both coatings have identical wetted area fractions and they both increase as the pressure increases from negative suction pressure to a positive compression pressure (note that the wetted area fraction definition of Vidal and Botto (207) A_{pw}, is only valid for $\theta^{YL} = 90^o$ in the absence of a non-zero hydrostatic pressure). It is also important to notice in Figures 5.9a and 5.9b that the reticulated particle arrangement results in accelerated failure of the coating under pressure as the large open area between the particles is a weak point in resisting against hydrostatic pressure. A Cassie to Wenzel transition was observed in our simulations at $P_h = 275$ Pa for the reticulated coating and $P_h = 885$ Pa for the coating with square particle packing (shown in Figure 5.9a with a dashed line). Likewise, the critical suction pressures for reticulated and square particle coatings were found to be about 775 Pa and 930 Pa, respectively. Predictions of Equation 5.7 are also added to Figure 5.9a for comparison. It can be seen that Equation 5.7

under-predicts the slip length for coatings with square particle packings but, it over-predicts the slip length of coatings with reticulated particle arrangements for hydrostatic pressure greater than -450 Pa and under-predicts the slip length for hydrostatic pressure smaller than -450 Pa.

For completeness of our comparison, slip velocity along the AWI is shown in Figures 5.9c – 5.9f for coatings with reticulated and uniform square particle packings under zero and 250 Pa pressures. It can be seen that the AWI curvature, caused by the positive hydrostatic pressure over the coating, tends to lower the slip velocity over the coating and therefore deteriorates the coating's drag reduction performance. This effect however affects the performance of the coating with uniform particle distribution much less severely than it does to the coating with reticulated particles. Both the coatings with reticulated and square particle packing shows significant increase in slip length under negative suction pressure, although the slip length for coating with reticulated particle packing was significantly higher than the slip length for coating with square particle packing under negative suction pressure. Drag reduction performance of coatings with square or reticulated particle packings with YLCAs other than $\theta^{YL} = 90^o$ is qualitatively similar to those with $\theta^{YL} = 90^o$ but higher effective slip length values should be expected from more hydrophobic coatings.

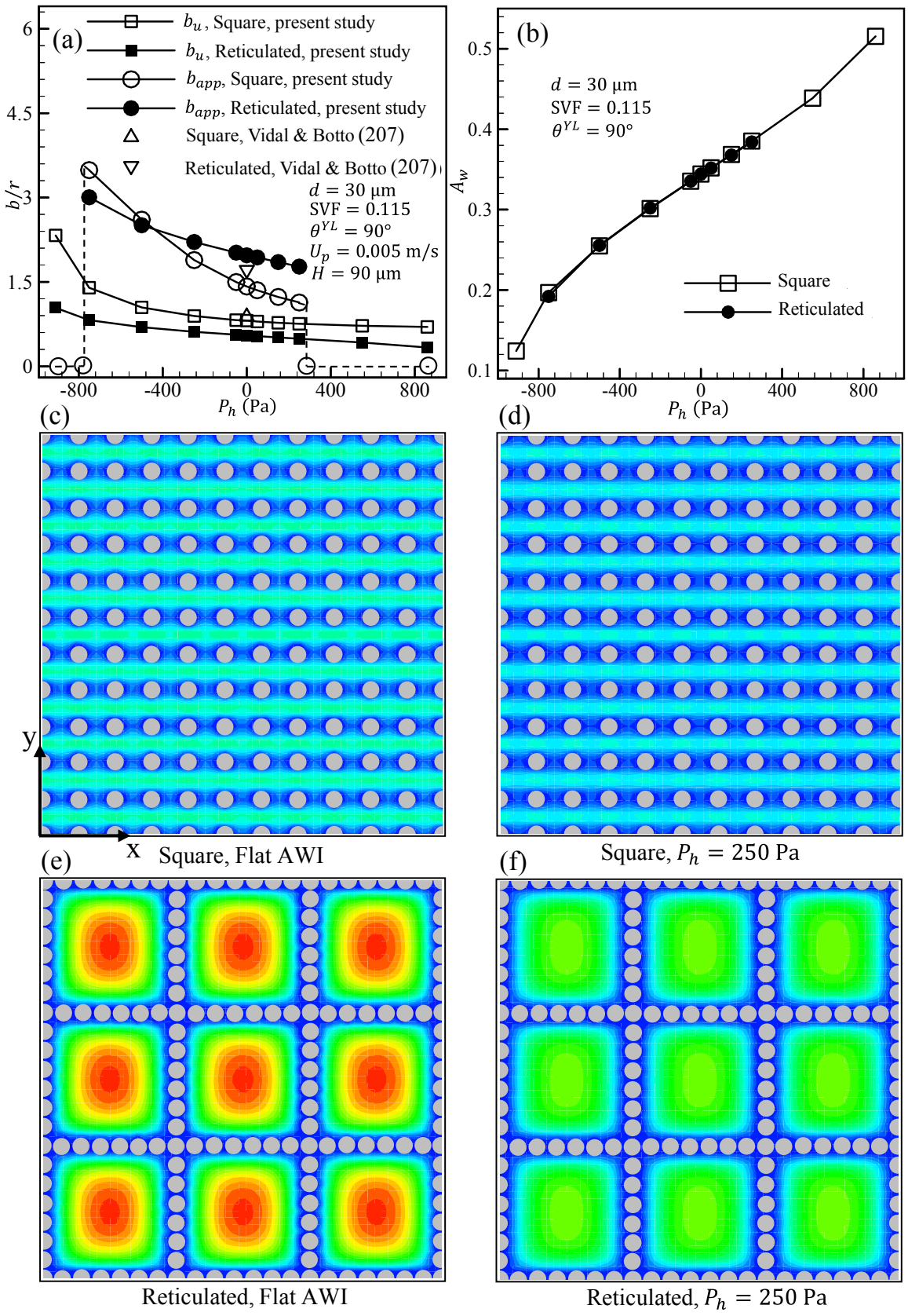

$d = 30$ µm, $\theta^{YL} = 90°$, SVF = 0.115, $U_p = 0.005$ m/s

Fig. 5.9: Comparison between drag reduction performance and wetted area fraction for coatings with different particle arrangements are shown in this figure (normalized slip length values for coatings with staggered and random particle arrangements are almost identical to those of coatings with square arrangement and so they are not shown). The air–water interface is simulated under pressure for the results presented in (a). The dotted line in (a) is added to indicate that the coatings with reticulated particles fail to remain dry for hydrostatic pressure smaller than -775 Pa and greater than about 275 Pa. Wetted area fractions are given in (b) as a function of pressure. Contours of slip velocity in the x-direction for a coating with square particles arrangements with (c) flat (zero pressure with an YLCA of 90 degree) air-water interface and (d) curved (arbitrary positive pressure of 250 Pa) air–water interface. Contours of slip velocity in the x-direction for a coating with reticulated particles arrangements with (e) flat (zero pressure with an YLCA of 90 degree) air-water interface and (f) curved (arbitrary positive pressure of 250 Pa) air–water interface. Dark blue to dark red represents slip velocity from almost 0 to 0.0017 m/s. For all these cases $\mathrm{Re} = 0.45$.

5.7 Conclusions

Effects of a granular coating's microstructure (Young–Laplace contact angle, particle diameter, solid volume fraction, and particle spatial arrangement) on its drag reduction efficiency are studied within this paper. With all other parameters kept constant, better drag reduction results were obtained for coatings with lower solid volume fractions, higher YLCAs, or larger particles. It was also found that the drag reduction performance of submerged SHP coatings decreases with increasing hydrostatic pressure, in agreement with observation reported in the literature (78, 90, 91, 201). However, under suction pressure (e.g., the Venturi effect) the drag reduction efficiency of a granular coating seems to increase monotonically with decreasing pressure, in contrast to coatings comprised of sharp-edged pores (92, 93).

Our study revealed that the spatial distribution of the particles has no significant effect on drag reduction, except for the case of coatings with reticulated particle arrangement, for which some improvements were observed. This advantage however, tends to decay rather quickly with increasing pressure. Moreover, SHP coatings with reticulated particle

patterns tend to fail (transition to the Wenzel wetted state) under elevated hydrostatic pressures in comparison to their counterparts having square or staggered particle arrangements.

Chapter 6. Fibrous Liquid-Infused Surface with Trapped-Air for Drag Reduction

6.1 Introduction

Friction between a rough surface and a body of water may be reduced if the surface is made of a hydrophobic material and it has the ability to trap a layer of air between the peaks and valleys of its asperities (55, 56, 80, 84,191-194,212). A rough hydrophobic surface is often referred to as a superhydrophobic (SHP) surface if it exhibits a water contact angle of 150 degrees or more (84, 192). A SHP surface can be produced by carving the required roughness into a hydrophobic smooth surface (texturing), or by depositing the roughness onto the surface in the form of a granular or fibrous coating (45, 50-52, 58, 61, 62, 78, 96, 214). Regardless, a submerged SHP surface may lose its air layer under excessive pressures and therefore transition from the Cassie (fully dry) state to the Wenzel (fully wetted) state. A wetted SHP surface can no longer produce a friction-reduction effect. The departure from the Cassie state can be caused by two main failure mechanisms. The first is the imbalance of mechanical forces acting on the air–water interface (AWI), which leads to instantaneous penetration of water into the air-filled pores of the SHP surface (45, 87, 203, 215, 216, 217, 218). The second cause of surface failure is the gradual dissolution of the entrapped air into the surrounding water as described in detail in many previous studies (94 - 100).

It has been reported that one can produce a slippery surface by infusing the pores of a rough surface with a lubricant, and that such a surface can have a lower friction coefficient against when used for a more viscous fluid (102). While a liquid–infused surface (LIS) does not suffer from the air dissolution problem of the conventional SHP surfaces, it is still prone to failure due

to shear-induced lubricant drainage (104). In addition, the drag reduction benefit of a LIS surface is quite small if the working fluid (the fluid flowing over the surface) is less viscous than the fluid used as the lubricant. To improve the drag reduction performance of a LIS surface, Hemeda & Tafreshi (103) suggested to place a layer of air underneath the lubricant layer and supported their hypothesis with data from numerical simulation. The liquid–infused surface with trapped air (LISTA) design of Hemeda and Tafreshi (103) however, is prone to lubricant drainage, similar to the LIS surfaces (or perhaps even more prone). To help stabilize the lubricant in the LISTA design, here we propose to place fibers of different wetting properties in the lubricant and air layers; i.e., a LISTA surface made of two layers of loosely-packed parallel fibers (fibers can potentially help to dampen the growth of instability waves in the lubricant layer). As shown in Figure 6.1, the top (lubricant-infused) and bottom (air-trapping) layers are expected to be made of oleophilic and oleophobic fibers, respectively. Making the LISTA surface from fibrous layers instead of microfabrication also reduces the cost of surface manufacturing. The working fluid and lubricant in our study are arbitrarily assumed to be water and n-Hexadecane. Obviously, more drag reduction can be expected from the proposed design if one considers a working fluid that is more viscous than the infused lubricant (we consider the case where achieving drag reduction is the hardest for demonstration).

In the remainder of this chapter, we quantify the drag reduction performance of fibrous LISTA and study the effects fiber diameter or packing fraction of the fibers on the overall performance of the surface. This requires accurate information about the shape and position of the water–lubricant interface (WLI) and lubricant–air interface (LAI) as a function of hydrostatic pressure over the surface (Section 6.2). With the shape and

position of the WLI and LAI obtained, we then solve the Navier–Stokes equations for water outside the fibrous LISTA and the infused lubricant inside it (Section 6.3). This information is then used to quantify the effects of microstructural parameters of the fibrous LISTA coatings (e.g., fiber diameters, porosity, contact angles, thickness of lubricant layer) on their drag reduction performance (Sections 6.4 and 6.5).

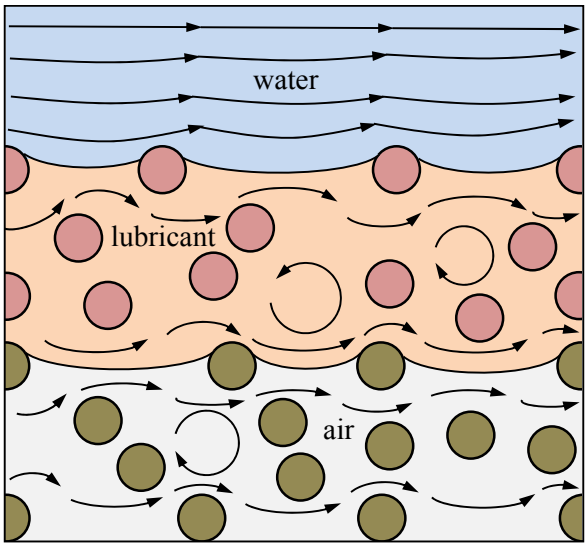

Fig. 6.1: Schematic representation of FLISTA made of parallel fibers in random arrangement. Maroon circles represent the oleophilic fibers and brown circles represent the oleophobic fibers.

6.2 Interface Tracking

As was mentioned earlier in Section 6.1, our study here is focused on analyzing the drag reduction performance of fibrous LISTA coatings comprised of two layers of parallel fibers with different wetting properties (see Figure 6.1). The coatings are considered to be submerged in water (working fluid), and the flow is assumed to be in a direction transverse to the fibers in a shear (or channel) flow configuration. In this section, we present a force balance approach to predict the shape of the above–mentioned WLI and LAI for any combinations of fiber diameters or contact angles and to track their penetration into the coating under elevated hydrostatic pressures.

We describe our interface tracking algorithm using an ordered arrangement of fibers in each layer (see Figure 6.2a) for the clarity of the presentation, but we then move on to the case of fibers with random arrangements. The equilibrium shape and position of WLI and LAI depend on the hydrostatic pressure P_h, fiber diameter d_f, horizontal distance between the fibers in a row s, vertical distance between the fibers in a column h, contact angle of water with fibers θ_W, contact angle of lubricant with fibers θ_L, surface tension between water and lubricant σ_{WL}, and surface tension between lubricant and air σ_{LA}. The solid volume fraction (SVF) for the ordered arrangement of fibers discussed here can be defined as $\xi = \pi d_f^2 / 2hs$. Assuming WLI and LAI to be circular arcs (95), one can consider the forces acting on WLI to relate the hydrostatic pressure P_h to the radius of curvature of WLI R_W and that of LAI R_L, i.e.,

$$P_h - \frac{\sigma_{LA}}{R_L} = \frac{\sigma_{WL}}{R_W} \tag{6.1}$$

One can also write an equation for the relationship between R_W and R_L in terms of their corresponding immersion angles α_W and α_L as (87),

$$R_W = -\frac{\left(s - d_f \sin\alpha_W\right)}{2\sin\left(\theta_W + \alpha_W\right)} \tag{6.2a}$$

$$R_L = -\frac{\left(s - d_f \sin\alpha_L\right)}{2\sin\left(\theta_L + \alpha_L\right)} \tag{6.2b}$$

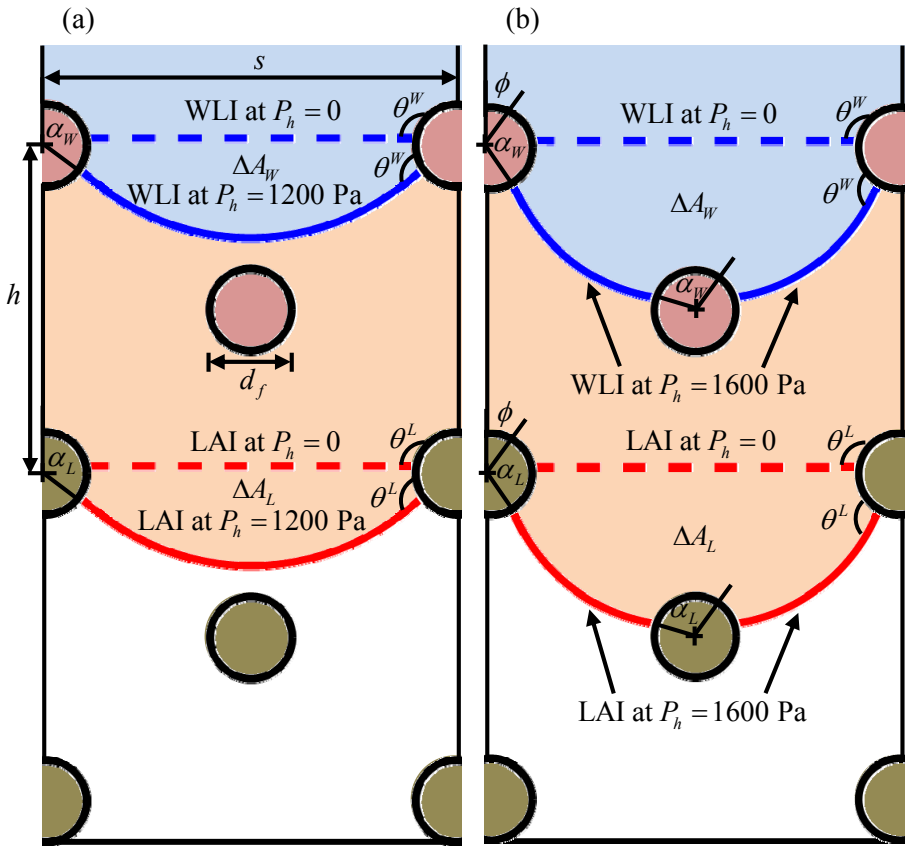

Fig. 6.2: WLI and LAI in a unit cell of FLISTA coating with ordered fibers under hydrostatic pressure (a) $P_h = 1200$ Pa and (b) $P_h = 1600$ Pa. Note that, WLI and LAI touches the fiber underneath them at $P_h = 1600$ Pa. Here, $d_f = 20$ μm, $\theta_W = \theta_L = 100^o$, $s = 100$ μm and $h = 80$ μm.

Note that as the lubricant is incompressible, its volume remains constant regardless of how R_W and R_L vary with hydrostatic pressure or fiber properties. More specifically, considering the volume of the lubricant displaced due to WLI and LAI sagging under pressure (relative to when there is no pressure), one can write (see Figure 6.2a),

$$\Delta A_W = \Delta A_L \tag{6.3}$$

where,

$$\Delta A_W = \frac{d_f^2}{8}\left\{2\left(\pi - \theta_W\right) + \sin 2\theta_W\right\} + \frac{R_W^2}{2}\left\{2\left(\alpha_W + \theta_W - \pi\right) - \sin 2\left(\theta_W + \alpha_W\right)\right\} - \frac{d_f^2}{8}\left(2\alpha_W - \sin 2\alpha_W\right) - \frac{d_f s}{2}\left(\cos\theta_W + \cos\alpha_W\right) \tag{6.4a}$$

and

$$\Delta A_L = \frac{d_f^2}{8}\left\{2\left(\pi-\theta_L\right)+\sin 2\theta_L\right\}+\frac{R_L^2}{2}\left\{2\left(\alpha_L+\theta_L-\pi\right)-\sin 2\left(\theta_L+\alpha_L\right)\right\}-\frac{d_f^2}{8}\left(2\alpha_L-\sin 2\alpha_L\right) - \frac{d_f s}{2}\left(\cos\theta_i+\cos\alpha_i\right) \tag{6.4b}$$

R_W, α_W, R_L, and α_L can be obtained for any hydrostatic pressure by solving Eqs. 6.1–6.4. Obviously, increasing the hydrostatic pressure results in WLI and LAI penetrating deeper into the coating, and at some pressure, the WLI and LAI will come into contact with fibers underneath them as shown in Figure 6.2b. In that case, Eqs. 6.1, 6.2, and 6.4 will change to a more general form as given below.

$$R_W = -\frac{\left(\frac{\sqrt{s^2+h^2}}{2}-d_f\sin\alpha_W\right)}{2\sin\left(\theta_W+\alpha_W\right)} \tag{6.5a}$$

$$R_L = -\frac{\left(\frac{\sqrt{s^2+h^2}}{2}-d_f\sin\alpha_L\right)}{2\sin\left(\theta_L+\alpha_L\right)} \tag{6.5b}$$

$$\Delta A_W = -\frac{sd_f}{4}\cos\theta_W+\frac{sh}{8}-\frac{\left(\sqrt{s^2+h^2}-d_f\sin\alpha_W\right)d_f\cos\alpha_W}{4} + \frac{R_W^2}{2}\left\{2\left(\alpha_W+\theta_W-\pi\right)-\sin 2\left(\alpha_W+\theta_W\right)\right\}+\frac{d_f^2}{16}\left\{2\left(\pi-\theta_W\right)+\sin 2\theta_W\right\}-\frac{d_f^2\alpha_W}{8} \tag{6.6a}$$

$$\Delta A_L = -\frac{sd_f}{4}\cos\theta_L+\frac{sh}{8}-\frac{\left(\sqrt{s^2+h^2}-d_f\sin\alpha_L\right)d_f\cos\alpha_L}{4} + \frac{R_L^2}{2}\left\{2\left(\alpha_L+\theta_L-\pi\right)-\sin 2\left(\alpha_L+\theta_L\right)\right\}+\frac{d_f^2}{16}\left\{2\left(\pi-\theta_L\right)+\sin 2\theta_L\right\}-\frac{d_f^2\alpha_L}{8} \tag{6.6b}$$

These equations can numerically be solved (e.g., using *Mathematica*) to obtain the AWI and LAI profiles for the given pressure.

With surface tension for water and n-Hexadecane being σ_{WA}= 0.072 N/m and σ_{LA}= 0.027 N/m, respectively, we estimated the water–lubricant surface tension to be σ_{WL}=0.045 N/m using Antonoff's rule (219) $\sigma_{WL} = \sigma_{WA} - \sigma_{LA}$.

Figure 6.3 shows a flowchart created on the basis of the above equations for tracking the fluid–fluid interfaces among fibers with random arrangements. For the case of random fiber arrangements, one has to compute the shapes and positions of the multiple fluid–fluid interfaces throughout the domain (unlike the case of fibers in ordered arrangement). Here we assumed the fibers in the top layer of the coating be at the same height from the substrate but randomly distributed in the horizontal direction. The shapes and positions of WLIs and LAIs are computed iteratively starting with an initial guess for R_W and R_L for a given hydrostatic pressure. N_{WL} and N_{LA} in the flowchart denote the number of WLIs and LAIs in the domain, respectively. We denote the number of fibers at the top layer of the coating and at the bottom of the lubricant layer by N_{f1} and N_{f2}, respectively. We start with assuming $N_{WL} = N_{f1} - 1$ and $N_{LA} = N_{f2} - 1$, but update these numbers if WLIs and LAIs come into contact with a new fiber as they intrude into the coating under pressure. Note that different fluid–fluid interfaces experience different degrees of deflection and depth of penetration depending on the local arrangement of the fibers. The schematic diagrams in the inset in Figure 6.3 graphically describe the above mentioned WLI deformation and intrusion. Also note that, the total water volume change and total lubricant volume change should be calculated and updated every time WLI, and therefore LAI, are updated. The inset in the Fig. 6.3 shows an example of water volume change for fibers with random arrangements. In this case, the total water volume change ΔA_W is the sum of $\Delta A_{W,1}$ and

$\Delta A_{W,2}$. Here, $\Delta A_{W,2}$ is calculated using Eq. 6.4a and $\Delta A_{W,1}$ is calculated numerically. Similarly, the total lubricant volume change is calculated. As can be seen in the flowchart in Figure 6.3, the value of R_L is updated until the total water volume change becomes equal to the total lubricant volume change. At the end, R_W and R_L must satisfy Eq. 6.1.

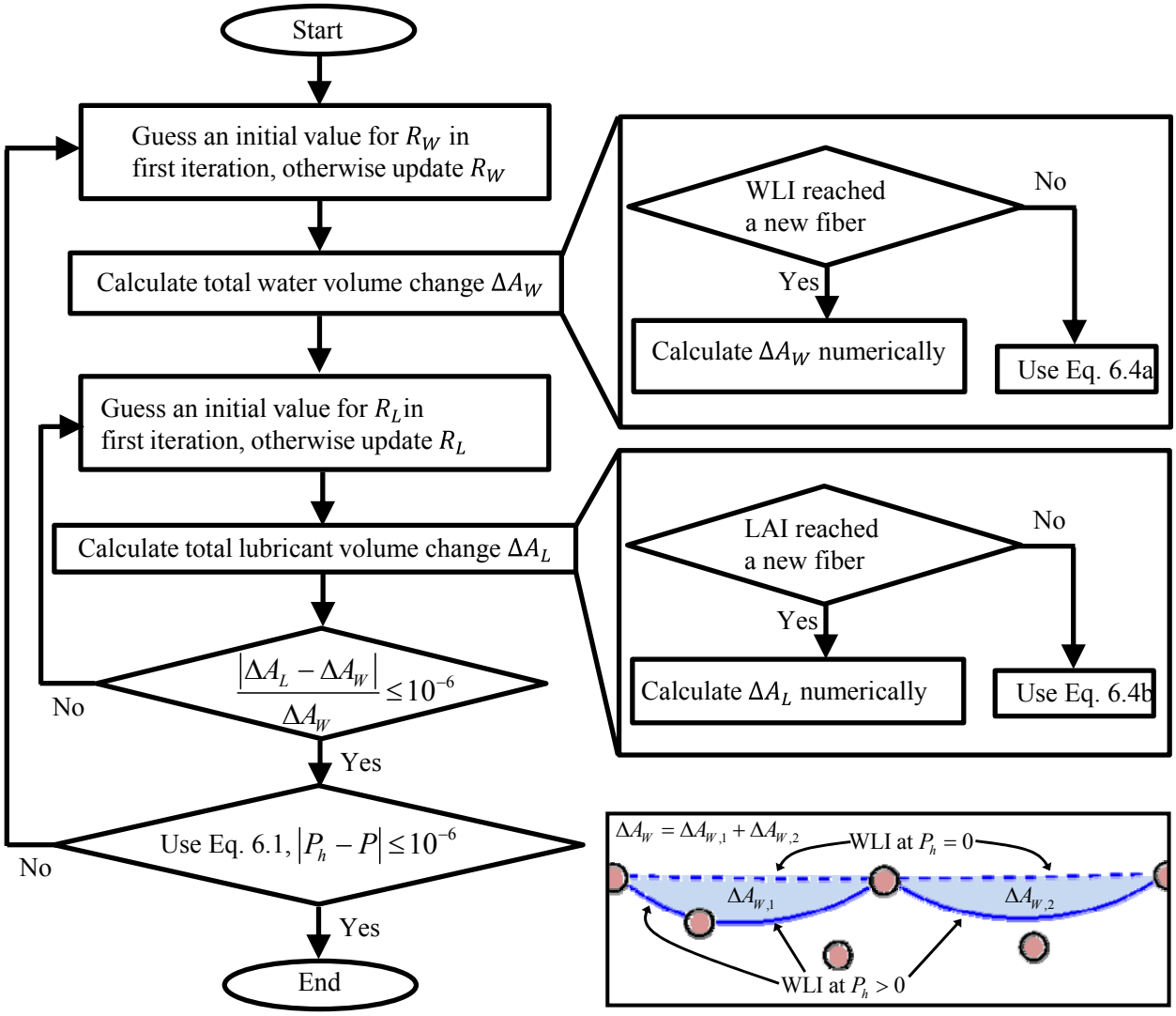

Fig. 6.3: Flow chart for the algorithm for computing shapes and positions of the WLIs and LAIs for a FLISTA coating made of parallel fibers in random arrangement. The inset in the Figure shows schematic representation of the water volume changes at two different segments of the FLISTA coating.

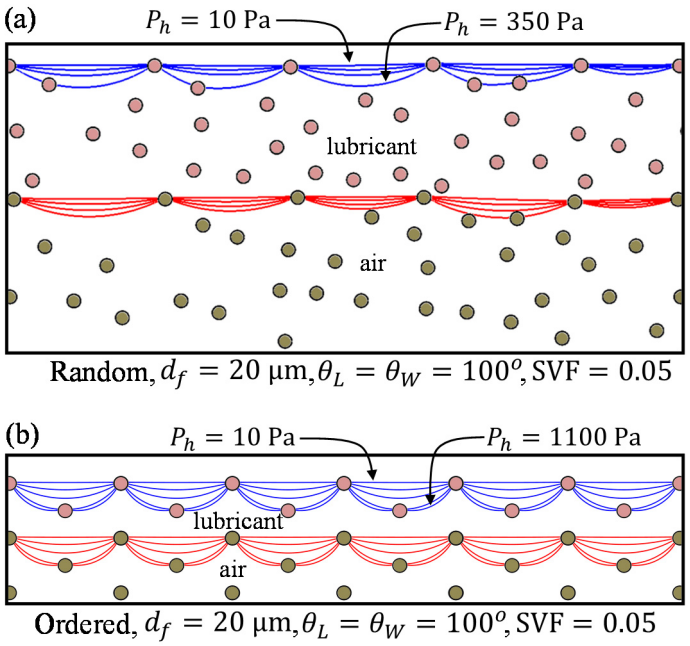

Fig. 6.4: (a) Tracking of WLI and LAI in a FLISTA coating made of parallel fibers in random arrangement at $P_h = 10,\ 100,\ 200,\ 350$ Pa. (b) Tracking of WLI and LAI in a FLISTA coating made of parallel fibers in ordered arrangement at $P_h = 10,\ 250,\ 500,\ 800,\ 1100$ Pa. Here, $d_f = 20$ μm, $\theta_W = \theta_L = 100^o$ and SVF = 0.05. For the FLISTA coating with ordered arrangement of fibers $s = 160$ μm.

Figure 6.4 shows examples of our coupled WLI–LAI interface tracking produced for FLISTA coatings comprised of random and ordered fibers with fiber diameter $d_f = 20$ μm, SVF $\gamma = 0.05$ and YLCAs $\theta_W = \theta_L = 100^o$. Figure 6.4a shows the intrusion of the WLI and LAI into the FLISTA coating comprised of random arrangement of fibers as the pressure P_h increases from 10 Pa to 350 Pa. Figure 6.4b shows the same for the FLISTA coating comprised of ordered arrangement of fibers as the pressure P_h increases from 10 Pa to 1100 Pa.

6.3 Slip Length Calculation

Once the radius of curvature and the immersion angle for WLI and LAI are calculated, the flow field inside the water, lubricant, and air domains can be simulated by solving the Navier–Stokes equations (Eqs. 6.7–6.8) for each phase using the ANSYS Fluent package.

$$\frac{\partial u_i}{\partial x_i} = 0 \tag{6.7}$$

$$\rho u_j \frac{\partial u_i}{\partial x_j} = -\frac{\partial P}{\partial x_i} + \mu \frac{\partial^2 u_i}{\partial x_j \partial x_j} \tag{6.8}$$

Here u_i is the velocity component $(i = 1,2)$, x_i is the Cartesian coordinate directions, ρ is fluid density (water, lubricant, or air in their corresponding domains), P is pressure, and μ is fluid viscosity (water, lubricant, or air in each domain). In the present study, it is assumed that the fluid–fluid interfaces do not deform due to the influence of fluids motion (one-way coupling), which is a reasonable assumption given a Capillary number of $Ca \ll 1$ (see Aziz and Tafreshi [220] for more detailed discussion about importance of Capillary number in the context of a shear flow over superhydrophobic surfaces). The boundary conditions for a fluid at the interface with another fluid are that the tangential velocities and the shear stresses should be matching, and the normal velocities should be zero. For the WLI, instance for, we have:

$$\vec{u}_W . \hat{t} = \vec{u}_L . \hat{t} \tag{6.9}$$

$$\vec{u}_W . \hat{n} = \vec{u}_L . \hat{n} = 0 \tag{6.10}$$

$$\tau_W = \tau_L \tag{6.11}$$

where, $\vec{u}$ is the velocity vector, τ is the tangential shear stress, $\hat{n}$ and $\hat{t}$ are the normal and tangential unit vectors to the WLI. Following the approach of Gruncell et al. (221), each interface is modelled with two overlapping solid boundaries, one wall for each fluid.

Figure 6.5a describes our shear-flow simulation domain schematically. Periodic boundary conditions (PBCs) are considered for each phase in the streamwise direction. The computational domain was meshed using quadrilateral mesh refined near the fibers, WLI, and LAI. For each fluid–fluid interface, the velocity is first calculated in the domain having a higher viscosity and it is then used as a boundary condition for the domain with the lower viscosity. For the shear stress calculation however, we reversed this order as suggested by Gruncell et al. (221). The above steps are repeated in every iteration until a converged solution is obtained.

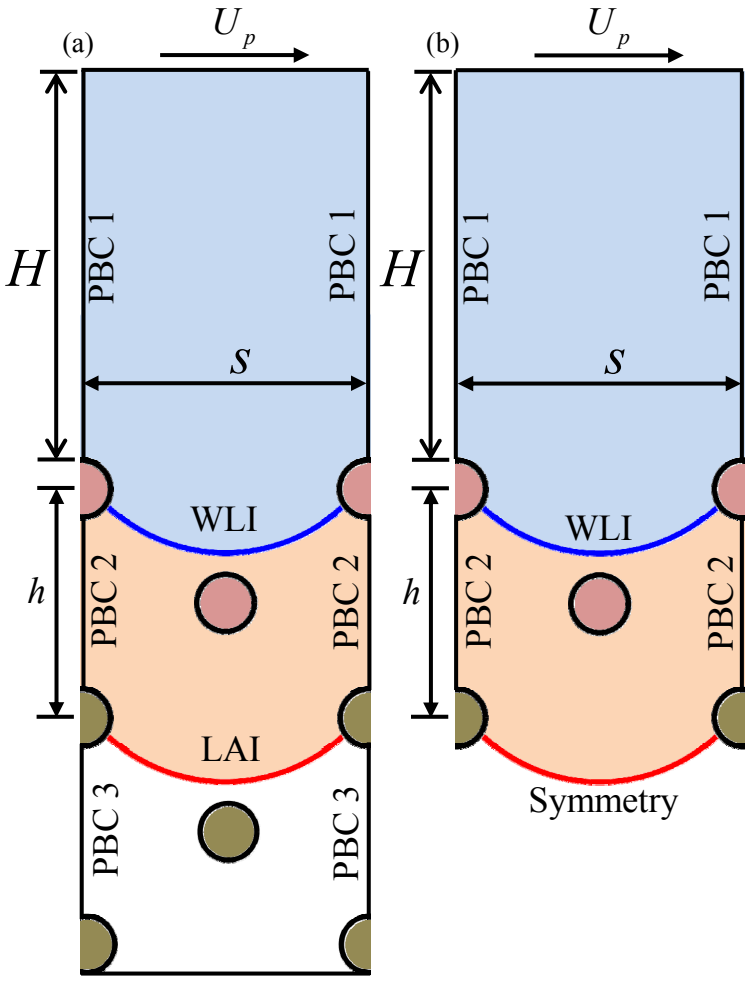

Fig. 6.5: Schematic representation of the computational domain for Couette flow over FLISTA coating made of parallel fibers in ordered/staggered arrangement. (a) Computational domain including the LAI.

(b) Computational domain with symmetry boundary condition approximated the LAI. Here, PBC denotes periodic boundary condition.

To reduce the size of the computational domain (and accelerate the speed of convergence), we examined the possibility of removing the air domain from the simulations and instead treating the LAI as a symmetry boundary (see Figure 6.5b). No significant difference was observed between the drag-reduction gain obtained from simulations conducted in the domain shown in Figure 6.5a and that obtained from the domain shown in Figure 6.5b. This was in fact expected as the air viscosity is much smaller than that of n-Hexadecane, i.e., air makes no significant resistant to flow field in the lubricant layer. The simulation results reported in this paper were therefore obtained using a symmetry boundary condition along the LAI. We also conducted a grid-independence study to ensure the suitability of the mesh size considered for the simulations. This study was performed at a hydrostatic pressure of $P_h = 500$ Pa, a fiber spacing of $s = 160$ μm, a fiber diameter of $d_f = 20$ μm, and with $h = 80$ μm, $H = 200$ μm, $\theta_W = \theta_L = 100^o$, $U_p = 10$ mm/s, and a lubricant-to-water viscosity ratio of $N = \mu_L / \mu_W = 3$. Negligible relative error was observed for simulations conducted with a mesh size smaller than $\delta < d_f / 25$.

6.4 Results and Discussion

In this section, we present our numerical simulation results obtained for to study the effects of microstructural parameters of a FLISTA coating (e.g. fiber diameter, fiber contact angle, fiber spacing) on its ability to generate a slip effect for a moving fluid (often quantified using the so-

called effective slip length) under different hydrostatic pressures. Following the work of Choi and Kim (192) or Srinivasan et al. (204), here we define effective slip length as,

$$b = \left(\frac{\tau_{ns}}{\tau_s} - 1 \right) H \tag{6.12}$$

where, τ_s and τ_{ns} are the shear stress exerted onto the upper plate in our shear-flow geometry with and without the slip-generating coating as the bottom surface, respectively.

Figure 6.6a shows an example of our flow field calculations conducted for water and lubricant (the WLI is shown in the figure with a black solid line) under three different hydrostatic pressures. Here solid volume fraction (SVF) of the coating is $\xi = 0.05$. Figure 6.6b shows slip length versus pressure for the LISTA coating with random fibers shown in Figure 6.6a. It can be seen that, unlike the case of a conventional SHP surfaces, the effective slip length generated by a FLISTA coating increases with increasing hydrostatic pressure. This is a significant effect (a unique attribute of the FLISTA design), as the slip length of most SHP surfaces deteriorate under increased hydrostatic pressures (208,209, 212, 220). The reason for slip length not declining in a FLISTA design is as follows. Slip length depends on the shear stress and slip velocity on an imaginary plane at the top of the coating (212). At a smaller scale, slip length depend on the drag force acting on the fibers adjacent to water. These fibers are immersed partly in water and partly in the lubricant (n-Hexadecane), and so the total drag force on them consists of the drag force exerted by water and that exerted by the lubricant. As the WLI penetrates deeper into a coating under pressure, the area of these fibers wetted by water increases relative to that wetted by the lubricant. Therefore, the total drag force acting on these fibers decreases with the increase of pressure since the viscosity of water is smaller than that of lubricant (222). As a result, the effective slip length increases with increasing hydrostatic pressure. Figure 6.6a shows contours

of x-velocity in the water and lubricant adjacent to the WLI for a coating with a fiber diameter of $d_f = 20$ μm. It can be seen that slip velocity increases as pressure increases from 10 Pa to 350 Pa (show in red color) which results in an increase in coating's slip length.

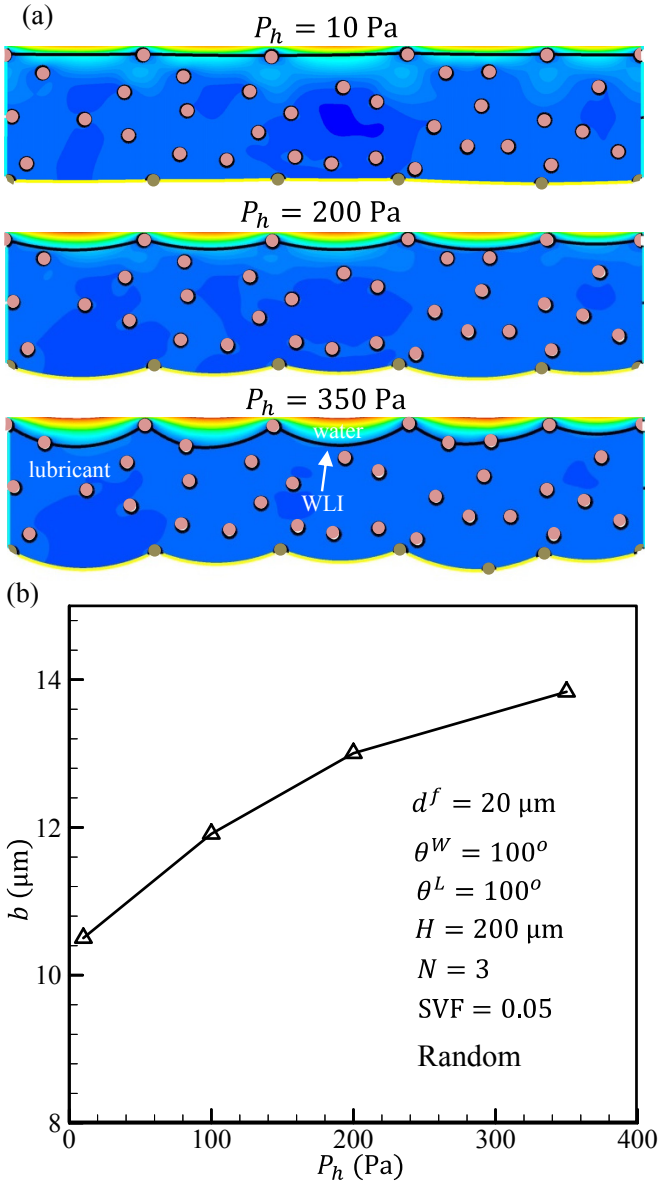

Fig. 6.6: (a) Contours of the x-velocity in the oil domain and in the water domain adjacent to the WLI at different pressures for FLISTA coating with random arrangement of fibers. Blue to red represents the x-velocity from -0.05 mm/s to 1 mm/s. (b) Effects of hydrostatic pressure on slip length for FLISTA coating with random fibers. Here, $U_p = 10$ mm/s, $\theta_W = \theta_L = 100^o$, SVF = 0.05, $N = 3$ and $d_f = 20$ μm.

The main objective of the present work is to investigate the effect of hydrostatic pressure, fiber diameter, fiber spacing, YLCAs of the water and lubricant and viscosity of the lubricant on the drag reduction performance of the FLISTA coating. Although it is more realistic to perform flow simulations for FLISTA coating with random arrangement of fibers, it is more than what is needed. These simulations are also time consuming. This parametric study can also be performed using the FLISTA coating having ordered arrangement of fibers (see Fig. 6.2) with significant savings in CPU time. It is also more convenient to control the fiber spacing for the FLISTA coating with ordered arrangement of fibers. All the results presented in the rest of the chapter are obtained from flow simulations for FLISTA coating having ordered arrangement of fibers.

6.4.1 Effects of Hydrostatic Pressure and Fiber Diameter

A FLISTA coating with an ordered/staggered fiber arrangement is considered in this subsection. Contact angles and solid volume fraction ($\xi = \pi d_f^2 / 2h_L s$) are assumed arbitrarily to be $\theta_W = 100^0$, $\theta_L = 100^0$, and 0.05. Figure 6.7a shows numerical results for coating's effective slip length versus hydrostatic pressures for coatings comprised of fibers with different diameters.

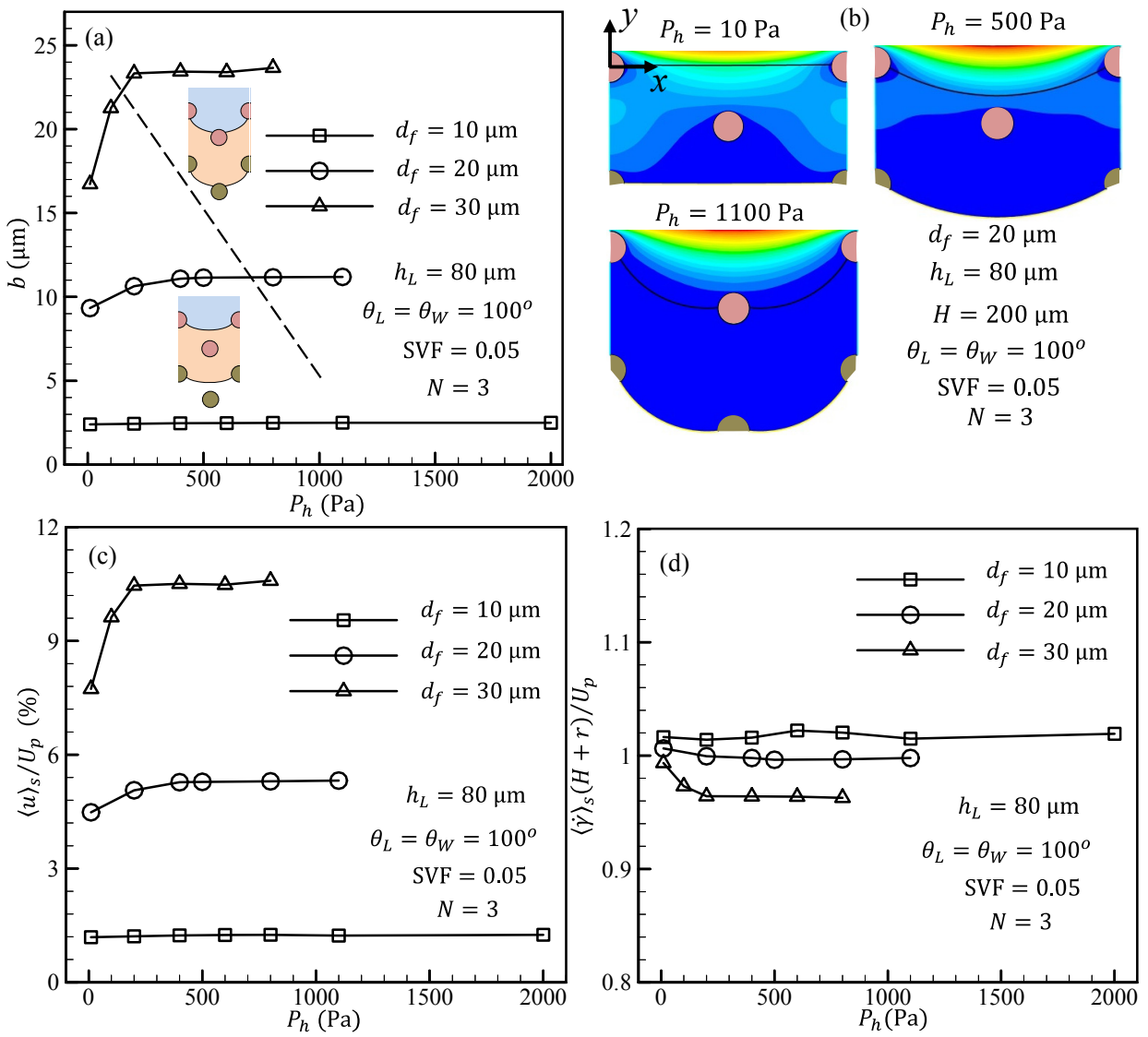

Fig. 6.7: (a) Effect of hydrostatic pressure P_h on slip length for different values of d_f for FLISTA having ordered arrangement of fibers. (b) Contours of the x-velocity in the oil domain and in the water domain adjacent to the WLI. Blue to red represents the x-velocity from -0.03 mm/s to 0.75 mm/s. (c) Effect of P_h on normalized average slip velocity. (d) Effect of P_h on normalized average shear rate. Here, $U_p = 10$ mm/s, $H = 200$ μm, $\theta_W = \theta_L = 100^o$, $h = 80$ μm, $N = 3$ and SVF = 0.05.

It can be seen in Fig. 6.7a that the effective slip length generated by a FLISTA coating having ordered arrangement of fibers increases with increasing hydrostatic pressure up to a point (500 Pa) after which it remains invariant with pressure which is qualitatively similar to the results discussed in the previous section for the FLISTA coating having random arrangement of fibers.

The reason behind the increase of slip length with hydrostatic pressure has already been discussed in the previous section. Note how the WLI penetrates deeper into the coating and comes into contact with the fiber below the first layer as pressure increases (the contact takes place at a hydrostatic pressure of about 700 Pa in the case shown in Figure 6.7b). It is also interesting to note in Figure 6.7a that slip length does not change with pressure for the coating comprised of fibers with a diameter of $d_f = 10$ μm. This is because for the range of hydrostatic pressures given in this figure, WLI profile does not change significantly for the case of $d_f = 10$ μm. Note that fiber–fiber spacing increases with increasing fiber diameter (when SVF is kept constant), and this makes WLI deflection more sensitive to pressure. For instance, the WLI penetrates into the coating deep enough to reach the fibers in the second row at a hydrostatic pressure of 150 Pa when the fiber diameter is 30 μm but the same thing does not happen for pressures less than about 700 Pa if the coating is made of fibers with a diameter of $d_f = 20$ μm. For the same exact reason, slip length increases with the increasing fibers diameter (for a fixed SVF) as can be seen in Figure 6.7a. This can be explained with the help of average slip velocity $\langle u \rangle_s$ and average of the shear rate $\langle \dot{\gamma} \rangle_s$ at the aforementioned imaginary plane right above the top surface of the coating, i.e.,

$$\langle u \rangle_s = \frac{1}{L} \int u(x, y = r) dx \tag{6.13}$$

$$\langle \dot{\gamma} \rangle_s = \left. \frac{d \langle u \rangle}{dy} \right|_{y=r} \tag{6.14}$$

As can be seen in Figures 6.7c-6.7d, average slip velocity is higher and average shear rate is lower for coatings made of larger fibers (having an identical SVF).

6.4.2 Effects of Fiber Spacing and Lubricant Layer Thickness

In this section, we consider FLISTA coatings having a fiber diameter of $d_f = 20$ μm and contact angles of $\theta_L = \theta_W = 100^o$ but with different fiber spacing values to study how horizontal fiber–fiber spacing affects slip length. We also consider two different hydrostatic pressures of $P_h = 10$ Pa and $P_h = 1100$ Pa, in a unit cell with a width of $h = 80$ μm.

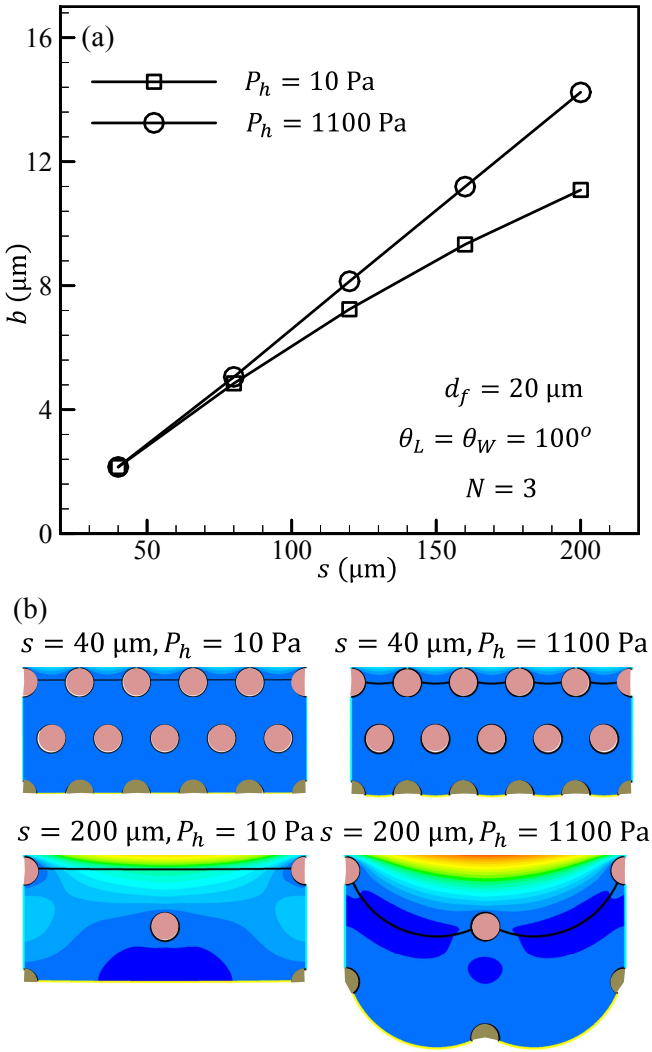

Fig. 6.8: (a) Effect of s on slip length for FLISTA having ordered arrangement of fibers. (b) Contours of the x-velocity in the oil domain and in the water domain adjacent to the WLI. Blue to red represents the x-velocity from -0.06 mm/s to 1 mm/s. Here, $U_p = 10$ mm/s, $H = 200$ μm, $\theta_W = \theta_L = 100^o$, $h = 80$ μm, $d_f = 20$ μm and $N = 3$.

As can be seen in Figure 6.8a, slip length increases monotonically with increasing horizontal fiber spacing. This is because increasing the horizontal fiber–fiber spacing increases the porosity of the coating and so decreases the contact between the working fluid and the frictional solid surfaces (fibers). This effect is shown graphically in Figure 6.8b using velocity contour plots for two different fiber–fiber spacing and under two different pressures. Note also that, WLI penetrates deeper into the coating when horizontal fiber-fiber spacing is increased. This increases the fraction of the fibers' surface in contact with water (less viscous) relative to the fraction in contact with lubricant (more viscous), and thereby reduces the overall friction between the fibers and the fluids involved.

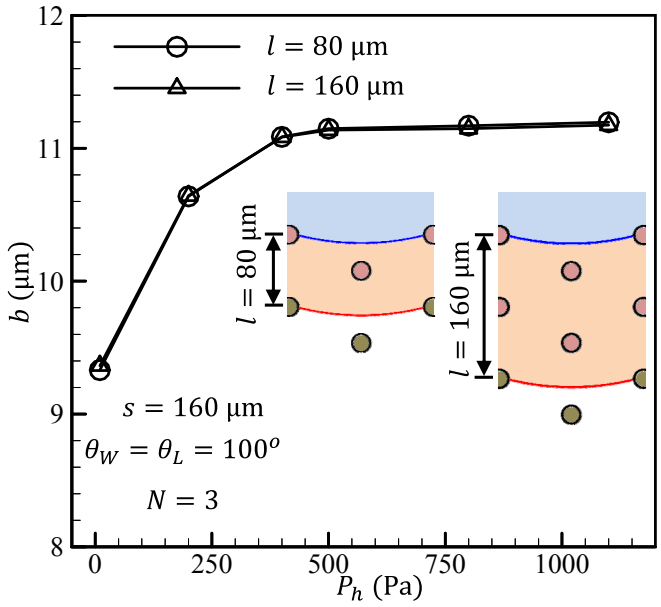

Fig. 6.9: Effect of lubricant layer thickness l on slip length for FLISTA having ordered arrangement of fibers. Here, $U_p = 10$ mm/s, $H = 200$ μm, $\theta_W = \theta_L = 100^o$, $h = 80$ μm, $s = 160$ μm, $N = 3$ and $d_f = 20$ μm.

Figure 6.9 compares the performance of two coatings with different lubricant-layer thicknesses (but identical properties otherwise) under different hydrostatic pressures. It

can be seen that for the range of parameters considered, thickness of the lubricant layer has no measurable effect on slip length. Note that these results are obtained for a steady-state shear flow with the upper wall moving with a constant speed. For such a flow condition, the velocity field in the water phase will not strongly depend on the thickness of the lubricant pool (although the time needed to reach a steady-state condition does). This is because velocities deep in the lubricant layer become quite small relative to those near the WLI. Also note that increasing the thickness of the lubricant layer does not affect the shape or position of the WLI as can be seen in the inset figures in Figure 6.9.

6.4.3 Effects of Water and Lubricant YLCAs

In all the cases discussed in the previous subsections it was assumed that YLCAs θ_W and θ_L were equal. But in reality their values can be different from each other. The contact angle of a lubricant in a solid-water-lubricant system is different from the contact angle of the same lubricant in a solid-air-lubricant system (223, 224). In this subsection, we consider different combinations of θ_W and θ_L values to study their effects on the slip length for FLISTA coating. It can be observed in Fig. 6.10a that slip length does not change with θ_L when θ_W is kept constant. On the contrary, the effective slip length increases with the decrease of θ_W. The WLI penetrates into the coating with the decrease of θ_W. Therefore, the area of the top layer of fibers wetted by water increases whiles the area of the fibers in this layer wetted by high viscous lubricant decreases. The total drag force on the top layer of fibers decreases and slip velocity increases (see Fig. 6.10b) with the decrease of θ_W which results in increase in slip length. The areas of the top layer of fibers wetted by water and lubricant do not change with the change of θ_L. Thus, the slip

velocity as well as slip length do not change with the change of θ_L. θ_L only affects the stability of the lubricant layer.

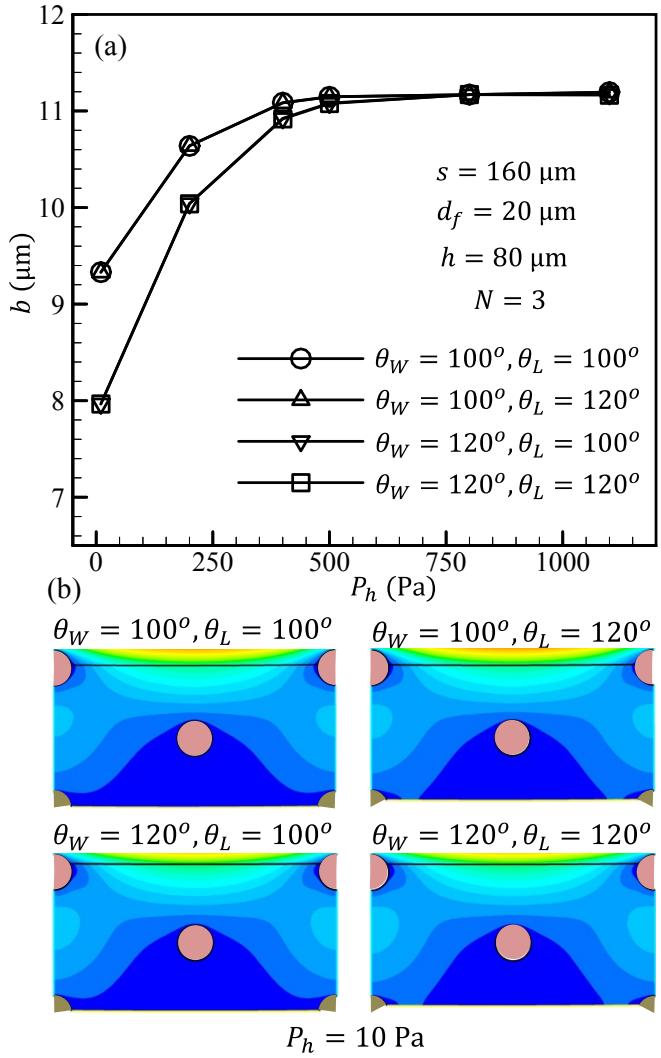

Fig. 6.10: Effects of θ_W and θ_L on slip length for FLISTA having ordered arrangement of fibers. (b) Contours of the x-velocity in the oil domain and in the water domain adjacent to the WLI at $P_h = 10$ Pa. Blue to red represents the x-velocity from -0.03 mm/s to 0.75 mm/s. Here, $U_p = 10$ m/s, $H = 200$ μm, $h = 80$ μm, $s = 160$ μm, $N = 3$ and $d_f = 20$ μm.

6.4.4 Effects of Gap Height

It is expected that slip length will depend on the gap height H. The shear rate in the gap depends on the gap height H. We compute slip length for three different values of H to

study its effect on slip length and present the results in Fig. 6.11. It is observed that the slip length increases when H is increased from $50\ \mu m$ to $200\ \mu m$. It is because higher H is associated with lower shear rate. However almost no change in slip length is observed when H is increased from $200\ \mu m$ to $1000\ \mu m$. It seems slip length becomes independent of shear rate when the shear rate becomes smaller than a threshold value. Similar observation on the dependence of slip length on the gap height H for superhydrophobic surfaces was previously made by Vidal and Botto (207).

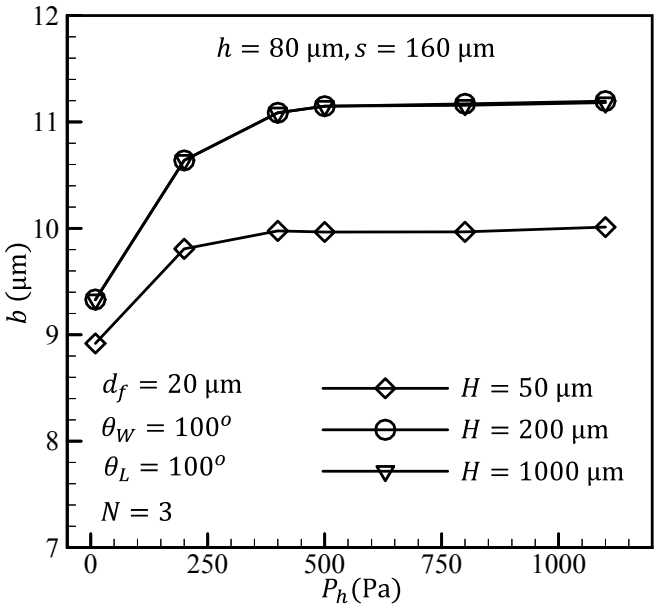

Fig. 6.11: Effects of gap height H on slip length for FLISTA coating having staggered arrangement of fibers. Here, $U_p = 10$ m/s, $\theta_W = \theta_L = 100^o$, $h = 80\ \mu m$, $s = 160\ \mu m$, $N = 3$ and $d_f = 20\ \mu m$.

6.4.5 Effects of Lubricant Viscosity

Drag force on the fibers of the coating and slip length depend on the viscosity of the lubricant. We compute the slip length for flow over FLISTA coating for two different lubricant viscosities and present the results in Fig. 6.12a. It shows that slip length decreases with the increase of lubricant viscosity. Although the area of the part of the top

layer of fibers wetted by the lubricant does not change with the change of lubricant viscosity, the drag force on this part increases with the increase of lubricant viscosity which results in increase in the total drag force on the top layer of fibers. Figure 6.12b shows that slip velocity increases with the decrease of lubricant viscosity at $P_h = 10$ Pa. As a result slip length increases with the decrease of lubricant viscosity.

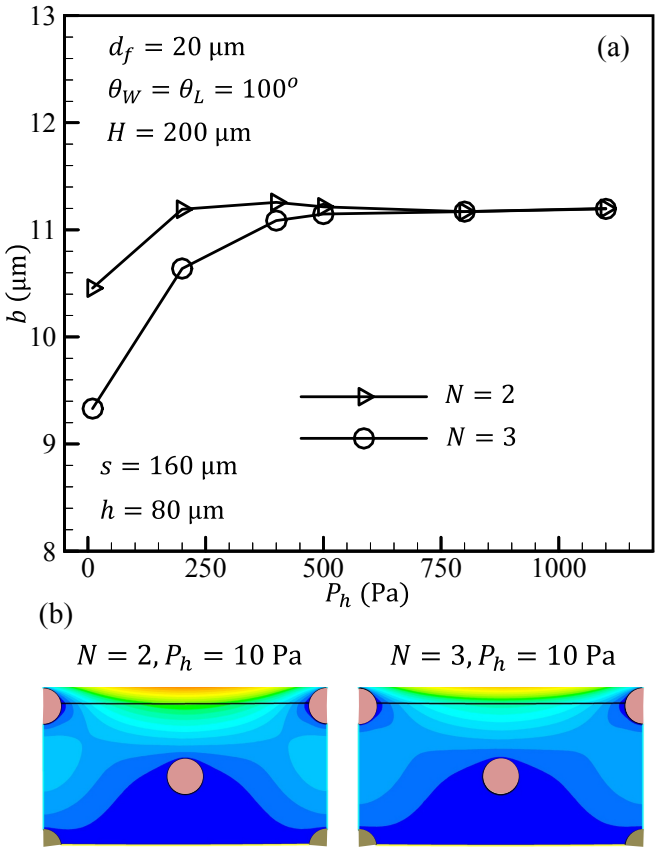

Fig. 6.12: (a) Effects of lubricant viscosity μ_L on slip length for FLISTA having staggered arrangement of fibers. (b) Contours of the x-velocity in the oil domain and in the water domain adjacent to the WLI at $P_h = 10$ Pa. Blue to red represents the x-velocity from -0.025 mm/s to 0.8 m/s. Here, $U_p = 10$ mm/s, $\theta_W = \theta_L = 100^o$, $h = 80$ μm, $s = 160$ μm and $d_f = 20$ μm.

6.5 Conclusions

Drag reduction performance of FLISTA coating and the effects of different parameters (pressure, lubricant property, fiber diameter, fiber spacing, fiber arrangement) on the drag

reduction performance of the coating have been presented in this paper. It is found that slip length for FLISTA coating increases with the increase of hydrostatic pressure unlike superhydrophobic surfaces and this is a major advantage of the FLISTA coating. This is true for both the FLISTA coatings having ordered and random arrangement of fibers. Slip length mainly depends on the fiber diameter, fiber spacing at the top layer of fibers, θ_W, μ_L and gap height at smaller gap height for FLISTA. It strongly depends on the arrangement of the top layer of the fibers. Slip length does not change with the change of thickness of the lubricant layer and θ_L. θ_L only affects the stability of the lubricant layer.

Chapter 7. Overall Conclusion

A series of investigations on the droplet-fiber interactions has been presented in this thesis. Experiments and numerical simulations were devised to find the effects of fiber properties (diameter and YLCA) and liquid properties on the interaction of a liquid droplet with a single fiber and a system of multiple fibers. Our work on droplet interaction with a fiber was focused on the detachment time and the droplet residue left on the fiber after droplet detachment. It was found that residue volume decreases with increasing fiber YLCA or droplet viscosity (in a viscosity range of 1–5.5 mPa s). Moreover, residue volume was found to increase with increasing fiber diameter (for a fixed YLCA) but remained almost independent of droplet volume. Droplet detachment time was found to increase with droplet volume or fiber diameter but remained unaffected by increasing droplet viscosity in 1–5.5 mPa s range. Detachment time was also found to decrease with increasing YLCA of the fiber. Then we investigated the droplet/liquid bridge between two fibers in parallel and orthogonal configurations. Our experiments and numerical simulations show that the shape of the liquid bridge and its interactions with the fibers vary significantly with varying the spacing between the fibers. It was found that the fiber-fiber spacing corresponding to bridge detachment, detachment force and destination of the droplet resulted from the bridge detachment was independent of the relative angle between the fibers. It was also shown that the liquid bridge detaches from the fiber that provided a weaker capillary force (after factoring the weight of the liquid), and the force needed for detachment did not strongly depend on the size or the YLCA of the other fiber (as long as it provided a larger capillary force, of course). A mathematical criterion was developed to predict which of the two fibers accommodating a liquid bridge would take the droplet that was resulted

from the bridge detachment. We also investigated the wetting behavior of a droplet deposited on a fibrous coating. The numerical simulations conducted in this work indicate that apparent contact angles of a droplet can be increased by decreasing the diameter of the fibers in the coating for a given fiber spacing (fiber count per unit length). Similarly, it was shown that increasing the fiber spacing, up to a critical value, can also help to increase the contact angles on a coating with a given fiber diameter. However, droplet contact angle can exhibit considerable fluctuations with varying fiber spacing. Considerable differences was observed between droplet contact angles on orthogonally layered and parallel-fiber coatings, i.e., a droplet may achieve higher contact angles on a coating with orthogonal fibers. Analytical expressions are derived to predict the condition in which a droplet may depart from the non-wetting Cassie state by partially or completely wetting the coating below it.

Regarding drag reduction performance of granular and fibrous coatings, we first performed numerical simulations to investigate the drag reduction due to superhydrophobic granular coatings. With all other parameters kept constant, better drag reduction results were obtained for coatings with lower SVF, higher YLCAs or larger particles. It was also found that the drag reduction performance of submerged SHP coatings decreased with increasing hydrostatic pressure. However, under suction pressure (e.g., the Venturi effect) the drag reduction efficiency of a granular coating seems to increase monotonically with decreasing pressure, in contrast to coatings comprised of sharp-edged pores. At the end, the drag reducing performance of fibrous liquid infused surface with trapped air (FLISTA) made of layers of parallel fibers was investigated. The results from our numerical simulations show that drag reduction performance of FLISTA increases with increasing hydrostatic pressure up to a point after which it remains

invariant with pressure unlike the case of conventional superhydrophobic surfaces. It also increases with the decreasing SVF or increasing fiber diameter with all other parameters kept constant. However, it decreases with the increasing lubricant viscosity.

Chapter 8. References

1. Seo D, Lee J, Lee C, Nam Y. The effect of surface wettability on the fog and dew moisture harvesting performance on tubular surfaces. Sci Rep. 2016;6:24276.

2. Shi W, Anderson MJ, Tulkoff JB, Kennedy BS, Boreyko JB. Fog harvesting with harps. ACS Applied Mater Interfaces. 2018;10(14):11979 – 11986.

3. Kampa D, Wurster S, Buzengeizer J, Meyer J, Kasper G. Pressure drop and liquid transport through coalescence filter media used for oil mist filtration. Int J Multiph Flow. 2014;58: 313 – 324.

4. Muller TK, Meyer J, Thebault E, Kasper G. Impact of an oil coating on particle deposition and dust holding capacity of fibrous filters. Powder Technol. 2014;253: 247 – 255.

5. Guo F, Servi F, Liu A, Gleason KK, Rutledge GC. Desalination by membrane distillation using electrospun polyamide fiber membranes with surface fluorination by chemical vapor deposition. ACS Appl. Mater. Interfaces. 2015;7:8225 – 8232.

6. Liao Y, Loh C-H, Wang R, Fane AG. Electrospun superhydrophobic membranes with unique structures for membrane distillation. ACS Appl. Mater. Interfaces. 2014;6:16035 – 16048.

7. Jamali M, Moghadam A, Tafreshi HV, Pourdeyhimi B. Droplet adhesion to hydrophobic fibrous surfaces. Applied Surface Science. 2018;456:626 – 636.

8. Michielsen S, Lee HJ. Design of superhydrophobic surface using woven structures. Langmuir. 2007;23:6004 – 6010.

9. Chen D, Tan L, Liu H, Hu J, Li Y, Tang F. Fabricating superhydrophilic wool fabrics. Langmuir. 2010;26(7):4675 – 4679.

10. Contal P, Simao J, Thomas D, Frishing T, Calle S, Appert-Collin JC, Bremer D. Clogging of fibre filters by submicron droplets. Phenomena and influence of operating contributions. J. Aerosol Sci. 2004;35:263 – 278.

11. Patel SU, Chase GG. Separation of water droplets from water-in-diesel dispersion using superhydrophobic polypropylene fibrous membranes. Sep. Purif. Technol. 2014;126:62 – 68.

12. Gilet T, Terwagne D, Vandewalle N. Digital microfluidics on a wire. Appl. Phys. Lett. 2009;95:014106.

13. Reznik SN, Salalha W, Yarin AL, Zussman E. Microscale fibre alignment by a three dimensional sessile drop on a wettable pad. J. Fluid Mech. 2007;574:179 – 207.

14. Semprebon C, Brinkmann M. On the onset of motion of sliding drops. Soft Matter. 2014;10(18):3325– 34.

15. Allen RF, Benson PR. Rolling drops on an inclined plane. J Colloid Interface Sci. 1975;50(2):250–3.

16. Mahadevan L, Pomeau Y. Rolling droplets. Phys Fluids. 1999;11(9):2449.

17. Ding H, Gilani MNH, Spelt PDM. Sliding, pinch-off and detachment of a droplet on a wall in shear flow. J. Fluid Mech. 2010;644:217-244.

18. Young T. An essay on the cohesion of fluids. Philos. Trans. R. Soc. Lond. 1805;95:65 – 87.

19. Tsamopoulos JA, Poslinski AJ, Ryan ME. Equilibrium shapes and stability of captive annular menisci. J. Fluid Mech. 1988;197:523 – 549.

20. Lobaton EJ, Salamon TR. Computation of constant mean curvature surfaces: Application to the gas-liquid interface of a pressurized fluid on a superhydrophobic surface. J. Colloid Interface Sci. 2007;314(1):184 – 198.

21. Brown RA, Scriven LE. On the multiple equilibrium shapes and stability of an interface pinned on a slot. J. Colloid Interface Sci. 1980;78(2):528 – 542.

22. Emami B, Tafreshi HV, Gad-el-Hak M, Tepper GC. Predicting shape and stability of air-water interfaces on superhydrophobic surfaces with randomly distributed dissimilar posts. Appl. Phys. Lett. 2011;98:203106.

23. Ershov D, Sprakel J, Appel J, Stuart MAC, van der Gucht J. Capillarity induced ordering of spherical colloids on an interface with anisotropic curvature. PNAS. 2013;110(23):9220 – 9224.

24. Carroll BJ. Equilibrium conformations of liquid drops on thin cylinders under forces of capillarity. A theory for the roll-up process. Langmuir. 1986;2:248 – 250.

25. Carroll BJ. The accurate measurement of contact angle, phase contact areas, drop volume and Laplace excess pressure in drop-on-fiber systems. J. Colloid Interface Sci. 1976;57: 488 – 495.

26. McHale G, Newton MI. Global geometry and equilibrium shapes of liquid drops on fibers. Colloids Surf. A 2002;206: 79 – 86.

27. Rebouillat S, Letellier B, Steffenino B. Wettability of single fibers - beyond the single fibers beyond the contact angle approach. Int. J. Adhes. Adhes. 1999;19: 303 – 314.

28. De Ruiter R, de Ruiter J, Eral HB, Samprebon C, Brinkman M, Mugele F. Buoyant droplets on functional fibers. Langmuir 2012;28: 13300 – 13306.

29. Mei M, Fan J, Shou D. The gravitational effect on the geometric profiles of droplets on horizontal fibers. Soft matter 2013;9: 10324 – 10334.

30. Sahu RP, Sinha-Ray S, Yarin AL, Pourdeyhimi B. Blowing drops off a filament. Soft Matter 2013;9: 6053−6071.

31. Yarin AL, Liu W, Reneker DH. Motion of droplets along thin fibers with temperature gradient. J. Appl. Phys. 2002;91: 4751 – 4760.

32. Dawar S, Li H, Dobson J, Chase GG. Drag correlation of drop motion on fibers. Drying Technol. 2006;24: 1283 – 1288.

33. Gilet T, Terwagne D, Vandewalle N. Droplets sliding on fibers. Eur. Phys. J. E: Soft Matter Biol. Phys. 2010;31: 253 – 262.

34. Haefner S, Baumchen O, Jacobs K. Capillary droplet propulsion on a fibre. Soft Matter 2015;11: 6921 – 6926.

35. Mead-Hunter R, Mullins BJ, Becker T, Braddock RD. Evaluation of the force required to move a coalesced liquid droplet along a fiber. Langmuir 2011;27: 227 – 232.

36. Mullins BJ, Pfrang A, Braddock RD, Schimmel T, Kasper G. Detachment of liquid droplets from fibers – Experimental and theoretical evaluation of detachment force due to interfacial tension effects. Journal of Colloid and Interface Science. 2007;312: 333 – 340.

37. Lorenceau E, Clanet C, Quéré D. Capturing drops with a thin fiber. J. Colloid Interface Sci. 2004;279: 192−197.

38. Amrei MM, Venkateshan DG, D'Souza N, Atulasimha J, Tafreshi HV. Novel approach to measuring the droplet detachment force from Fibers. Langmuir. 2016;32:13333 – 13339.

39. Amrei MM, Davoudi M, Chase GG, Tafreshi HV. Effects of roughness on droplet apparent contact angles on a fiber. Separation and Purification Technology 2017;180:107 – 113.

40. Pan Z, Weyer F, Pitt WG, Vandewalle N, Truscott TT. Drop on bent fibre. Soft Matter. 2018;14:3724.

41. Sauret A, Bick AD, Duprat C, Stone HA. Wetting of crossed fibers: Multiple steady states and symmetry breaking. EPL. 2014;105: 56006.

42. Weyer F, Lismont M, Dreesen L, Nestler B, Vandewalle N. Compound droplet manipulations on fiber arrays. Soft Matter. 2015;11: 7086−7091.

43. Weyer F, Duchesne A, Vandewalle N. Switching behavior of droplets crossing nodes on a fiber network. Scientific Reports. 2017;7:13309.

44. Davoudi M, Fang J, Chase GG. Barrel shaped droplet movement at junctions of perpendicular fibers with different orientations to the air flow direction. Separation and Purification Technology 2016;162:1−5.

45. Bormashenko E. Progress in understanding wetting transitions on rough surfaces. Advances in colloid and interface science. 2015;222:92–103.

46. Eick JD, Good RJ, Neumann AW. Thermodynamics of contact angles. 2. Rough solid-surfaces. J. Colloid Interface Sci. 1975;53:235–248.

47. He B, Patankar NA, Lee J. Multiple equilibrium droplet shapes and design criterion for rough hydrophobic surfaces. Langmuir. 2003;19:4999–5003.

48. Long J, Hyder MN, Huang RYM, Chen P. Thermodynamic modeling of contact angles on rough, heterogeneous surfaces. Adv. Colloid Interface Sci. 2005;118:173–190.

49. Wenzel RN. Resistance of solid surfaces to wetting by water. Ind. Eng. Chem. 1936;28:988–994.

50. Cassie ABD, Baxter S. Wettability of porous surfaces. Trans. Faraday Soc. 1944;40:0546–0550.

51. Marmur A. Wetting on the hydrophobic rough surfaces: To be heterogeneous or not to be?. Langmuir. 2003;19:8343 – 8348.

52. Bormashenko E, Bormashenko Y, Stein T, Whyman G, Bormashenko E. Why do pigeon feathers repel water? Hydrophobicity of pennae, Cassie-Baxter wetting hypothesis and Cassie-Wenzel capillarity-induced wetting transition. J. Colloid Interface Sci. 2007;311:212–216.

53. Quere D. Wetting and roughness. Annu. Rev. Mater. Res. 2008;38:71–99.

54. Shirtcliffe NJ, McHale G, Atherton S, Newton MI. An introduction to superhydrophobicity. Adv. Colloid Interf. Sci. 2010;16:124–138.

55. Rothstein JP. Slip on superhydrophobic surfaces. Annu. Rev. Fluid Mech. 2010;42:89–109.

56. Lee C, Choi C-H, Kim C-J, Structured surfaces for giant liquid slip. Phys. Rev. Lett. 2008;101:064501.

57. Extrand CW. Repellency of the lotus leaf: resistance to water intrusion under hydrostatic pressure. Langmuir. 2011;27:6920–6925.

58. Ma ML, Hill RM, Rutledge GC. A review of recent results on superhydrophobic materials based on micro- and nanofibers. J. Adhes. Sci. Technol. 2008;22:1799.

59. Tuteja A, Choi W, Mabry JM, McKinely GH, Cohen RE. Robust omniphobic surfaces. Proc. Natl. Acad. Sci. U.S.A. 2008;105:18200.

60. Wu H, Zhang R, Sun Y, Lin D, Sun Z, Pan W, Downs P, Biomimetic nanofiber patterns with controlled wettability. Soft Matter. 2008;4:2429–2433.

61. Lin J, Cai Y, Wang X, Ding B, Yu J, Wang M, Fabrication of biomimetic superhydrophobic surfaces inspired by lotus leaf and silver ragwort leaf. Nanoscale. 2011;3:1258.

62. Lim HS, Park SH, Koo SH, Kwark Y-J, Thomas EL, Jeong Y, Cho JH. Superamphiphilic Janus Fabric. Langmuir. 2010;26(24):19159–19162.

63. Brandon S, Wachs A, Marmur A, Simulated contact angle hysteresis of a three-dimensional drop on a chemically heterogeneous surface: a numerical example. J. Colloid Interface Sci. 1997;191:110–116.

64. Brandon S, Haimovich N, Yeger E, Marmur A. Partial wetting of chemically patterned surfaces: The effect of drop size. J. Colloid Interface Sci. 2003;263:237–243.

65. Chen Y, He B, Lee J, Patankar NA. Anisotropy in the wetting of rough surfaces. J. Colloid interface sci. 2004;281:458–464.

66. Li W, Fang GP, Lij YF, Qiao GJ. Anisotropic wetting behavior arising from superhydrophobic surfaces: parallel grooved structure. J. Phys. Chem. B. 2008;112:7234–7243.

67. Dubov AL, Mourran A, Moller M, Vinogradova OI. Contact angle hysteresis on superhydrophobic stripes. Journal of Chemical Physics. 2014;141:074710.

68. Jansen HP, Sotthewes K, Zandvliet HJW, Kooij ES. Potential of lattice Boltzmann to model droplets on chemically stripe-patterned substrates. Applied Surface Science. 2016;361:122–132.

69. Tie L, Guo Z, Liu W. Anisotropic wetting properties on various shape of parallel grooved microstructure. J. Colloid Interface Sci. 2015;453:142–150.

70. Bormashenko E, Gendelman O, Whyman G. Superhydrophobicity of lotus leaves versus birds' wings: Different physical mechanisms leading to similar phenomena. Langmuir. 2012;28:14992 – 14997.

71. Zhao H, Law KW. Directional self-cleaning of superoleophobic surface. Langmuir. 2012;28:11812–11818.

72. Wu SZ, Wang JN, Niu GL, Yao J, Wu D, Li AW. Reversible switching between isotropic and anisotropic wetting by one-direction curvature tuning on flexible superhydrophobic surfaces. Applied Physics Letters. 2011;98:081902.

73. Zussman E, Theron A, Yarin AL, Formation of nanofiber crossbars in electrospinning. Appl. Phys. Lett. 2003;82:6.

74. Brown TD, Dalton PD, Hutmacher DW. Direct Writing By Way of Melt Electrospinning, Adv. Mater. 2011;23:5651–5657.

75. Bucher TM, Emami B, Tafreshi HV, Gad-el-Hak M, Tepper GC. Modeling resistance of nanofibrous superhydrophobic coatings to hydrostatic pressures: The role of microstructure. Physics of Fluids. 2012;24:022109.

76. Dalton PD, Vaquette C, Farrugia BL, Dargaville TR, Brown TD, Hutmacher DW. Electrospinning and additive manufacturing: converging technologies. Biomater. Sci. 2013;1:171–185.

77. Bucher TM, Tafreshi HV, Tepper GC. Modeling Filtraion Performance of Nanofiber Coatings with Orthogonal Fiber Orientations. Powder Technology. 2013;249:43-53.

78. Bucher TM, Amrei MM, Tafreshi HV. Wetting resistance of heterogeneous superhydrophobic coatings with orthogonally layered fibers. Surface & Coatings Technology. 2015;277:117–127.

79. Ou J, Rothstein P. Direct velocity measurements of the flow past drag-reducing ultrahydrophobic surfaces. Phys. Fluids. 2005;17:103606.

80. McHale G, Shirtcliffe NJ, Evans CR, Newton MI. Terminal velocity and dragreduction measurements on superhydrophobic spheres. Appl. Phys. Lett. 2009;94:064104.

81. Samaha MA, Tafreshi HV, Gad-el-Hak M. Modeling drag reduction and meniscus stability of superhydrophobic surfaces comprised of random roughness. Phys. Fluids. 2011;23:012001.

82. Dong H, Cheng M, Zhang Y, Wei H, Shi F. Extraordinary drag-reducing effect of a superhydrophobic coating on a macroscopic model ship at high speed. J.Mater. Chem. A. 2013;1:5886–5891.

83. Brown PS, Bhushan B. Mechanically durable, superoleophobic coatings prepared by layer-by- layer technique for anti-smudge and oil-water separation. Scientific Reports. 2014;5:8701.

84. Shirtcliffe NJ, McHale G, Newton MI, Chabrol G, Perry CC. Dual-scaleroughness produces unusually water-repellent surfaces. Adv. Mater. 2004;16:1929–1932.

85. Ma ML, Hill RM, Rutledge GC. A review of recent results on superhydrophobic materials based on micro- and nanofibers. J. Adhes. Sci. Technol. 2008;22:1799.

86. Emami B, Tafreshi HV, Gad-el-Hak M, Tepper GC. Effect of fiber orientation on shape and stability of air–water interface on submerged superhydrophobic electrospun thin coatings. Journal of Applied Physics. 2012;111:064325.

87. Emami B, Tafreshi HV, Gad-el-Hak M, Tepper GC. Simulation of meniscus stability in superhydrophobic granular surfaces under hydrostatic pressures. Colloid Surf. A. 2011;385:95–103.

88. Samaha MA, Ochanda F, Tafreshi HV, Tepper GC, Gad-el-Hak M. In-situ non-invasive characterization of superhydrophobic coatings. Rev. Sci. Instrum. 2011;82:045109.

89. Samaha MA, Tafershi HV, Gad-el-Hak M. Effects of hydrostatic pressures on drag-reduction performance of submerged aerogel particle coatings. Colloid Surf. A. 2012;399:62–70.

90. Amrei MM, Tafreshi HV. Effects of hydrostatic pressure on wetted area of submerged superhydrophobic granular coatings. Part 1: mono-dispersed coatings. Colloids and Surfaces A: Physicochem. Eng. Aspects. 2015;465:87-98.

91. Amrei MM, Tafreshi HV. Effects of pressure on wetted area of submerged superhydrophobic granular coatings. Part II: poly-dispersed coatings, Colloids and Surfaces A: Physicochem. Eng. Aspects. 2015;481:547-560.

92. Steinberger A, Cottin-Bizonne C, Kleimann P, Charlaix E. High friction on a bubble mattress. Nat Mater. 2007;6(9):665-668.

93. Karatay E, Haase AS, Visser CW, Sun C, Lohse D, Tsai PA, Lammertink RGH. Control of slippage with tunable bubble mattresses. Proc. Natl. Acad. Sci. U. S. A. 2013;110:8422-8426.

94. Bobji MS, Kumar SV, Asthana A, Govardhan RN. Underwater sustainability of the Cassie state of wetting. Langmuir. 2009;25;12120 – 12126.

95. Emami B, Hemeda AA, Amrei MM, Luzar A, Gad-el-Hak M, Tafreshi HV. Predicting longevity of submerged superhydrophobic surfaces: surfaces with parallel grooves. Phys. Fluids. 2013;25:062108.

96. Samaha MA, Tafreshi HV, Gad-el-Hak M. Sustainability of superhydrophobicity under pressure. Phys. Fluids. 2012;24:112103.

97. Lv P, Xue Y, Shi Y, Lin H, Duan H. Metastable states and wetting transition of submerged superhydrophobic structures. Phys. Rev. Lett. 2014;112:196101.

98. Hemeda AA, Tafreshi HV. General formulations for predicting longevity of submerged superhydrophobic surfaces composed of pores or posts. Langmuir. 2014;30:10317 – 10327.

99. Xu M, Sun G, Kim C-J. Infinite lifetime of underwater superhydrophobic states. Phys. Rev. Lett. 2014;113:136103.

100. Bolognesi G, Cottin-Bizonne C, Pirat C. Evidence of slippage breakdown for a superhydrophobic microchannel. Phys. Fluids. 2014;26:082004.

101. Wong T-S, Kang S-H, Tang SKY, Smythe EJ, Hatton BD, Grinthal A, Aizenberg J. Bioinspired self-repairing slippery surfaces with pressure-stable omniphobicity. Nature. 2011;477:443 – 447.

102. Solomon BR, Khalil KS, Varanasi KK. Drag reduction using lubricant-impregnated surfaces in viscous laminar flow. Langmuir. 2014;30:10970 – 10976.

103. Hemeda AA, Tafreshi HV. Liquid-infused surfaces with trapped air (LISTA) for drag force reduction. Langmuir. 2016;32:2955 – 2962.

104. Waxler JS, Jacobi I, StoneH. Shera-driven failure of liquid-infused surfaces. Phys. Rev. Lett. 2015;114:168301.

105. Waxler JS, Grosskopf A, Chow M, Fan Y, Jacobi I, Stone HA. Robust liquid-infused surfaces through patterned wettability. Soft Matter 2015;11:5023.

106. Jacobi I, Waxler JS, Samaha MA, Shang JK, Rosenberg BJ, Hultmark M, Stone HA. Stratified thin-flim flow in a rheometer. Phys. Fluids. 2015;27:052102.

107. Smith JD, Dhiman R, Anand S, Reza-Garduno E, Cohen RE, Mckinley GH, Varanasi KK. Droplet mobility on lubricant-impregnated surface. Soft Matter. 2013;9:1772.

108. Wurster S, Meyer J, Kolb HE, Kasper G. Bubbling vs. blow-off – On the relevant mechanism(s) of drop entrainment from oil mist filter media. Separation and Purification Technology. 2015;152: 70–79.

109. Wei X, Chen F, Wang H, Zhou H, Ji Z, Lin T. Efficient removal of aerosol oil-mists using superoleophobic filters. J. Mater. Chem. A. 2018;6: 871–877.

110. Contal P, Simao J, Thomas D, Frising T, Calle S, Appert-Collin JC, Bremer D. Clogging of fibre filters by submicron droplets. Phenomena and influence of operating conditions. J. Aerosol Sci. 2004;35: 263 – 278.

111. Rajgarhia SS, Jana SC, Chase GG. Separation of water from ultralow Sulphur diesel using novel polymer nanofiber-coated glass fiber media. ACS Appl. Mater. Interfaces 2016;8:21683 – 21690.

112. Reznik SN, Salalha W, Yarin AL, Zussman E. Microscale fibre alignment by a three-dimensional sessile drop on a wettable pad. J. Fluid Mech. 2007;574:179 – 207.

113. Gauthier E, Hellstern T, Kevrekidis IG, Benziger J. Drop detachment and motion on fuel cell electrode materials. ACS Appl. Mater. Interfaces 2012;4: 761 – 771.

114. Gurau V, Bluemle MJ, Castro ESD, Tsou YM, Man Jr. JA, Zawodzinski Jr. TA. Characterization of transport properties in gas diffusion layers for proton exchange membrane fuel cells: 1. Wettability (internal contact angle to water and surface energy of GDL fibers). Journal of Power Sources. 2006;160(2): 1156 – 1162.

115. Tadmor R, Das R, Gulec S, Liu J, N'guessan HE, Shah M, Wasnik PS, Yadav SB. Solid-liquid work of adhesion. Langmuir. 2017;33(15):3594 – 3600.

116. Solmaz M, Park H, Madsen CK, Cheng X. Patterning chalcogenide glass by direct resist-free thermal nanoimprint. J. Vac. Sci. Technol. B. 2008;26: 606–610.

117. Lin PC, Yang S. Mechanically switchable wetting on wrinkled elastomers with dual-scale roughness. Soft Matter. 2009;5:1011 – 1018.

118. Brakke KA. The Surface Evolver. Exp. Math. 1992;1: 141 – 165.

119. Yildirim OE, Xu Q, Basaran OA. Analysis of drop weight method. Physics of Fluids 2005;17:062107.

120. Dressaire E, Sauret A, Boulogne F, Stone HA. Drop impact on a flexible fiber. Soft Matter 2016;12:200.

121. Comtet J, Keshavarz B, Bush JWM. Drop impact and capture on a thin flexible fiber. Soft Matter 2016;12:149.

122. Ambravaneswaran B, Wilkes ED, Basaran OA. Drop formation from a capillary tube: Comparison of one-dimensional and two-dimensional analyses and occurrence of satellite drops. Physics of Fluids. 2002;14:2606.

123. Hanna G, Barnes WJP. Adhesion and detachment of the toe pads of the tree frogs. J. Exp. Biol. 1991;155:103 – 125.

124. Qian J, Gao H. Scaling effects of wet adhesion in biological attachment systems. Acta Biomaterialia. 2006;2:51 – 58.

125. Huber G, Mantz H, Spolenak R, Mecke K, Jacobs K, Gorb SN, Arzt E. Evidence of capillarity contributions to gecko adhesion from single spatula nanomechanical measurements. PNAS. 2005;102(45):16293 – 16296.

126. Eisner T, Aneshansley DJ. Defense by foot adhesion in a beetle (Hemisphaerota cyanea). PNAS. 2000;97(12):6568 – 6573.

127. Dejam M, Hassanzadeh H, Chen Z. Reinfiltration through liquid bridges formed between two matrix blocks in fractured rocks. Journal of Hydrology. 2014;519:3520-3530.

128. Hu S, Koh CA. Interfacial properties and mechanisms dominating gas hydrate cohesion and adhesion in liquid and vapor hydrocarbon phases. Langmuir. 2017;33:11299-11309.

129. L. Bocquet, E. Charlaix, S. Ciliberto, J. Crassous. (1998) Moisture-induced ageing in granular media and the kinetics of capillary condensation Nature, 1998, 396(6713), 735 – 737.

130. Albert R, Albert I, Hornbaker D, Schiffer P, Barabasi A-L. (1997) Maximum angle of stability in wet and dry spherical granular media. Physical Review E. 1997;56(6):6271.

131. Fournier Z, Geromichalos D, Herminghaus S, Kohonen MM, Mugele F, Scheel M, Schulz M, Schulz B, Schier C, Seemann R, Skudelny A. Mechanical properties of wet granular materials. J. Phys.: Condens. Matter. 2005;17:S477 – S502.

132. Scheel M, Seemann R, Brinkmann M, Di Michiel M, Sheppard A, Breidenbach B, Herminghaus S. Morphological clues to wet granular pile stability. Nature Materials. 2008;7:189 – 193.

133. Halsey TC, Levine AJ. How sandcastles fall. Phys. Rev. Lett. 1998;80:3141.

134. Zhu R, Li S, Yao Q. Effects of cohesion on the flow patterns of granular materials in spouted beds. Physical Review E. 2013;87:022206.

135. Patnaik A, Rengasamy RS, Kothari VK, Ghosh A. Wetting and wicking in fibrous materials. Text. Prog. 2006;38:1 – 105.

136. Mullins BJ, Agranovski IE, Braddock RD, Ho CM. Effect of fiber orientation on fiber wetting processes. J. Colloid Interface Sci. 2004;269:449 – 458.

137. Yu Y, Chen H, Liu Y, Craig VSJ, Lai Z. Selective separation of oil and water with mesh membranes by capillarity. Adv Colloid Interface Sci. 2016;235:46 – 55.

138. Wurster S, Kampa D, Meyer J, Muller T, Mullins BJ, Kasper G. Measurement of oil entrainment rates and drop size spectra from coalescence filter media. Chem. Eng. Sci. 2015;132:72 – 80.

139. Wei X, Zhou H, Chen F, Wang H, Ji Z, Lin T. High-efficiency low-resistance oil-mist coalescence filtration using fibrous filters with thickness-direction asymmetric wettability. Adv. Funct. Mater. 2019:29(1);1806302.

140. Hotz CJ, Mead-Hunter R, Becker T, King AJC, Wurster S, Kasper G, Mullins BJ. Detachment of droplets from cylinders in flow using an experimental analogue. J. Fluid Mech. 2015;771:327 – 340.

141. Chilamakuri SK, Bhushan B. A comprehensive kinetic meniscus model for prediction of long-term static friction. J. Appl. Phys. 1999;86(8):4649.

142. Butt H-J, Kappl M. Normal capillary forces. Advances in Colloid and Interface Science. 2009;146:48 – 60.

143. van de Ven TGM. Capillary forces in wet paper. Ind. Eng. Chem. Res. 2008;47:7250 – 7256.

144. Keis K, Kornev KG, Neimark AV, Kamath YK, Towards fiber based micro- and nanofluidics. NATO Science series II: Mathematics, Physics and Chemistry, Kluwer publishing, 2004, 169, 175 – 182.

145. Gilet T, Terwagne D, Vandewalle N. Digital microfluidics in a wire. Appl. Phys. Lett. 2009;95: 014106.

146. Young T. An essay on cohesion of fluids Philos. Trans. R. Soc. London. 1805;95:65 – 87.

147. Finn R. Capillary surface interfaces. Not AMS. 1999;46:770 – 781.

148. De Souza EJ, Brinkmann M, Mohrdieck C, Crosby C, Arzt E. Capillary forces between chemically different substrates. Langmuir. 2008;24:10161 – 10168.

149. De Souza EJ, Gao L, McCarthy TJ, Arzt E, Crosby AJ. Effect of contact angle hysteresis on the measurement of capillary forces. Langmuir. 2008;24(4):1391 – 1396.

150. Chen H, Amirfazli A, Tang T. Modeling liquid bridge between surfaces with contact angle hysteresis. Langmuir. 2013;29:3310 – 3319.

151. Wang Y, Michielsen S, Lee HJ. Symmetric and asymmetric capillary bridges between rough surface and parallel surface. Langmuir. 2013;29: 11028 – 11037.

152. Kusumaatmaja H, Lipowsky R. Equilibrium morphologies and effective spring constants of capillary bridges. Langmuir. 2010;26(24):18734 – 18741.

153. Qian B, Breuer KS. The motion, stability and breakup of a stretching liquid bridge with a receding contact line. J. Fluid Mech. 2011;666:554 – 572.

154. Hotta K, Takeda K, Iinoya K. The capillary binding force of a liquid bridge. Powder Technology. 1974;10:231 – 242.

155. Butt H-J. Capillary forces: Influence of roughness and heterogeneity. Langmuir 2008;24(9):4715 – 4721.

156. Vagharchakian L, Restagno F, Leger L. Capillary bridge formation and breakage: A test to characterize adhesive surfaces. J. Phys. Chem. B. 2009;113:3769 – 3775.

157. Willet CD, Adamd MJ, Johnson SA, Seville JPK. Capillary bridges between two spherical bodies. Langmuir. 2000;16:9396 – 9405.

158. Lambert P, Chau A, Delchambre A, Regnier S. Comparison between two capillary force models. Langmuir. 2008;24:3157 – 3163.

159. Mazzone DN, Tardos GI, Pfeffer R. The effect of gravity on the shape and strength of a liquid bridge between two spheres. Journal of Colloid and Interface Science. 1986;113(2):544 – 556.

160. Adams MJ, Johnson SA, Seville PK, Willet CD. Mapping the influence of gravity on pendular liquid bridges between rigid spheres. Langmuir. 2002;18:6180–6184.

161. Princen HM. Capillary phenomena in assemblies of parallel cylinders III. Liquid columns between horizontal parallel cylinders. Journal of Colloid and Interface Science. 1970;34(2):171 – 184.

162. Protiere S, Durprat C., Stone HA. Wetting on two parallel fibers: drop to column transitions. Soft Matter. 2013;9: 271.

163. Schellbach SL, Monteiro SN, Drelich JW. A novel method for contact angle measurements on natural fibers. Materials Letters. 2016;164: 599 – 604.

164. Virozub A, Haimovich N, Brandon S. Three-dimensional simulation of liquid bridges between two cylinders: forces, energies and torques. Langmuir. 2009;25(22):12837 – 12842.

165. Wu X-F, Bedarkar A, Vaynberg KA. Droplets wetting on filament rails: surface energy and morphology transition. Journal of Colloid and Interface Scinece. 2010;341:326 – 332.

166. Bedarkar A, Wu X-F, Vaynberg A. Wetting of liquid droplets on two parallel filaments. Applied Surface Science. 2010;256:7260 – 7264.

167. Durpat C, Protiere S. Capillary stretching of fibers. EPL. 2015;111:56006.

168. Durpat C, Protiere S, Beebe AY, Stone HA. Wetting of flexible fiber arrays. Nature. 2012;482: 510 – 513.

169. Soleimani M, Hill RJ, van de Ven TGM. Capillary force between flexible filaments. Langmuir. 2015;31: 8328 – 8334.

170. Aziz H, Farhan NM, Tafreshi HV. Effects of fiber wettability and size on droplet detachment residue. Experiments in Fluids. 2018;59:122.

171. Farhan NM, Tafreshi HV. Universal expression for droplet-fiber detachment force. J. Appl. Phys. 2018;124:075301.

172. Farhan NM, Aziz H, Tafreshi HV. Simple method for measuring intrinsic contact angle of a fiber with liquids. Experiments in Fluids. 2019;60:87.

173. Gopalkrishan P, Manas-Zloczower I, Feke DL. Modeling time-dependent forces on liquid bridge interactions between dissimilar particles. Advanced Powder Technology. 2008;19:277 – 292.

174. Brakke KA. Surface Evolver manual version 2.50, 2012.

175. Farmer TP, Bird JC. Asymmetric capillary bridges between contacting spheres. Journal of Colloid and Interface Science. 2015;454:192 – 199.

176. Sun X, Lee HJ, Michielsen, Wilusz E. Profile of capillary bridges between two vertically stacked cylindrical fibers under gravitational effect. Applied Surface Science 2018;441:791 – 797.

177. Ponomarenko A, Quere D, Clanet C (2011) Universal law of capillary rise in corners. J. Fluid Mech. 666: 146 – 154.

178. Ojaghlou N, Tafreshi HV, Bratko D, Luzar A. Dynamical insights into the mechanism of droplet detachment from a fiber. Soft Matter. 2018;14:8924.

179. Guo F, Servi A, Liu A, Gleason KK, Rutledge GC. Desalination by membrane distillation using electrospun polyamide fiber membranes with surface fluorination by chemical vapour deposition. ACS Appl. Mater. Interfaces. 2015;7:8225 – 8232.

180. Liao Y, Loh C-H, Wang R, Fane AG. Electrospun superhydrophobic membranes with unique structures for membrane distillation. ACS Appl. Mater. Interfaces. 2014;6:16035 – 16048.

181. Jamali M, Moghadam A, Tafreshi HV, Pourdeyhimi B. Droplet adhesion to hydrophobic fibrous surfaces. Applied Surface Science. 2018;456:626 - 636.

182. Jamali M, Tafreshi HV, Pourdeyhimi B. Droplet mobility on hydrophobic fibrous coatings comprising orthogonal fibers. Langmuir. 2018;34(41):12488-12499.

183. Jamali M, Tafreshi HV, Pourdeyhimi B. Penetration of liquid droplets into hydrophobic fibrous materials under enhanced gravity. J. Appl. Phys. 2019;125(14):145304.

184. Kim YH, Choi W, Lee JS. Water droplet properties on periodically structured superhydrophobic surfaces: A lattice Boltzmann approach to multiphase flows with higher water/air density ratio. Microfluid Nanofluid. 2011;10:173 – 185.

185. Dupuis A, Yeomans JM. Modeling droplets on superhydrophobic surfaces: Equilibrium states and transitions. Langmuir. 2005;21:2624 – 2629.

186. Dubov AL, Mourran A, Moller M, Vinogradova OI. Regimes of wetting transitions on superhydrophobic textures conditioned by energy of receding contact lines. Applied Physics Letters. 2015;106:241601.

187. Zu YQ, Yan YY. Single droplet on micro square post patterned surfaces – theoretical model and numerical simulation. Scientific Reports. 2016;6:19281.

188. Bucher TM, Tafreshi HV. Modeling air-water interface in disordered fibrous media with heterogeneous wettabilities. Colloids and Surfaces A: Physicochem. Eng. Aspects. 2014;461:323-335.

189. Zhang B, Wang J, Liu Z, Zhang X. Beyond Cassie equation: Local structure of heterogeneous surfaces determines the contact angles of microdroplets. Sci. Rep. 2014;4:5822.

190. Marmur A. From hydrophilic to superhydrophobic: Theoretical conditions for making high-contact-angle surfaces from low-contact-angle materials. Langmuir. 2008;24:7573-7579.

191. Extrand CW. Criteria for Ultralyophobic Surface. Langmuir. 2004;20:5013–5018.

192. Choi CH, Kim CJ. Large slip of aqueous liquid flow over a nanoengineered superhydrophobic surface. Physical Review Letters. 2006;96:066001.

193. McHale, G., Newton, M.I., Shirtcliffe, N.J., 2010. Immersed superhydrophobic surfaces: Gas exchange, slip and drag reduction properties. Soft Matter 6, 714 – 719.

194. Sbragaglia, M., Prosperetti, A., 2007a. Effective velocity boundary condition at a mixed slip surface. Journal of Fluid Mechanics 578, 435 – 451.

195. Verho T, Korhonen JT, Sainiemi L, Jokinen V, Bower C, Franze K, Franssila S, Andrew P, Ikkala O, Ras RHA. Reversible switching between superhydrophobic states on a hierarchically structured surface. Proc. Natl. Acad. Sci. U. S. A. 2012;109(26):10210 – 10213.

196. Vourdas N, Ranos C, Stathopoulos VN. Reversible and dynamic transitions between sticky and slippery states on porous surface with ultralow backpressure. RSC Adv. 2015;5(42):33666 – 33673.

197. Vourdas N, Pashos G, Kokkoris G, Boudouvis AG, Stathopoulos VN. Droplet mobility manipulation on porous media using back pressure. Langmuir. 2016;32:5250 – 5258.

198. Jiang ZX, Geng L, Huang YD. Fabrication of superhydrophobic 3-D braided carbon fiber fabric boat. Materials Letters. 2010;64:2441–2443.

199. Pan Q, Wang M. Miniature boats with striking loading capacity fabricated from superhydrophobic copper meshes. ACS Applied Materials and Interfaces. 2009;1:420–423.

200. Wang C, Tang F, Li Q, Zhang Y, Wang X. Spray-coated superhydrophobic surfaces with wear-resistance, drag reduction and anti-corrosion properties. Colloids and Surfaces A. 2017;514:236 – 242.

201. Hemeda AA, Tafreshi HV. Instantaneous Slip Length in Superhydrophobic Microchannels having Grooves with Curved or Dissimilar Walls. Physics of Fluids. 2015;27:102101.

202. Extrand CW, Moon SI. Intrusion Pressure To Initiate Flow through Pores between Spheres. Langmuir. 2012;28:3503–3509.

203. Hemeda AA, Amrei MM, Tafreshi HV. Wetting states of superhydrophobic surfaces made of polygonal pores and posts. Journal of Applied Physics. 2016;119:175304.

204. Srinivasan S, Choi W, Park KC, Chhatre SC, Cohen RE, McKinley GH. Drag reduction for viscous laminar flow on spray-coated non-wetting surfaces. Soft Matter. 2013;9:5691.

205. Davis AMJ, Lauga E. The friction of a mesh-like super-hydrophobic surface. Physics of Fluids. 2009;21:113101.

206. Hyvaluoma J, Harting J. Slip flow over structured surfaces with entrapped microbubbles. Physical Review Letters. 2008;100:246001.

207. Vidal A, Botto L. Slip flow past a gas-liquid interface with embedded solid particles. Journal of Fluid Mechanics. 2017;813:152–174.

208. Venkateshan DG, Amrei MM, Hemeda AA, Cullingsworth Z, Corbett J, Tafreshi HV. Failure pressures and drag reduction benefits of superhydrophobic wire screens. Colloids and Surfaces A. 2016;511:247–254.

209. Cottin-Bizonne C, Barentin C, Charlaix E, Bocquet L, Barrat JL. Dynamics of simple liquids at heterogeneous surfaces: Molecular-dynamics simulations and hydrodynamic description. European Physical Journal E. 2004;15:427–438.

210. Hasse AS, Karatay E, Tsai PA, Lamertink RGH. Momentum and mass transport over bubble mattress: the influence of interface geometry. Soft Matter. 2013;9:8949.

211. Haase AS, Wood JA, Lammertink RGH, Snoeijer JH. Why bumpy is better: The role of the dissipation distribution in slip flow over a bubble mattress. Physical Review Fluids. 2016;1:054101.

212. Sbragaglia M, Prosperetti A. A note on the effective slip properties for microchannel flows with ultrahydrophobic surfaces. Physics of Fluids. 2007;19:043603.

213. Pihl M, Jonsson B, Skepo M. Effect of patchwise slip on fluid flow. Microfluid Nanofluid. 2014;17:341 – 347.

214. Yousefi SH, Venkateshan DG, Tang C, Tafreshi HV, Pourdeyhimi B. Effects of electrospinning conditions on microstructural properties of polystyrene fibrous materials. J. Appl. Phys. 2018;124:235307

215. Emami B, Tafreshi HV, Gad-el-Hak M, Tepper GC. Predicting shape and stability of air-water interface on superhydrophobic surfaces with randomly distributed, dissimilar posts. Appl. Phys. Lett. 2011;98:203106.

216. Aziz H, Amrei MM, Dotivala A, Tang C, Tafreshi HV. Modelling Cassie droplets on superhydrophobic coatings with orthogonal fibrous structures. Colloid Surf. A. 2017;512:61 – 70.

217. Moghadam A, Jamali M, Venkateshan DG, Tafreshi HV, Pourdehimi B. A new approach to modeling liquid intrusion in hydrophobic fibrous membranes with heterogeneous wettabilities. Colloid Surf. A. 2018;512:61 – 70.

218. Moghadam A, Yousefi SH, Tafreshi HV, Pourdeyhimi B. Characterizing nonwoven material via realistic microstructural modeling. Separation and Purification Technology. 2019;211:602-609.

219. Antonoff G. On the validity of Antonoff's rule. J. Phys. Chem. 1942;46(4):497 – 499.

220. Aziz H, Tafreshi HV. Role of particles spatial distribution in drag reduction performance of superhydrophobic granular coatings. Int. J. Multiphase Flow. 2018;98:128 – 138.

221. Gruncell BRK, Sandham ND, McHale G. Simulations of laminar flow past a superhydrophobic sphere with drag reduction and separation delay. Phys. Fluids. 2013;25:043601.

222. Dorr A, Hardt S, Masoud H, Stone HA. Drag and diffusion coefficients of a spherical particle attached to fluid-fluid interface. J. Fluid Mech. 2016;790:607 – 618.

223. Jin M, Wang J, Yao X, Liao M, Zhao Y, Jiang L. Underwater oil capture by a three-dimensional network architectured organosilane surface. Advanced Materials. 2011;23:2861 – 2864.

224. Palama IE, D'Amone S, Arcadio V, Caschera D, Toro RG, Gigli G, Cortese B. Underwater Wenzel and Cassie oleophobic behavior. Journal of Materials Chemistry A. 2015;3:3854 – 3861.

Appendix A: Supporting Information for Chapter 2

Appendix-A-1: Measuring Fibers' YLCA:

A simulation–experiment approach was used to obtain an YLCA for fibers used in our experiment. In this method, a ferrofluid droplet with a known volume was placed on the fiber and imaged. The same droplet–fiber system was then simulated using Surface Evolver code (119) but for fibers with different YLCAs. The simulated droplets were compared with the one imaged experimentally to assign an YLCA to the fiber. This process was repeated several times and for the ferrofluid droplets of different volumes to ensure the reliability of the YLCA prediction. Figure A1 shows an YLCA of around 65° for ferrofluid on a fiber with a radius of 264 µm.

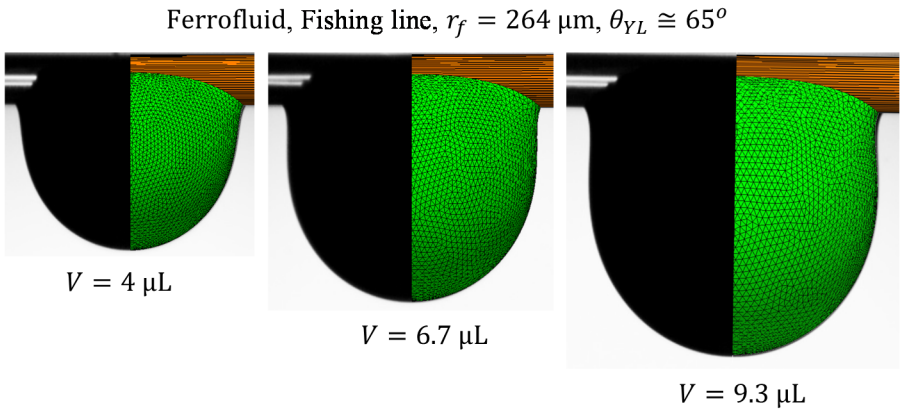

Fig. A1: Comparison between ferrofluid droplet profiles (under gravity) from simulation and experiment for droplets with volumes $4\ \mu L \leq V \leq 9.3\ \mu L$ on a fiber with a radius of 264 µm (see also Amrei et al. (38)).

We also compared the shape of the droplet observed from the longitudinal direction from simulation with that from experiment for a few cases to confirm the accuracy of our YLCA measurements (see Figure A2).

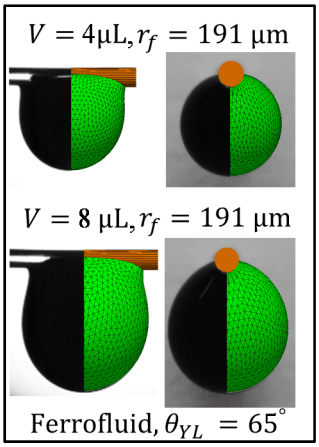

Fig. A2: Comparison between droplet profile from simulation and experiments from the transverse and longitudinal views under gravity for $r_f = 191\ \mu m$ and $\theta_{YL} = 65^{o}$.

Appendix-A-2: Viscosity Measurement

Viscosities for ferrofluid and ferrofluid-glycerol mixtures were measured with a Discovery HR–3 hybrid rheometer. Both the ferrofluid and ferrofluid-glycerol mixtures behaved like a Newtonian fluid. The flow curve for ferrofluid with 15% glycerol (by weight) is shown below as an example.

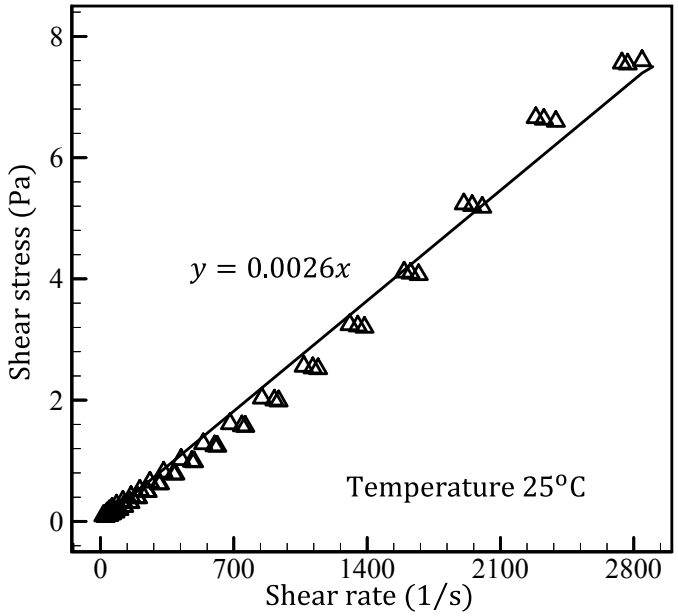

Fig. A3: Flow curve obtained from rheometer for ferrofluid with 15% glycerol. An almost linear relationship between shear stress and shear rate can be observed.

Appendix-A-3: Shape of the detached droplet

The shape of the detached droplet was assumed to be symmetric about the z-axis. This was confirmed by imaging the detached droplet from the transverse and longitudinal directions for a few droplet-fiber cases.

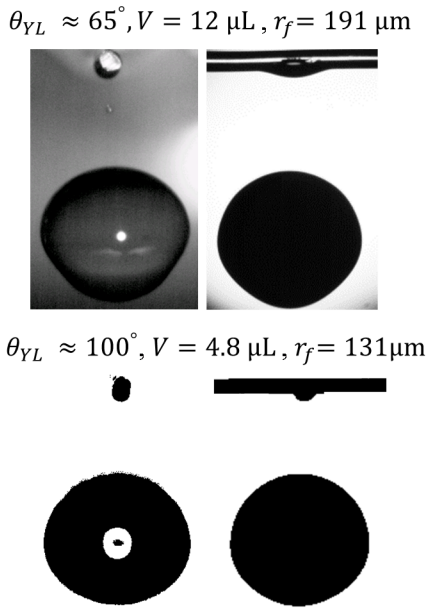

Fig. A4: Longitudinal and transverse views of the detached part of the droplet for two different droplet-fiber systems.

Appendix-A-4: Neck Diameter and Detachment Force Measurement for Fishing Line

Neck diameter at each time instant was measured using high-speed imaging for each case. Figure A5a shows the change of neck diameter (normalized with fiber radius) with time for droplets of different volume during the detachment from a fiber with radius 191 µm and YLCA 65^{o}. We also measured the detachment force for each case. It can be seen in Fig. A5b that detachment force per unit mass of the droplet decreases with the increase of YLCA as well as with the increase of

droplet volume. Figure A5c shows how the droplet shape at the detachment initiation moment changes with YLCA when fiber radius and droplet volume is kept constant. Detachment force changes with the change of fiber radius too. Figure A5d shows that the detachment force per unit mass of the droplet decreases with the increase of fiber radius for a fixed YLCA.

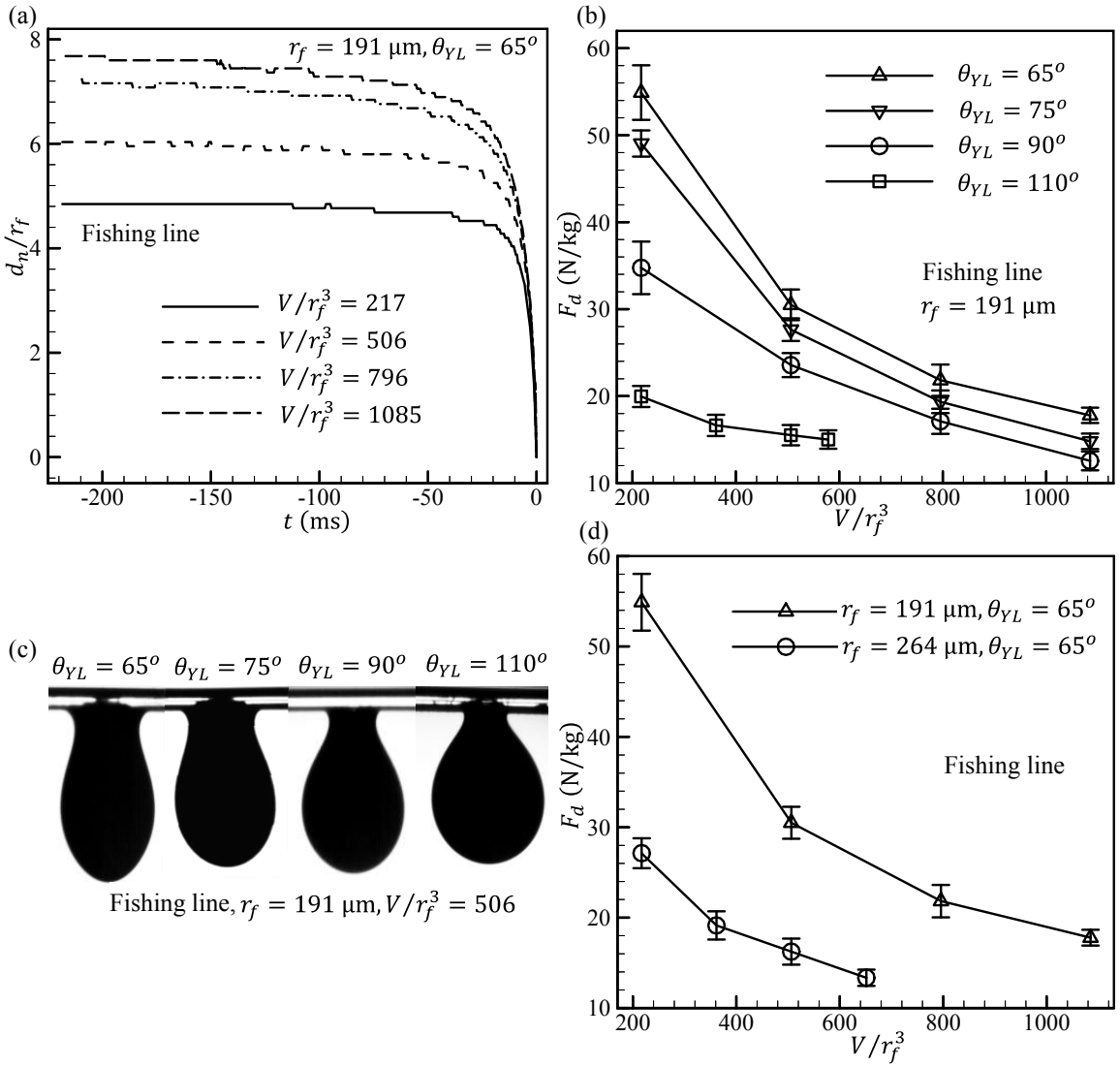

Fig. A5: (a) Neck diameter vs. time for droplets of different volumes during the detachment from a fiber with a radius of 191 μm and an YLCA of 65°. (b) Effects of YLCA on the detachment force per unit mass of the droplet. (c) Final equilibrium (right before spontaneous detachment) shape of droplets with a volume of $V/r_f^3 = 506$ on fibers with different YLCAs. (d) Droplet detachment force per unit droplet mass for fibers with two different radii.

Appendix-A-5: Experiment with Copper Wire

The droplet detachment experiment was also performed using copper wires with different radius but an YLCA of about 50^o (Fig. A6). The conclusions drawn from experiments with copper wire were similar to those reported in the paper from experiment with fishing line.

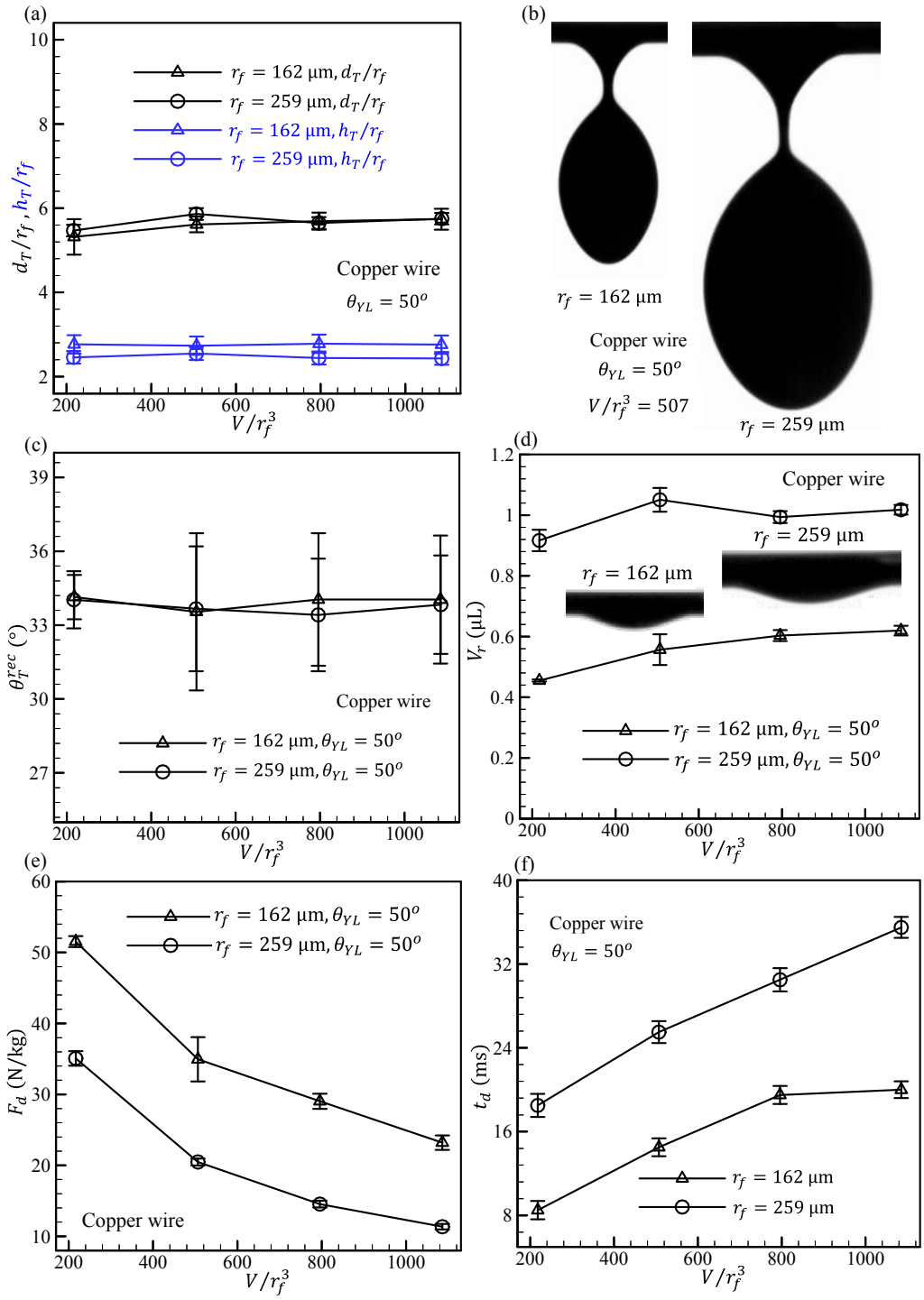

Fig. A6: (a) Effects of fiber radius on d_T/r_f and h_T/r_f for droplet detachment from copper wires with different diameters but an YLCA of 50°. (b) Droplet profiles just before the detachment from copper wires for a droplet dimensionless volume of $V/r_f^3 = 507$. (c) Transverse contact angle θ_T^{rec} vs. droplet volume. (d) Residue volume on copper wires vs. droplet volume. The inset images show the residue on wires with a radius of 162 μm and 259 μm with YLCA 50°. (e) and (f) are droplet detachment force per unit mass and droplet detachment time from wires, respectively.

Appendix B: Supporting Information for Chapter 3

Appendix-B-1: Effect of Fiber-Fiber Spacing on Capillary Force:

Figure 3.6 in the chapter 3 can be explained using Eq. 3.8 which indicates that the force acting on a fiber depends on length of the contact line L, immersion angle α, projected wetted area of the fiber A_p, Laplace pressure ΔP, and the volume of the immersed part of the fiber i.e. V_b. It can be seen in Figs. B1a-B1e (in the next page) that L^u, α^u_{avg}, A^u_p, ΔP^u and V^u_b decrease with increasing fiber spacing which results in an increase in F^u (according to Figs. 3.6a-3.6b in chapter 3). It was observed that the force F^l acting on the lower fiber also increases with increasing s (see Fig. 3.6c in chapter 3). F^l is always smaller than F^u, and the difference between them is the weight of the liquid bridge. It is also interesting to note that α changes significantly along the contact line for both the upper and lower fibers (see Fig. B1f).

It can be seen in Figs. 3.6a and 3.6b of the chapter 3 that F^u just before the start of the dynamic detachment process is same for parallel and orthogonal configurations, although the evolution of F^u with spacing is different for parallel and orthogonal configurations (spontaneous detachment process started at $s \approx 2400$ μm for both configurations). The reason behind this was that the values of L^u, α^u, A^u_p, ΔP^u and V^u_b were identical for both configurations at $s \approx 2400$ μm. This indicates that the shape of the wetted area, contact length, and apparent local contact angle on the upper fiber don't depend on the orientation of the lower fiber.

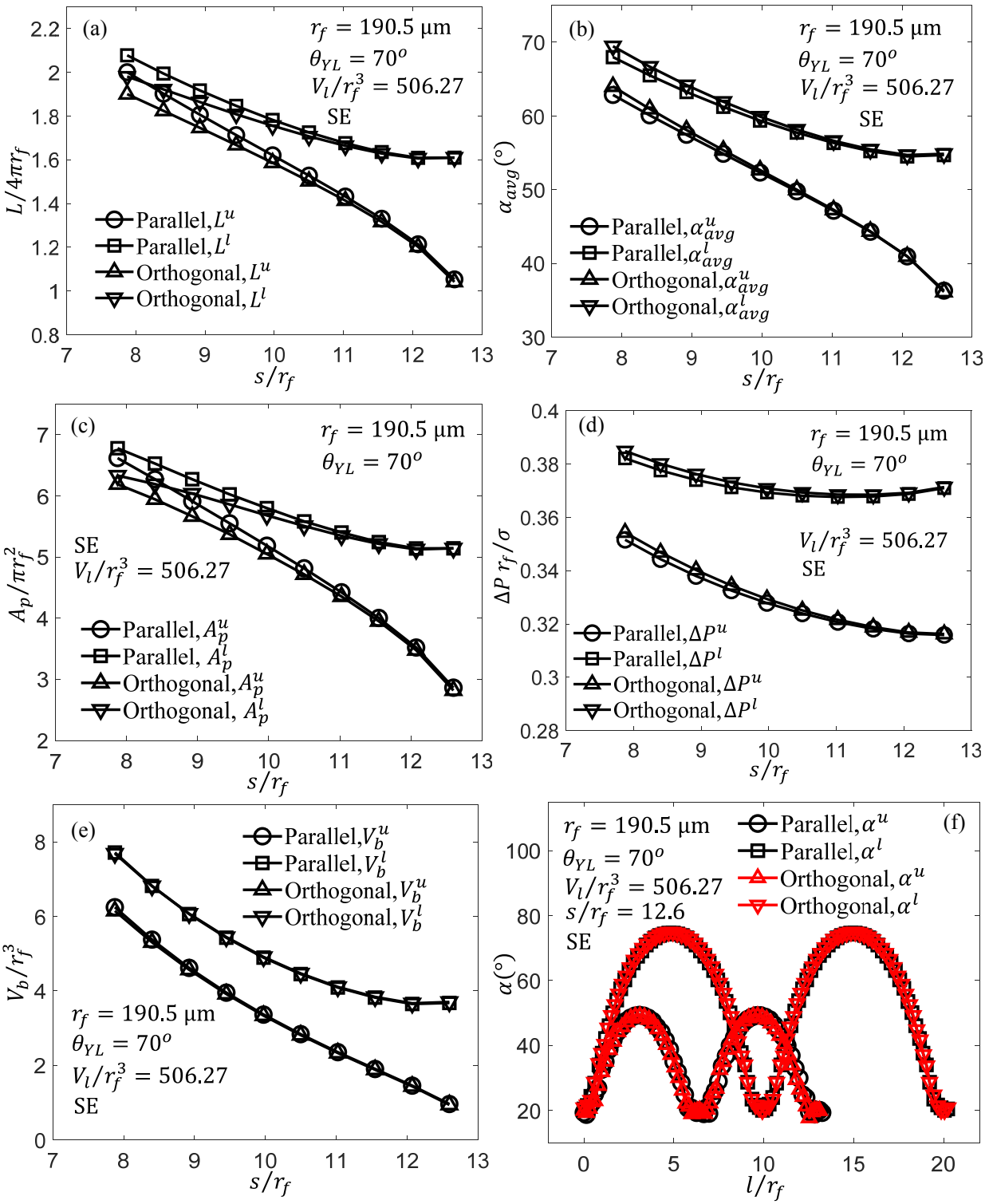

Fig. B1: (a) Length of contact line L (non-dimensionalized by $4\pi r_f$) versus fiber spacing for two fibers in parallel and orthogonal configurations. (b) α_{avg} versus fiber spacing. Normalized A_p, normalized ΔP and normalized V_b versus fiber spacing are given in (c), (d), and (e) respectively. (f) α along the contact

line for $s/r_f = 12.6$. For all the cases $r_f = 190.5$ µm, $\theta_{YL} = 70^o$, and $V_l/r_f^3 = 506.27$. The liquid used for the experiment was water-glycerol (15% by weight) mixture.

Appendix-B-2: Detachment Force between Two Fibers having Same Properties:

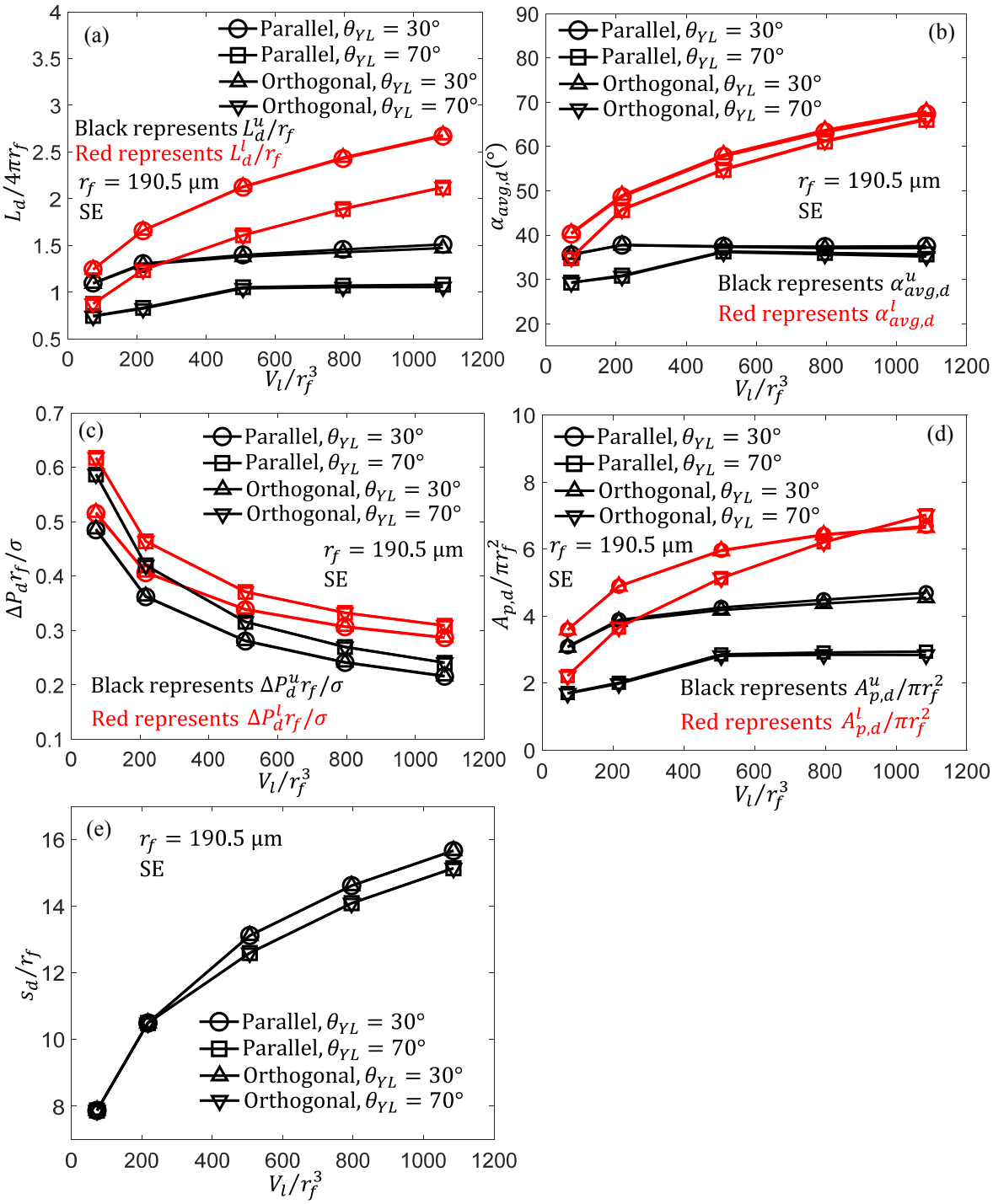

Fig. B2: (a) Length of contact line at the onset of detachment L_d (non-dimensionalized by $4\pi r_f$) versus droplet volume. (b) $\alpha_{avg,d}$ versus droplet volume. Normalized ΔP_d, normalized $A_{p,d}$, and normalized s_d versus droplet volume for different θ_{YL} values at $r_f = 190.5$ μm are given (c), (d), and (e) respectively. Here, the subscript *d* indicates the values at the onset of the detachment. The liquid used for the experiment was water-glycerol (15% by weight) mixture.

The values of L_d^u, $\alpha_{avg,d}^u$, ΔP_d^u, $A_{p,d}^u$ and s_d are computed for both the parallel and orthogonal configurations for all the cases shown in Fig 3.8a in the chapter 3 and they are presented in Figs. B2a–B2e here. It can be observed that L_d^u, $\alpha_{avg,d}^u$, ΔP_d^u, $A_{p,d}^u$ and s_d are the same for parallel and orthogonal configurations in all the cases. This again indicates that the detachment force between the liquid bridge and a fiber depends on the shape of the liquid bridge in the vicinity of that fiber (top fiber in the present case) which depends on r_f, θ_{YL} and V_l irrespective of the configuration of the fibers, as long as the fiber is moved slowly (quasi-static process). We also calculated L_d^l, $\alpha_{avg,d}^l$, ΔP_d^l, $A_{p,d}^l$ for the lower fiber for all the cases mentioned above and noted that they did not depend on fiber configuration when the droplet volume and fiber properties were fixed (see Fig. B2). It was also clear that the detachment force increased with decreasing θ_{YL}. The adhesive force between the liquid bridge and the fiber increases with decreasing θ_{YL} (171). It is therefore expected that the force required to detach the liquid bridge from the upper fiber will increase with decreasing θ_{YL}. Parameters L_d, $\alpha_{avg,d}$, ΔP_d, $A_{p,d}$ and s_d were also computed for the cases shown in Fig. 3.8b in chapter 3, but not reported as they were identical for the parallel and orthogonal configurations. Figure 3.8b also shows that detachment force increases with increasing fiber radius r_f (because L_d^u increases and $\alpha_{avg,d}^u$ decreases with r_f). This is in agreement with the previous work of Farhan and Tafreshi (171) on pendant droplet detachment.

Appendix-B-3: Detachment Force between Two Fibers having Different Properties:

It can be seen in Fig. 3.9b in the chapter 3 that the detachment force is same for parallel and orthogonal configurations even when the upper and lower fibers have different properties. This can be explained with the help of Figs. B3a-B3e. It can be seen that the parameters L_d^u, $\alpha_{avg,d}^u$, ΔP_d^u, $A_{p,d}^u$ and s_d is same for parallel and orthogonal configurations in all the cases where upper and lower fibers have different properties. Figures B3a-B3e also show that the parameters L_d^u, $\alpha_{avg,d}^u$, ΔP_d^u and $A_{p,d}^u$ do not change significantly with the change in properties of the lower fiber when the properties of the upper fiber is fixed except for $V_l / r_f^{u3} = 1703.23$.

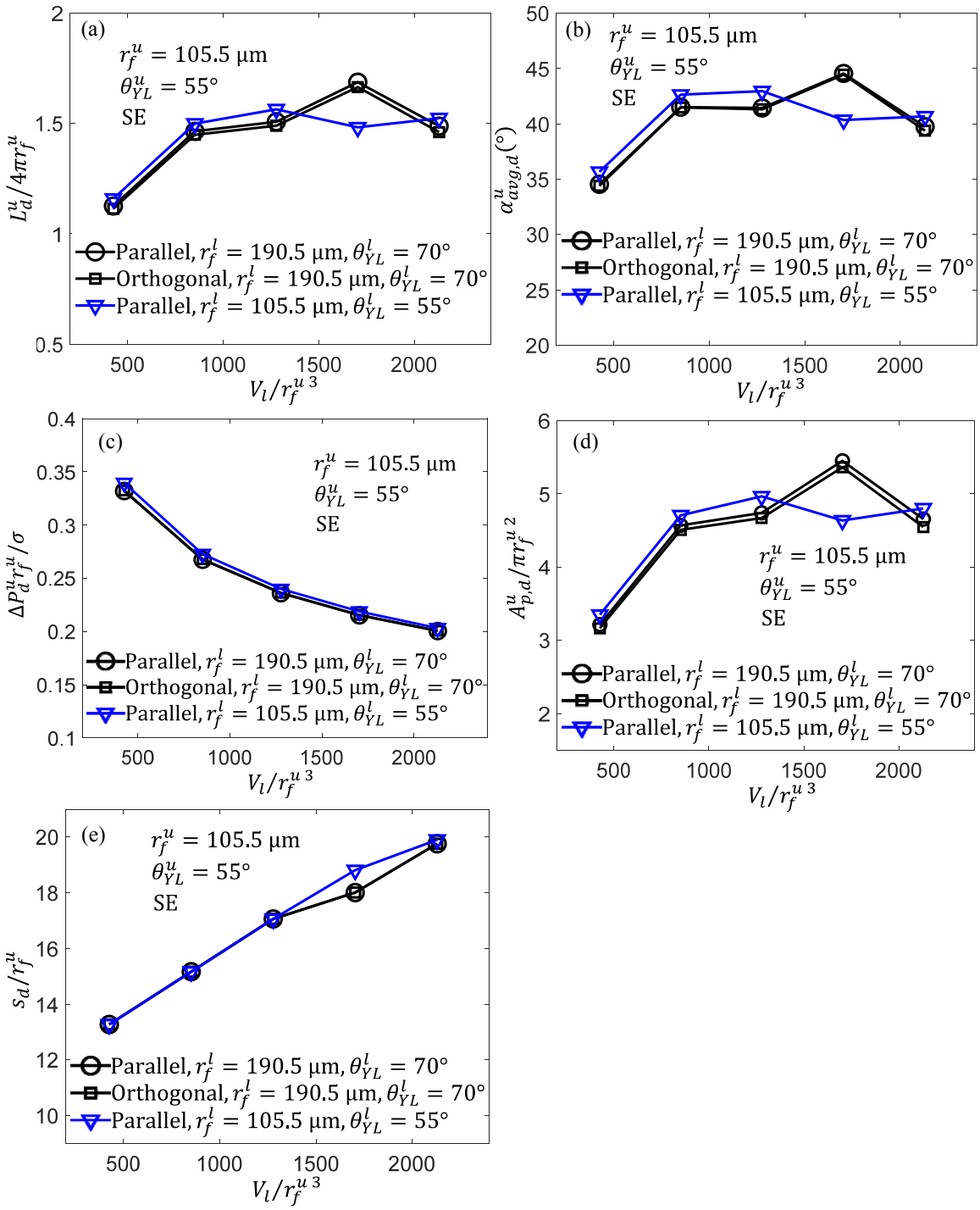

Fig. B3: (a) Length of the contact line on upper fiber L_d^u (non-dimensionalized by $4\pi r_f^u$) versus droplet volume. (b) $\alpha_{avg,d}^u$ versus droplet volume. Normalized ΔP_d^u, normalized $A_{p,d}^u$, and normalized s_d versus droplet volume for upper and lower fibers having different properties are given in (c), (d), and (e). For all the cases $r_f^u = 105.5$ µm and $\theta_{YL}^u = 55^o$. The liquid used for the experiment was water-glycerol (15% by weight) mixture.

Appendix C: Vita

Hossain Aziz

PhD Candidate
Mechanical and Nuclear Engineering Department, Virginia Commonwealth University
Office: 804-827-2029; Cell: 540-838-1436; Email: azizh2@vcu.edu

EDUCATION

- **PhD, Mechanical & Nuclear Engineering** (2015–2019)
  Virginia Commonwealth University
  GPA: 4 out of 4

- **MS, Applied Mechanics** (2008–2011)
  Indian Institute of Technology Madras, Chennai, India
  GPA: 8.6 out of 10

- **BE, Mechanical Engineering** (2002–2006)
  Indian Institute of Engineering Science and Technology, Shibpur, Howrah, India
  Percentage: 72.27 (First Class)

WORK EXPERIENCE

- **Graduate Research Assistant**, VCU, Richmond VA, USA (2017–2019)
- **Graduate Teaching Assistant**, VCU, Richmond VA, USA (2015–2017)
- **Graduate Teaching Assistant**, Virginia Tech, Blacksburg VA, USA (2013–2015)
- **Assistant Professor**, Aliah University, Kolkata, India (2012-2013)
- **Project Officer,** IIT Madras, Chennai, India (2011-2012)
- **Programmer Analyst**, CTS India Pvt. Ltd., Kolkata, India (2006-2007)

RESEARCH INTERESTS AND ACTIVITIES

- Porous Media and Multiphase Flow
- Computational Fluid Dynamics
- Interfacial Phenomena

HONORS AND AWARDS

- Recipient of **VCU College of Engineering Dissertation Assistantship Award** for the 2018 – 2019 academic year.
- Recipient of a travel grant from IIT Madras to attend the conference "**International Conference on Mechanical and Aerospace Engineering**", October 27-29 (2010), Paris, France.
- Recipient of a travel grant from IIT Madras to attend the conference "**The 13th Asian Congress on Fluid Mechanics**", December 17-21 (2010), Dhaka, Bangladesh.
- Human Resource Development, Government of India scholarship for a period of 3 years (January 2008 to December 2010).

SKILLS

- **Computer Programming:** FORTRAN, C, COBOL, PYTHON, MATLAB, Mathematica
- **Engineering Software:** Surface Evolver, ANSYS Fluent, ANSYS DesignModeler, and Adobe Designer
- **Experimental:** High-speed imaging and image processing, Surface characterization, Data acquisition
- **General:** MS Office, Tecplot, Adobe Photoshop

PEER-REVIEWED JOURNAL PUBLICATIONS

1. **H. Aziz**, A.A. Hemeda, and H.V. Tafreshi, "Fibrous Liquid-Infused Surface with Trapped-Air (FLISTA) for Drag Reduction", (to be submitted)

2. **H. Aziz** and H.V. Tafreshi, "Competing Forces on a Liquid Bridge between Parallel and Orthogonal Dissimilar Fibers", (under review)

3. N.M. Farhan, **H. Aziz** and H.V. Tafreshi, "Simple Method for Measuring Intrinsic Contact Angle of a Fiber with Liquids" *Experiments in Fluids* 60:87 (2019)

4. **H. Aziz,** N.M. Farhan and H.V. Tafreshi, "Effects of Fiber Wettability and Size on Droplet Detachment Residue", *Experiments in Fluids* 59:122 (2018)

5. **H. Aziz** and H.V. Tafreshi, "Role of Particles Spatial Distribution in Drag Reduction Performance of Superhydrophobic Granular Coatings", *International Journal of Multiphase Flow* 98, 128 (2018)

6. **H. Aziz**, M.M. Amrei, A. Dotivala, C. Tang, and H.V. Tafreshi, "Modeling Cassie Droplets on Superhydrophobic Coatings with Orthogonal Fibrous Structures", *Colloids and Surfaces A* 512, 61-70 (2017)

7. **H. Aziz** and R. Mukherjee, "Vortex Interaction and Roll-Up in Unsteady Flow past Tandem Airfoils", *Journal of Applied Fluid Mechanics* 9(6), 3087-3100 (2016)

SELECTED CONFERENCES AND WORKSHOPS

1. N.M. Farhan, **H. Aziz**, N. Ojaghlou, Henry Holweger, H.V. Tafreshi, "On the Adhesion Force between a Droplet and a Single Fiber", American Filtration and Separations Society (AFS), April 01-04 (2019), Cherry Hill, NJ, USA.

2. **H. Aziz** and H.V. Tafreshi, "Interaction of Water with Superhydrophobic coatings", Virginia Soft Matter Workshop, September 4 (2017), Harrisonburg, VA, USA.

3. **H. Aziz**, M.M. Amrei, H.V. Tafreshi, The Effect of Fibrous Coating Characteristics on Apparent Contact Angle, Nanofibers, Applications & Related Technologies (NART) conference, Sept. 13-15 (2016), Raleigh, NC, USA.

4. R.A. Shirsath, **H. Aziz**, and R. Mukherjee, "A Numerical Study of Tandem Pitching Airfoils", AIAA 2013-0793, Jan 2013.

5. **H. Aziz** and R. Mukherjee, "Unsteady Aerodynamics of Multiple Airfoils in Configuration", International Conference on Mechanical and Aerospace Engineering", October 27-29 (2010), Paris, France.

6. **H. Aziz** and R. Mukherjee, "Unsteady Aerodynamics of Suddenly Accelerated Multiple Airfoils", The 13th Asian Congress on Fluid Mechanics, December 17-21 (2010), Dhaka, Bangladesh.

7. **H. Aziz** and R. Mukherjee, "Aerodynamic characteristics of a wing-tail and wing-canard configuration", 3rd International Congress on Computational Mechanics and Simulation, December 1-5 (2009), IIT Bombay, Mumbai, India.

GRADUATE COURSEWORK

IIT Madras, India

Advanced Fluid Mechanics, Introduction to Turbulence, Engineering Aerodynamics and Flight Mechanics, Foundations of Computational Fluid Dynamics, Computational Techniques in Applied Mechanics.

Virginia Tech, USA

Continuum Mechanics, Intermediate Dynamics, Applied Tensor Analysis, Computational Fluid Dynamics and Heat Transfer, Compressible Flow I, Operational Methods, Non-Newtonian Fluid Mechanics, Introduction to Perturbations, Theory of Elasticity, Advanced Dynamics, Nonlinear Dynamics and Chaos.

Virginia Commonwealth University, USA

Topics in Nuclear Engineering, Mechanical and Nuclear Engineering Materials, Convective Heat Transfer.